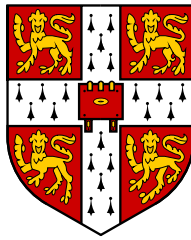


# Design of Sandwich Structures

Achilles Petras

Robinson College, Cambridge



Supervisor: Dr M.P.F. Sutcliffe

A dissertation submitted to  
**Cambridge University Engineering Department**  
for the degree of Doctor of Philosophy

December, 1998

*To my parents and bebita*

# Declaration

This dissertation presents the results of research carried out in the Engineering Department of the University of Cambridge between October 1995 and October 1998. Except where specific reference is made to the work of others, this dissertation is the original result of my own work and includes nothing which is the outcome of work done in collaboration. No part of this dissertation has been submitted for a degree at any other University. This dissertation is approximately 35,000 words long and contains 50 figures.

March 5, 1999

Achilles Petras  
Robinson College, Cambridge

# Acknowledgements

I would like to express my gratitude to my supervisor Dr Michael Sutcliffe for all his kind help, encouragement and dedicated guidance, without which, this project would not have been possible. He gave me flexibility to follow my research interests, but at the same time he kept me going in the right direction. His patience with proof-reading my thesis is highly appreciated.

I am also grateful to Professor Norman Fleck for his invaluable advice and fruitful discussions. I would like to thank him for supporting financially my project (US Office of Naval Research grant #0014-91-J-1916), and my attendance at the 4th International Conference on Sandwich Construction in Stockholm.

I acknowledge with gratitude the generous financial support of the Greek State Scholarship Foundation (IKY). I would like to thank Professors Christos Panagopoulos and Constantinos Lascarides at the National Technical University of Athens and Dr Dimitris Niarchos at the National Centre for Scientific Research ‘Demokritos’ in Greece for supporting and urging me to pursue my PhD studies at Cambridge.

I would like to thank Nigel Hookham and Peter Clayton from Hexcel Composites in Duxford for providing materials and valuable technical information. I wish to acknowledge the Cambridge University Engineering Department (CUED) and especially the Cambridge Centre for Micromechanics (CCM) for use of their facilities. I am also grateful to Alan Heaver and Simon Marshall for building the test rigs and helping me during my experiments. Special thanks to the CUED’s librarians for their kindest assistance. I wish to thank my friend Antonios Zervos for helping me out on computational modelling topics. Many thanks to Roxy, Pia, Ingo, Sinisa, Guy, Dongquan, Kieran, Jide at the CCM for those stimulating discussions and entertaining moments, when there was a chance to see them due to my night shifts.

Staff, students and fellows at Robinson College have helped make my time at Cambridge really enjoyable. Thanks to all my friends here in Cambridge for the enjoyable moments we have shared during these three years. Also to my friends in Athens, Kostas and Stefanos, for not forgetting me and for making my holidays in Greece a real fun.

I am extremely grateful to my parents Violetta and Alexandros for their constant understanding, caring love and support. *Σας ευχαριστώ με όλη μου την καρδιά.*

Finally but most importantly, I would like to thank Georgina for her love, patience and the happy life we share together. *Te amo.*

# Abstract

Failure modes for sandwich beams of GFRP laminate skins and Nomex honeycomb core are investigated. Theoretical models using honeycomb mechanics and classical beam theory are described. A failure mode map for loading under 3-point bending, is constructed, showing the dependence of failure mode and load on the ratio of skin thickness to span length and honeycomb relative density. Beam specimens are tested in 3-point bending. The effect of honeycomb direction is also examined. The experimental data agree satisfactorily with the theoretical predictions. The results reveal the important role of core shear in a sandwich beam's bending behaviour and the need for a better understanding of indentation failure mechanism.

High-order sandwich beam theory (HOSBT) is implemented to extract useful information about the way that sandwich beams respond to localised loads under 3-point bending. 'High-order' or localised effects relate to the non-linear patterns of the in-plane and vertical displacements fields of the core through its height resulting from the unequal deformations in the loaded and unloaded skins. The localised effects are examined experimentally by Surface Displacement Analysis of video images recorded during 3-point bending tests. A new parameter based on the intrinsic material and geometric properties of a sandwich beam is introduced to characterise its susceptibility to localised effects. Skin flexural rigidity is shown to play a key role in determining the way that the top skin allows the external load to pass over the core. Furthermore, the contact stress distribution in the interface between the central roller and the top skin, and its importance to an indentation stress analysis, are investigated.

To better model the failure in the core under the vicinity of localised loads, an Arcan-type test rig is used to test honeycomb cores under simultaneous compression and shear loading. The experimental measurements show a linear relationship between the out-of-plane compression and shear in honeycomb cores. This is used to derive a failure criterion for applied shear and compression, which is combined with the high-order sandwich beam theory to predict failure caused by localised loads in sandwich beams made of GFRP laminate skins and Nomex honeycomb under 3-point bending loading. Short beam tests with three different indenter's size are performed on appropriately prepared specimens. Experiments validate the theoretical approach and reveal the

nature of pre- and post-failure behaviour of these sandwich beams. HOSBT is used as a compact computational tool to reconstruct failure mode maps for sandwich panels. Superposition of weight and stiffness contours on these failure maps provide carpet plots for design optimisation procedures.

**Keywords:**

composite structures, sandwich structures, Nomex honeycomb sandwich beams, failure mode maps, honeycomb anisotropy, indentation, localised effects, high-order sandwich beam theory, mixed failure criterion for honeycombs, biaxial testing of honeycombs

# Contents

Preface and Declaration . . . . .	ii
Acknowledgements . . . . .	iii
Abstract . . . . .	iv
Contents . . . . .	vi
List of Figures . . . . .	viii
List of Tables . . . . .	xi
Nomenclature . . . . .	xii
<b>1 Introduction and Overview</b>	<b>1</b>
1.1 Introduction to Composite Structures . . . . .	1
1.1.1 Fibre Reinforced Polymer Composites . . . . .	2
1.1.2 Structural Optimisation . . . . .	3
1.2 Sandwich Structures . . . . .	4
1.2.1 Previous Work on Indentation Analyses . . . . .	8
1.2.2 Previous Work on Indentation Failure Prediction . . . . .	10
1.3 Scope and Outline of the Thesis . . . . .	12
<b>2 Failure Mode Maps for Honeycomb Sandwich Beams</b>	<b>13</b>
2.1 Introduction . . . . .	13
2.2 Beam Theory for Sandwich Panels . . . . .	14
2.2.1 Skin Failure . . . . .	16
2.2.2 Core Failure . . . . .	17
2.2.3 Honeycomb Mechanics . . . . .	19
2.3 Construction of a Failure Mode Map . . . . .	21
2.3.1 A Failure Mode Map for Beams with a GFRP Skin and Nomex Core . . . . .	23
2.4 Experiments . . . . .	24
2.4.1 Experimental Results . . . . .	28

2.5	Discussion . . . . .	32
2.5.1	Skin Failure . . . . .	32
2.5.2	Core Failure . . . . .	32
2.5.3	Effect of Ribbon Direction . . . . .	32
2.5.4	Intra-cell Buckling . . . . .	33
2.6	Conclusions . . . . .	33
<b>3</b>	<b>Indentation Resistance of Sandwich Beams</b>	<b>36</b>
3.1	Introduction . . . . .	36
3.2	High-Order Sandwich Beam Theory . . . . .	37
3.3	Surface Displacement Analysis . . . . .	40
3.4	Effect of Spreading Stresses . . . . .	43
3.5	Contact Pressure Distribution . . . . .	49
3.5.1	Case Study . . . . .	53
3.6	Concluding Remarks . . . . .	57
<b>4</b>	<b>Indentation Failure Analysis</b>	<b>60</b>
4.1	Introduction . . . . .	60
4.2	Failure Envelope for Nomex Honeycombs . . . . .	60
4.3	Failure Analysis with HOSBT . . . . .	65
4.4	Experimental Work . . . . .	68
4.5	Concluding Remarks . . . . .	72
<b>5</b>	<b>Failure Maps using HOSBT</b>	<b>74</b>
5.1	Introduction . . . . .	74
5.2	Reconstruction of Failure Maps . . . . .	75
5.3	Optimisation Carpet Plots . . . . .	79
5.4	Concluding Remarks . . . . .	82
<b>6</b>	<b>Conclusions and Future Work</b>	<b>83</b>
6.1	Conclusions . . . . .	83
6.2	Future Work . . . . .	86
	<b>Appendix A: Experimental Results</b>	<b>88</b>
	<b>Bibliography</b>	<b>95</b>



# List of Figures

1.1	Sandwich construction with honeycomb core . . . . .	5
1.2	Sandwich panels with (a) corrugated (b) foam and (c) honeycomb core	6
1.3	Typical hexagonal honeycomb with a set of doubled walls. $t'$ is the single wall thickness and $\alpha$ is the honeycomb cell size . . . . .	7
1.4	Test rig for indentation fatigue tests on aircraft floor panels . . . . .	11
2.1	(a) Simply supported beam, (b) Cross section on A-A . . . . .	14
2.2	Failure modes in the skin . . . . .	16
2.3	Failure modes in the core . . . . .	17
2.4	Comparison of theoretical and experimentally measured out-of-plane (a) compressive modulus, (b) compressive strength, (c) shear modulus and (d) shear strength of Nomex honeycombs . . . . .	22
2.5	(a) Failure mode map. Solid lines refer to beams in which the honeycomb ribbon lies along the beam axis; dashed lines for when the ribbon lies transverse to the beam axis. The * symbol identifies experimental measurements described in section 2.4, (b) Failure load surface for ribbon lying along the beam axis . . . . .	25
2.6	Failure mode map for three typical values of $t/L$ and $R/t = 26$ . . . . .	26
2.7	Layup details . . . . .	27
2.8	Test setup . . . . .	28
2.9	Photographs of the different failure modes (for transverse ribbon direction) and corresponding load deflection curves (for both ribbon directions)	30
2.10	Variation of failure load $W_o$ with skin thickness to span ratio $t/L$ . . . . .	31
2.11	Photographs and results of specimens with 13 mm cell size . . . . .	35
3.1	The behaviour of flexible and rigid skins . . . . .	37
3.2	(a) Nonlinear displacement patterns, (b) Beam geometry and stresses. The origin of the z-coordinate is always taken at the top of the beam element, either skin or core, which is being considered . . . . .	39

3.3	Surface Displacement Analysis software window, showing the reference image frame of a side cross section (painted to have a random speckle pattern) and the ‘area of interest’ where the analysis takes place . . . .	42
3.4	Experimental setup . . . . .	42
3.5	Load-deflection and core compression curves. A and B correspond to the frames used for processing by SDA. The dashed line indicates the total midspan core compression at a line load of 6 kN/m . . . . .	44
3.6	Vertical displacement field in the core produced by (a) SDA and (b) HOSBT model. All contour values are in mm and the scaling in both plots is the same . . . . .	45
3.7	Parametric Study; change of transmission coefficient $C_m^{\sigma_{zz}}$ with wavelength $L/m$ for variations in the parameters $t$ , $E_f$ , $c$ and $\rho_c$ . The boxed labels show each time the parameters and the arrows indicate the direction of each parameter’s increase. The position of inflection is marked by a $\circ$ symbol . . . . .	48
3.8	Discrete contact pressure elements; (a) uniform (piecewise constant), (b) overlapping triangles (piecewise linear) and (c) Geometric definitions .	51
3.9	Distributions of contact stresses $q_t/\sigma_{cc}$ and the corresponding normal stresses in the top skin-core interface $\sigma_{zz}/\sigma_{cc}$ (normalised by the core’s out-of-plane compressive strength) for beam A with $\lambda = 0.8$ mm . . . .	55
3.10	Distributions of contact stresses $q_t/\sigma_{cc}$ and the corresponding normal stresses in the top skin-core interface $\sigma_{zz}/\sigma_{cc}$ (normalised by the core’s out-of-plane compressive strength) for beam B with $\lambda = 3.7$ mm . . . .	56
3.11	Dependence of spreading effect on roller’s radius $R$ and determination on how flexible or rigid are the skins with respect to the indentation resistance of the sandwich beam . . . . .	58
4.1	Combined indentation failure mechanism . . . . .	61
4.2	The Arcan-type rig . . . . .	62
4.3	Load paths and determination of failure envelope . . . . .	63
4.4	The three angle setups and the corresponding load-deflection curves (here for specimens with 128 kg/m <sup>3</sup> core density) . . . . .	64
4.5	Failure envelopes for Nomex honeycombs. The dashed line corresponds to the linear failure criterion given by equation (4.1) . . . . .	66
4.6	Combined failure criterion . . . . .	67
4.7	Experimental setup . . . . .	68
4.8	Typical experimental results for sandwich beam with 29 kg/m <sup>3</sup> core density loaded by a roller with diameter of 6 mm. Midspan bottom skin deflection, midspan core compression, and line load are plotted against midspan top skin deflection. Lines legend: (—) longitudinal and (– –) transverse honeycomb ribbon direction . . . . .	70

4.9	The pre-failure influence of core density. Video images captured just before failure during 3-point bending loading with a 6mm diameter central roller . . . . .	71
4.10	The post-failure influence of core density. Video images captured after failure (2 mm total deflection) during 3-point bending loading with a 10mm diameter central roller . . . . .	71
4.11	The post-failure influence of core density on extent of damage. Video images captured after failure (2 mm total deflection) during 3-point bending loading with a 10mm diameter central roller . . . . .	71
4.12	Theory (lines) vs experimental results (symbols) for failure line load $W_o$	73
5.1	Improved failure map for Nomex honeycomb sandwich beams. Each contour represents sandwich beams of equal strength in N/m . . . . .	77
5.2	Comparison with the experimental results from Chapter 2. Lines show the predictions of HOSBT failure analysis and the symbols represent the experimental data (c.f. Fig. 2.10). Solid lines and symbols correspond to the longitudinal ribbon direction, while dashed lines and hollow symbols correspond to the transverse ribbon direction . . . . .	78
5.3	Strength contour plot corresponding to Fig. 5.1 . . . . .	80
5.4	Stiffness contour plot . . . . .	80
5.5	Optimisation carpet plot for $t/L = 5 \times 10^{-4}$ with $\rho_c/\rho_s$ and $c/L$ as design parameters . . . . .	81
6.1	Vertical displacements calculated by Abaqus finite element analysis . .	87
A.1	For 6 mm diameter roller: midspan bottom skin deflection, midspan core compression, and line load variation curves with respect to midspan top skin deflection. Lines legend: (—) longitudinal and (– –) transverse honeycomb ribbon direction . . . . .	89
A.2	For 10 mm diameter roller: midspan bottom skin deflection, midspan core compression, and line load variation curves with respect to midspan top skin deflection. Lines legend: (—) longitudinal and (– –) transverse honeycomb ribbon direction . . . . .	90
A.3	For 20 mm diameter roller: midspan bottom skin deflection, midspan core compression, and line load variation curves with respect to midspan top skin deflection. Lines legend: (—) longitudinal and (– –) transverse honeycomb ribbon direction . . . . .	91
A.4	Video snapshots during loading with a 6 mm diameter roller . . . . .	92
A.5	Video snapshots during loading with a 10 mm diameter roller . . . . .	93
A.6	Video snapshots during loading with a 20 mm diameter roller . . . . .	94

# List of Tables

1.1	An example of structural efficiency of sandwich panels in terms of weight	5
2.1	Summary of failure criteria . . . . .	23
2.2	Material properties of Nomex and laminate skin . . . . .	27
2.3	Experimental results. Photographs of failure given in Fig. 2.9 and 2.11 correspond to the entries in italics in the final column of this table . . .	29
3.1	The range of the geometric and material parameters used in the para- metric study . . . . .	47
3.2	Change of spreading length $\lambda$ . . . . .	49
5.1	Expressions for peak failure loads . . . . .	76

# Nomenclature

## Greek symbols

$\alpha$	Honeycomb cell size
$\delta$	Length of contact between the central roller and the top skin or length of top distributed load
$\theta, \xi$	Quantities defined in section 2.2
$\nu_{cxz}$	Out-of-plane honeycomb Poisson's ratio
$\nu_{fxy}$	Poissons's ratio of the skin material
$\rho_c$	Honeycomb core density
$\rho_s$	Density of honeycomb's constituent material
$\sigma_{cc}$	Out-of-plane compressive strength of the honeycomb core
$\sigma_{fi}$	In-plane compressive stress for intra-cell buckling of the skin
$\sigma_{fw}$	In-plane wrinkling strength of the skin
$\sigma_{fx}$	Maximum in-plane stresses in the skins (Chapter 2)
$\sigma_{fY}$	In-plane yield strength of the skins
$\sigma_{txx}, \sigma_{bxx}$	In-plane normal stresses in the skins
$\sigma_{zz}$	Out-of-plane normal stresses in the core
$\tau_{31}, \tau_{32}$	Out-of-plane shear strength of the honeycomb for transverse and longitudinal ribbon direction respectively
$\tau_{cs}$	Out-of-plane shear strength of the honeycomb core
$\tau_{cxz}$	Maximum shear stresses in the core (Chapter 2)
$\tau_x$	Out-of-plane shear stresses in the core
$\varphi$	Setup angle in Arcan test rig

## Latin symbols

$A_t, A_b$	In-plane rigidity of top and bottom skin
$b$	Beam width
$C_m$	Fourier coefficient
$c$	Core thickness
$D$	Flexural stiffness of the beam
$D_t, D_b$	Flexural rigidity of top and bottom skin

$d$	Distance between the midplanes of top and bottom skin
$E_3$ or $E_c$	Out-of-plane Young's modulus of the honeycomb core
$E_{cx}$	In-plane Young's modulus of the honeycomb core in the $x$ direction
$E_f$ ( $E_{fx}$ )	Young's modulus of the face material (in the $x$ direction)
$E_s$	Young's modulus of the honeycomb's solid material
$G_{31}, G_{32}$	Out-of-plane shear moduli of the honeycomb for transverse and longitudinal ribbon direction respectively
$G_c$ ( $G_{cxz}$ )	Out-of-plane shear modulus of the core (in the $xz$ direction)
$G_s$	Shear modulus of the honeycomb's solid material
$I$	Second moment of area of the sandwich beam
$I_f$	Second moment of area of the skins with respect to their own centroidal axes
$L$	Span of the sandwich beam
long, trans	Longitudinal, transverse honeycomb ribbon direction
$M$	Maximum beam bending moment
$P_i$	Heights of triangular pressure elements (Chapter 3)
$q_i$	Discrete pressure elements (Chapter 3)
$q_t$	External distributed load applied on top skin or contact pressure distribution between the central indenter and top skin
$R$	Roller's radius
$t, (t_t, t_b)$	Skin thickness (top, bottom)
$t'$	Single wall thickness of honeycomb
$u_t, u_b$	In-plane centroidal displacements of top or bottom skin
$v$	Base width of triangular pressure elements (Chapter 3)
$W$ ( $W_o$ )	Load per unit width (at failure)
$w_t, w_b$	Vertical displacements of top or bottom skin
$w_c$	Vertical displacements in the core
$x, y, z$	Coordinates of sandwich beam

Note: Other symbols not mentioned are defined in the text or figure when appearing

# Chapter 1

## Introduction and Overview

One day, towards the end of 1943, a circus proprietor called George May called to see me at Farnborough. After he had told me several Gerald Durrell-type stories about the difficulties of keeping monkeys in travelling circuses, he produced something which looked like a cross between a book and a concertina. When he pulled on the ends of this invention, the whole thing opened out like one of those coloured-paper festoons which people use for Christmas decorations. It was in fact a sort of paper honeycomb of very light weight but of quite surprising strength and stiffness. Did I think that such a thing could be of any use in aircraft? The snag, as George May modestly admitted, was that, since it was only made from brown paper and ordinary gum, it had no moisture resistance at all and would fall to bits if it got wet.

This must have been one of the relatively few occasions in history when a group of aircraft engineers have been seriously tempted to throw their collective arms around the neck of a circus proprietor and kiss him. However, we resisted the temptation and told May that there could be no serious difficulty in waterproofing the paper honeycomb by means of a synthetic resin.

J.E. Gordon ‘*Structures: or, why things don’t fall down*’ [1]

### 1.1 Introduction to Composite Structures

Innovative, high performance design of load-bearing components is always sought in high-tech applications, such as aircrafts, spacecrafts, satellites or F1 racing cars. These structures should be as as light as possible, while having high stiffness, sufficient strength, and some damage tolerance. This requires *structurally efficient* construction. Structural efficiency can be maximised by using the most efficient materials and optimising the structure’s geometry. To produce an optimum design, both these factors need to be considered throughout the design process.

The catalogue of materials is one of forbidding length. Thus a designer needs a systematic way to be guided through the maze of material classes so as to gradually narrow down the material choices and choose the optimum material. Ashby [2] proposed a material selection procedure, using material selection charts. Birmingham *et al.* [3] have introduced an integrated approach to the assessment of alternative

materials and structural forms at the concept stage of structural design based on the above methodology.

### **1.1.1 Fibre Reinforced Polymer Composites**

Fibre Reinforced Polymer (FRP) composite materials are some of the most useful materials available to the designer of high performance structures in the aerospace or maritime industries because their high specific strength and stiffness can lead to significant weight reductions. The aerospace industry has proved the effectiveness of composite materials in reducing component weight and increasing fuel economy. In the marine field, the use of composites has been growing steadily since the early 1950's, particularly driven by the low construction costs of Glass FRP's. Initial applications include small crafts, lifeboats and pleasure crafts. Potential applications are radar domes, masts and piping, ship hulls, ship superstructures, submersibles and offshore structure modules. Yachts participating in the America's Cup race have all-composite hull, keel and mast. Racing car bodies are made of composites providing more safety per unit weight to drivers. In the last decade composites have been used in applications outside the aerospace industry. Sporting goods such as tennis and squash rackets, golf shafts, bicycles and oars are a major outlet for composites materials. Future applications include high speed trains, subway cars and surface ships [4]. As well as weight reductions, other benefits of composites include their ability to cope with extreme environment, reliability, maintainability, life cycle cost and service life extension. Despite all their advantages, composites are still regarded as expensive materials to purchase, tool up for and work with.

When using composites, a designer has the freedom to tailor the properties. Although this can improve the structural efficiency, this also increases the complexity and number of design parameters. Many design tools have been developed to predict their behaviour and so decrease the level of empiricism, which has been used up to now in design procedures. Finding an efficient composite structural design that meets the requirements of a given application can be achieved not only by sizing the cross-sectional areas and members thicknesses, but also by global or local tailoring of the material properties through selective use of orientation, number and stacking sequence of laminae that make up the laminate composite [5]. A comprehensive presentation of the equations which govern the mechanical behaviour of laminates can be found in Hull's book [6]. Stress analysis for the design of composites laminates is commonly implemented by the use of computer programs (i.e. Cambridge Composite Designer [7]) based on laminated plate theory (LPT).



This kind of software is convenient, efficient and user-friendly, but does not help determine the optimum laminate configuration or choose the best material system. For this purpose there are procedures which are based on the use of carpet plots, which are themselves generated using LPT principles, but also provide a graphic illustration of the whole range of elastic properties available with chosen system [8]. Miki [9] describes a highly practical tool for design optimisation of laminates based on a graphical procedure. Tsai and Patterson [10] have introduced the laminate ranking method for selecting the optimum ply angles. Recently Quinn [11] has published a design manual for composites, which provides practical information for engineers to facilitate the design of GRP, CFRP, A(ramide)RP composites. Quinn has also introduced a relevant nomogram [12, 13], which allows the costs of the constituent materials (fibres, matrix) in a composite to be quickly assessed.

### **1.1.2 Structural Optimisation**

The design of full scale composite materials structures usually requires a building block approach to testing and design [14]. This approach involves increasing the testing complexity and size from coupon tests to full structural tests. The chemical and material tests in the first stages are generally well defined tests. As we move from the laminate level to sub-element, component and sub-structure level, the test become more application-dependent. Neither standard test methods nor databases exist for these larger tests. Thus there is a need to reduce cost and increase the efficiency of structural design and structural failure prediction by a global/local testing and analysis approach. The global/local approach involves supporting the global tests and analyses, used in traditional design approaches, by critical local sub-element tests. These tests are intended to be in between a coupon and sub-structure test. They are cheaper to manufacture and test and most importantly they are fully representative of structural configurations undergoing the same manufacturing processes, and may even be cut from an actual structure.

A major constraint to overcome in the design and construction of large fibre-reinforced plastic (FRP) structures (e.g. in ship hulls or aircraft wings) is the flexibility of the panels. Although this can be overcome by large increases in thickness, this causes molding difficulties and is also very uneconomical. A more satisfactory alternative is the use of stiffeners, which are commonly in the form of top-hats, I-beam, tee-joint, or by use of sandwich constructions [15, 16]. The stiffeners may be an integral part of the shell or they may be attached by adhesive bonding (the latter is the usual case). Bonded or laminated connections between two structural members represent a zone of

potential weakness.

Recent studies have resulted in computer codes for design of specific stiffened panel configurations subject to simple loadings (usually compression). In the 1980s, a computer code PASCO (Panel Analysis and Sizing Code) was developed by NASA [17], which has been widely used for composite optimization procedures [18]. The code has been designed to have sufficient generality in terms of panel configuration, loading, and practical constraints so that it can be used for final sizing of panels in a realistic design situation. The UWCODA (University of Washington Composite Optimization and Design Algorithm) design-analysis-optimization software tool was originally developed to optimise the lay-up of flat composite panels. In the UWCODA analysis both ply orientation angles and stiffener geometries are treated as design variables. Optimum designs are sought [19] which minimise structural weight and satisfy mechanical performance requirements, for example maximum strain and minimum strength.

Especially within the aircraft industry, finite element based optimisation methods are used to size complex structures for minimum weight taking into account a variety of constraints including strength, stiffness and aeroelasticity. However there is always a need for simple low-cost direct methods, which can assist in configurations and weight studies at the initial design stage. Bartholomew [20, 21, 22] apply a simple optimization method known as geometric programming (GP) [23]. In this method the minimisation of a function representing weight or cost subject to non-linear constraints on the variables can sometimes be reduced to the solution of linear equations.

## **1.2 Sandwich Structures**

Amongst all possible design concepts in composite structures, the idea of sandwich construction has become increasingly popular because of the development of man-made cellular materials as core materials. Sandwich structures consist of 1) a pair of thin stiff, strong skins (faces, facings or covers); 2) a thick, lightweight core to separate the skins and carry loads from one skin to the other; and 3) an adhesive attachment which is capable of transmitting shear and axial loads to and from the core (Fig. 1.1). The separation of the skins by the core increases the moment of inertia of the panel with little increase in weight, producing an efficient structure for resisting bending and buckling loads. Table 1.1 shows illustratively the flexural stiffness and strength advantage of sandwich panels compared to solid panels using typical beam theory with typical values for skin and core density. By splitting a solid laminate down the middle and separating the two halves with a core material, the result is a sandwich panel. The

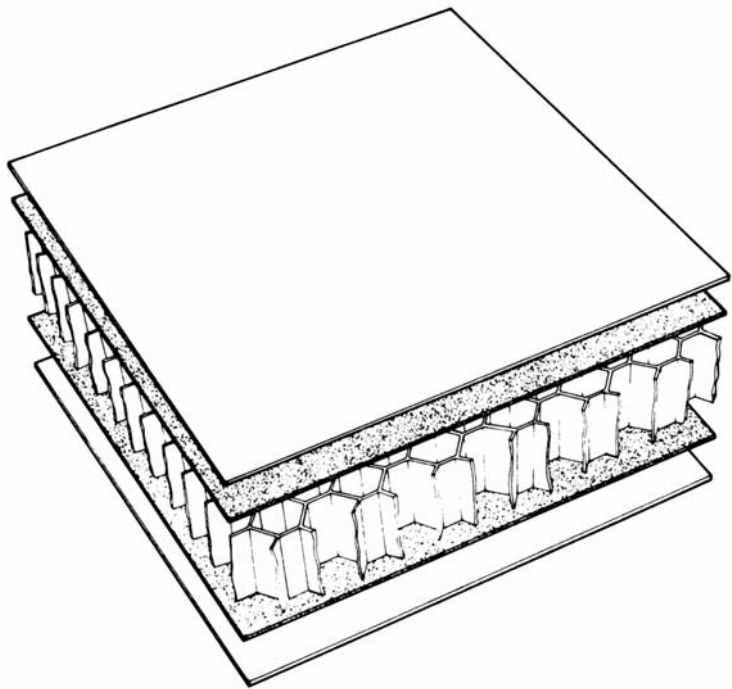
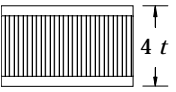

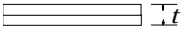


Figure 1.1: Sandwich construction with honeycomb core

new panel weighs little more than the laminate, but its flexural stiffness and strength is much greater; by doubling the thickness of the core material, the difference is even more striking.

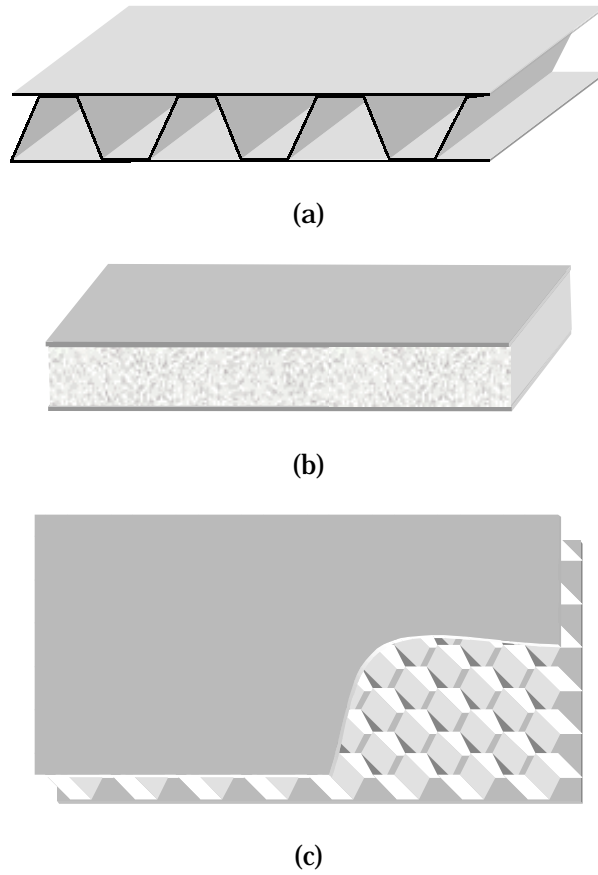
Thus sandwich panels are popular in high performance applications where weight must be kept to a minimum, for example aeronautical structures, high-speed marine craft and racing cars. In the most weight-critical applications, composite materials are used for the skins; cheaper alternatives such as aluminium alloy, steel or plywood are also commonly used. Materials used for cores include polymers, aluminium, wood and composites. To minimise weight these are used in the form of foams, honeycombs or with a corrugated construction (Fig. 1.2). As well as mechanical requirements, core



Relative Bending Stiffness	1	7.0	37
Relative Bending Strength	1	3.5	9.2
Relative Weight	1	1.03	1.06

Table 1.1: An example of structural efficiency of sandwich panels in terms of weight

materials may also be selected based on their fire-resistance or thermal properties.



**Figure 1.2:** Sandwich panels with (a) corrugated (b) foam and (c) honeycomb core

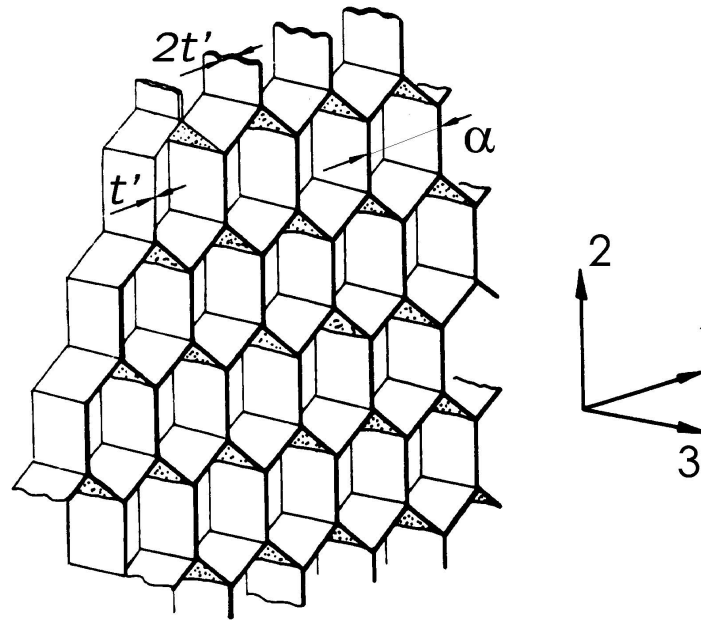
The most common and some unorthodox techniques employed to manufacture sandwich components for structural applications, as well as the recent developments and future trends in terms of both materials and processing routes are comprehensively reviewed by Karlsson [24].

Sandwich panels will have stiffness and strength criteria to meet. The stiffness of honeycomb sandwich panels is straightforward to predict, but it remains difficult to estimate the strength. Typical modes of failure are face yielding, face wrinkling, intra-cell dimpling, core shear or local indentation (where the load is applied to the panel). These are described in detail in section 2.2. The critical failure mode and the corresponding failure load depend on the properties of the face and core materials, on the geometry of the structure and on the loading arrangement.

Proper analysis of sandwich structures demands a thorough understanding of the mechanical behaviour of both the skins and the core. The skins behave in a relatively simple manner and, in case of composite laminates, the aforementioned methods of

analysis (i.e. laminated plate theory) facilitate the modelling procedure. However, the mechanical modelling of the core material, particularly for foams or honeycombs, is less straightforward. The response of the core to shear loading from the skins or loading normal to the plane of skins is required. The behaviour depends both on the materials used in the core and on the core relative density, which is the ratio of the core density to that of the solid material constituting the core. Gibson and Ashby [25] give a thorough overview of the literature on cellular materials, quoting many results for foam cores.

Figure 1.3 illustrates the honeycomb structure. One of the most common core materials is Nomex honeycomb<sup>1</sup>, because it possesses an extremely high strength-to-weight ratio. It is also electrically and thermally insulating, chemically stable, self-extinguishing and corrosion as well as shock and fatigue resistant. As Nomex is used extensively in this thesis, the make-up of this core is described in detail here. Nomex is constructed from ribbons of aramid paper running in the 2 direction (the longitudinal ribbon direction). These are glued together at intervals along the ribbon and the stack of ribbons is then expanded into a honeycomb by pulling in the 1 direction (transverse). The paper substrate is finally dipped into phenolic resin to build up the walls of the honeycomb. Because of this construction method, the honeycomb is anisotropic with respect to out-of-plane shear stiffness and strength.



**Figure 1.3:** Typical hexagonal honeycomb with a set of doubled walls.  $t'$  is the single wall thickness and  $\alpha$  is the honeycomb cell size

<sup>1</sup>Nomex is a Du Pont trademark

Zhang [26] and Ashby [27] model the elastic and collapse behaviour for Nomex honeycomb materials under shear and out-of-plane compression. Their models agree well with experiments that they made on a wide range of Nomex honeycombs. Zhang and Ashby [28] have also investigated the in-plane biaxial buckling behaviour of Nomex honeycombs. Shi *et al.* [29] and Grediac [30] model the transverse shear modulus of a honeycomb core.

Considerable effort has been devoted to the analysis of beams, panels and struts of sandwich construction and the results have been summarised in the books of Allen [31] and Plantema [32]. Modelling a sandwich panel as a beam, with the simplifying assumptions that the skins are thin relative to the core and that the core material is homogeneous and much less stiff than the skin material, was presented by Allen [31] and developed by Gibson and Ashby [25]. Triantafillou and Gibson [33] have developed an optimisation procedure which can determine the optimum values of skins' and core's thicknesses that satisfy the stiffness constraint at minimum weight. Although most of research work in literature is concerned with bending loading of sandwich beams, Kwon *et al.* [34] or Pearce [35] have investigated the overall buckling and wrinkling of sandwich panels under in-plane compression.

A recent comprehensive review to the subject of sandwich construction and the development of theoretical analyses up to now is given in the book of Zenkert [36]. Holt and Webber [37] summarise recent developments and analyse the elastic behaviour of honeycomb sandwich beams, assuming linear elastic behaviour for the skin and the core. Mechanical, thermal, and hygrometric loading on a sandwich beam with a honeycomb core and laminated facings are included in reference [38]. Failure mode maps have been derived by various authors for sandwich panels with flexible cores [39, 40, 41]. These authors have been particularly concerned with beams with ductile foam cores, making appropriate assumptions about the elastic and plastic behaviour of the core and skin. However there appears to be little work on failure of panels with honeycomb cores, whose shear anisotropy can reveal the important role of core shear in the bending of sandwich beams. Furthermore resistance to indentation failure is rarely considered as an important factor, although it can be important in determining the durability and service life of the structure.

### 1.2.1 Previous Work on Indentation Analyses

The use of flexible foams and non-metallic honeycombs as core materials has introduced a new design difficulty; they are transversely flexible compared to the effectively incompressible metallic honeycombs or rigid foam cores. This leads to significant lo-

cal deflections of the loaded skin into the core material, hence to indentation failure. Indentation failure of sandwich structures has been primarily investigated for aircraft floor panels. These panels need to be sufficiently stiff to avoid passengers perceiving that the floor is unsafe because of its deflection. High heel shoes or dropped objects are typical causes for local indentations on the top skin of these panels in areas like the aisles, thresholds, toilets/galley. However, a sandwich panel would continue to give good service until a number of such indentations had been made. Therefore, the time from incipient to final failure should be sufficient to allow maintenance operators to change a defective panel at the next convenient check.

A good source of information on indentation analyses of sandwich beams are the books by Allen [31] and Plantema [32]. They cover the development of the theoretical analyses based on a so-called ‘splitted rigidity’ model. This approach assumes that the beam consists of a component with only bending rigidity and a component with only shear rigidity. They are connected through equilibrium, assuming that the shear resultants in the two components are the same. These models offers an adequate level of accuracy for sandwich structures with incompressible cores, but are inadequate for non-metallic honeycomb sandwich panels, since they neglect localised effects, which play an important role for these flexible cores.

To model indentation failure of transversely flexible cores in sandwich structures requires the use of models that take into account the compressibility of the core in the vicinity of the applied loads. A common approach is the *elastic foundation* model. Selvadurai [42] presents the principles of these models. Their application in sandwich structures analysis is described in Zenkert’s book [36]. The simplest of these is the one-parameter Winkler foundation model, which treats the core material as a set of continuously-distributed linear springs. However, its main drawback is that it neglects shear interactions between the loaded skin and the core. The elastic foundation approach adopted by Thomsen [43, 44] was based on the use of a two-parameter elastic foundation model including the shear interaction between the skins and the core. Typical two-parameter models are those of Pasternak or Vlasov (see Selvadurai [42]).

Nevertheless these elastic foundation models neglect the interaction between the top and bottom skin. A different approach by Frostig and Baruch [45] consists of treating the beam as an ordinary incompressible sandwich substructure interconnected with a special elastic foundation substructure, which provides the localised effects due to the different displacements of the upper and lower skins. The non-planar deformed cross section of the sandwich beam which is observed by experiments suggested the need for a model which allows non-linear variations of in-plane and vertical displacement

field through the core. Frostig *et al.* [46, 47] used variational principles to develop the high-order sandwich panel theory, which includes the transverse flexibility of the core. ‘High-order’ refers to the non-linear way in which the in-plane and vertical displacements are allowed to vary through the height of the core, in contrast to simple beam theory where the core in-plane displacements are assumed to vary in a linear way through the depth, and the out-of-plane displacements are assumed to be constant. The high-order theory enables the prediction of localised effects under conditions such as concentrated loads, delamination and diaphragms [48], curved sandwich panels [49], hygrothermal (environmental) effects and discontinuous skins [50]. A comprehensive review and comparison between this method and conventional beam theories was presented recently by Frostig [51].

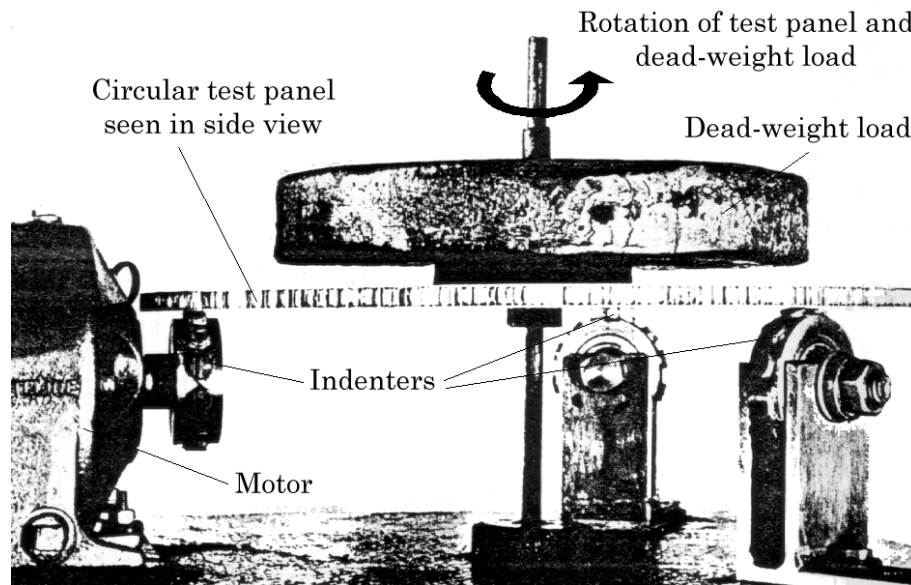
In the literature the importance of the core behaviour in affecting indentation failure has been considered; however, the influence of the skin’s flexural rigidity is generally overlooked. This omission derives from the fact that in practical applications the skins are quite stiff and the influence of skin flexural rigidity can be neglected. One of the main aims of this thesis is to focus on the role of skin rigidity in indentation failure and give a better insight in the mechanism of indentation.

### 1.2.2 Previous Work on Indentation Failure Prediction

The aircraft industry, in collaboration with sandwich panel manufacturers, has conducted research to establish design codes for indentation resistant and cost effective sandwich panels [52]. However most of the design specifications have been based on experimental results rather than accurate theoretical models. In manufacturers’ data sheets [53] and handbooks [54] the prediction of indentation failure load is derived as a product of the out-of-plane compressive strength of the core and the area over which the load is applied. However, such an approach is at best approximate. Special experimental setups have been introduced depending on the application; static blunt indentation tests for freight floors or dynamic fatigue tests for cabin floors. Bonded Structures Division CIBA (now Hexcel Composites) have devised the ‘fatigue wheel’ machine (Fig. 1.4) to provide data on the relative performance of various sandwich panels.

Similar indentation damage accumulation can be observed in sandwich panels used as a part of control surfaces (flaps, ailerons), in this case because of hail or stone impacts. A strength analysis of the damaged sandwich panels is essential to predict the influence of the multi-site damage. Razi *et al.* [55] have introduced an analytical method to determine the stress distribution in sandwich panels with damage that is





**Figure 1.4:** Test rig for indentation fatigue tests on aircraft floor panels

elliptical or circular in shape and at an arbitrary location.

The low-velocity or quasi-static impact behaviour of sandwich panels is also another aspect of the whole indentation problem that has been investigated by several authors. The lack of accepted test methods for measuring impact damage resistance of composite sandwich structures led Lagace *et al.* [56] to propose a new methodology based on static indentation and impact tests. Mines *et al.* [57, 58] have tested the dropped weight impact performance of sandwich beams with woven/chopped strand glass skins and polyester foam and aluminium honeycomb cores and have simulated the upper skin post-failure energy absorption behaviour with an elastic-plastic beam bending model. Low velocity damage mechanisms and damage modes have been investigated in sandwich beams with Rohacell foam core by Wu and Sun [59] and with Nomex honeycomb core by Herup and Palazotto [60].

The pure static indentation response of composite sandwich beams has been modelled as linear elastic bending of the top skin on a rigid-perfectly plastic foundation (the core) by Soden [61] and Shuaib [62]. Olsson and McManus [63] introduced a theory for contact indentation of sandwich panels; the model is based on the assumption of axisymmetric indentation of an infinite elastic face sheet bonded to an elastic-ideally plastic core on a rigid foundation. Despite the usefulness of such models for analysing sandwich beam indentation behaviour, they are restricted only to the loading case where a sandwich beam is indented on a rigid foundation. However this loading case is not normal in practice. Most sandwich beams in service are simply supported or

clamped and are indented whilst also suffering bending loads. These loading conditions make the influence of the bottom skin an important factor in the overall behaviour of a sandwich beam under localised loads.

### 1.3 Scope and Outline of the Thesis

The use of laminate composites as skins and low density cellular materials as cores in sandwich constructions has enabled a very good utilisation of the constituent materials, providing structural components with high stiffness and strength-to-weight ratios. Non-metallic honeycombs are popular in high performance applications because of their good mechanical properties, excellent resistance to hostile environments and better fatigue resistance than aluminium. However, because of the low stiffness of the core, they are susceptible to indentation failure. The need to take into consideration the indentation resistance of sandwich panels when optimising their design and the importance of having a robust computational tool to predict indentation failure in sandwich beams under bending, have been the main motivations for this thesis.

To address design including indentation failure, we first need to investigate the other failure mechanisms described in Chapter 2. Failure maps for loading under 3-point bending are constructed and the region, where indentation failure is important, is identified. This work uses sandwich panels made of GFRP laminates and Nomex honeycomb cores of various densities. Experimental measurements are compared with simple theoretical predictions. In Chapter 3 analytical modelling which can be used for indentation failure is addressed. This uses an existing beam theory developed by Frostig *et al.* [46, 47] and applies it to the GFRP - Nomex construction considered in the thesis. The effect of material properties and the beam and indenter geometry on the beam response are considered. Chapter 4 presents the methodology to predict more accurately indentation failure loads. This is achieved by introducing a new failure criterion for honeycomb core, which takes into account both the out-of-plane normal compression stresses and the shear stresses in the core. Theoretical predictions are compared with experimental data. Refined failure maps including the new indentation analysis are described in Chapter 5. Carpet plots based on these failure mode maps provide a preliminary optimisation methodology for minimum weight design of sandwich beams. The thesis concludes in Chapter 6 by summarising the main results of this research together with a discussion of new research directions.

## Chapter 2

# Failure Mode Maps for Honeycomb Sandwich Beams

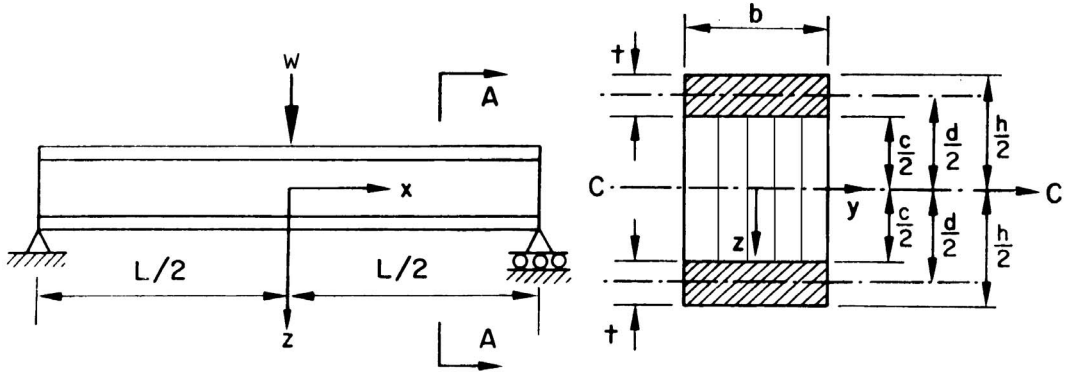
### 2.1 Introduction

In this chapter we consider loading under three-point bending of sandwich beams made with honeycomb and skins, both of which fail in a brittle manner. We apply the analysis framework and failure mode map technique used by Triantafillou and Gibson [41] for ductile foam cores and ductile skin materials. However here we investigate the failure modes of panels with honeycomb cores, whose shear anisotropy can reveal the important role of core shear in the bending of sandwich beams. Furthermore the constructed failure mode maps include indentation failure and identify for what beams this mechanism will be important.

In section 2.2 we review beam theory for sandwich panels. Section 2.2.3 describes existing work on honeycomb mechanics. By combining the analysis for sandwich beams with the honeycomb mechanics, we derive in section 2.3 failure loads for the various failure mechanisms. This information is used in section 2.3.1 to draw up failure mode maps, in which the mechanisms of failure and the corresponding failure loads are plotted as a function of the core relative density and skin thickness/span ratio. Theoretical results are illustrated using the commercially-popular combination of laminated glass fibre reinforced plastic (GFRP) skins and Nomex core. Theory is compared in section 2.4 with experiments on sandwich panels of various core relative densities and skin thickness/span ratios.

## 2.2 Beam Theory for Sandwich Panels

In this section we outline the elastic analysis of sandwich beams in three point bending. This will be used to evaluate the stresses in the core or skin and hence the failure loads due to the various mechanisms. Consider a simply supported sandwich beam of span  $L$  and width  $b$  loaded in 3-point bending with a central load  $W$  per unit width as illustrated in Fig. 2.1. The skins each have thickness  $t$  and are separated by a thick layer of honeycomb core of thickness  $c$ .



**Figure 2.1:** (a) Simply supported beam, (b) Cross section on A-A

We assume that the skins remain firmly bonded to the core, that the beam bends in a cylindrical manner with no curvature in the  $yz$ -plane and that cross-sections remain plane and perpendicular to the longitudinal axis of the beam. The flexural rigidity  $D$  of the sandwich beam is then given by

$$D = \frac{E_{fx}bt^3}{6} + \frac{E_{fx}btd^2}{2} + \frac{E_{cx}bc^3}{12} \quad (2.1)$$

where  $d$  is the distance between the midplanes of the upper and bottom skins.  $E_{fx}$  and  $E_{cx}$  are the in-plane Young's moduli of the skin and core respectively for loading in the  $x$  direction (along the axis of the beam). Subscripts ' $f$ ' and ' $c$ ' denote the face material and the honeycomb core respectively. Subscript ' $s$ ' is used in later expressions for the solid material from which the honeycomb is made. The three terms on the right hand side of (2.1) correspond to bending of the skins about their centroidal axes, bending of the skins about the centroid of the whole beam, and bending of the core, respectively. We can simplify this equation by assuming that bending of the skins about the centroid of the beam is the dominant term. The contributions of the first

and third terms amount to less than 1% of this when

$$\frac{d}{t} > 5.77 \quad \text{and} \quad \frac{E_{fx}}{E_{cx}} \frac{t}{c} \left( \frac{d}{c} \right)^2 > 16.7 \quad (2.2)$$

respectively, so that (2.1) becomes

$$D = E_{fx} \frac{btd^2}{2} = E_{fx} I \quad (2.3)$$

where  $I$  is second moment of area of the cross-section of the sandwich beam. With 3-point bending the maximum bending moment  $M$  is at the mid-span and the corresponding maximum stress  $\sigma_{fx}$  in the skins is given by

$$\sigma_{fx} = \frac{ME_{fx}}{D} \frac{d}{2} = \frac{WL}{4dt} \quad (2.4)$$

However, the above theoretical model neglects the effect of shear deflection in the core, which becomes significant for low density cores. Inclusion of this effect also allows a prediction of observed differences in beam strength for different orientations of the honeycomb ribbon (see section 2.2.3 for further details). For the above reasons we follow the suggestion of Allen [31] for the maximum axial stresses in the faces

$$\sigma_{fx} = \frac{WbL}{4} \left( \frac{c+2t}{2I} + \frac{WL}{4} \frac{t}{2I_f} \frac{1}{\theta} \right) \quad (2.5)$$

$$\text{where} \quad \theta = \frac{L}{c} \left[ \frac{G_{cxz}}{2E_{fx}} \frac{c}{t} \left( 1 + \frac{3d^2}{t^2} \right) \right]^{\frac{1}{2}}, \quad I = \frac{bt^3}{6} + \frac{btd^2}{2}, \quad I_f = \frac{bt^3}{6} \quad (2.6)$$

$G_{cxz}$  is the out-of-plane shear modulus of the core,  $I$  is the second moment of area of the sandwich with respect to its neutral axis and  $I_f$  is the second moment of area of the faceplates with respect to their own centroidal axes<sup>1</sup>. Equation (2.6) shows that  $\theta$  depends on the relative stiffness of the skin and the core. Finally (2.5) gives

$$W = 4\sigma_{fx} \xi \frac{t}{L} \quad (2.7)$$

$$\text{where} \quad \xi = \theta \frac{t^5/9 + t^3d^2/3}{ht^3(\theta - 1)/3 + t^4/3 + t^2d^2} \quad (2.8)$$

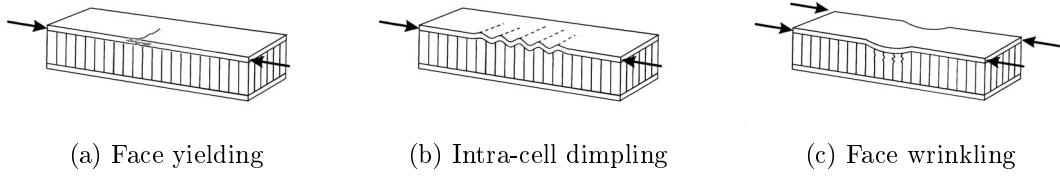
As the span length  $L$  or the core shear stiffness  $G_{cxz}$  approach infinity, (2.7) tends to the simple beam model (2.4). In the case study presented in section 2.3.1, maximum deviations from the simple beam model due to the finite thickness of the skins and the effect of finite shear stiffness in the core amount to a maximum of 26%.

---

<sup>1</sup>Note that  $I_f$  is not negligible in this approach

### 2.2.1 Skin Failure

Section 2.2 gives an expression for the maximum stress  $\sigma_{fx}$  in the skins. This can be used to predict beam failure due to the skin failure modes of face yielding, intra-cell dimpling or face wrinkling, as illustrated in Fig. 2.2.



**Figure 2.2:** Failure modes in the skin

#### Face Yielding

Failure occurs in the top skin due to face yielding when the axial stress in either of the skins [equation (2.5)] reaches the in-plane strength  $\sigma_{fY}$  of the face material for loading along the beam axis,

$$\sigma_{fx} = \sigma_{fY} \quad (2.9)$$

It is assumed that the skin behaves in a brittle manner. With a symmetrical beam the stress is the same in the tension and compression faces. For composite face materials the compressive face is generally the critical one.

#### Intra-cell Dimpling

A sandwich with a honeycomb core may fail by buckling of the face where it is unsupported by the walls of the honeycomb (Fig. 2.2b). Simple elastic plate buckling theory can be used to derive an expression for the in-plane stress  $\sigma_{fi}$  in the skins at which intra-cell buckling occurs as

$$\sigma_{fi} = \frac{2E_{fx}}{1 - \nu_{fxy}^2} \left( \frac{2t}{\alpha} \right)^2 \quad (2.10)$$

where  $\alpha$  is the cell size (i.e. the diameter of the inscribed circle) of the honeycomb and  $E_{fx}$  and  $\nu_{fxy}$  are the elastic modulus and Poisson's ratio for the skin for loading in the axial direction. A similar expression, verified experimentally by Kuenzi [64], has been given by Norris [65]. Equations (2.9) and (2.10) can be used to derive the value of cell

size above which there is transition from face yielding to intra-cell buckling as

$$\alpha = 2t \sqrt{\frac{2}{1 - \nu_{fxy}^2} \frac{E_{fx}}{\sigma_{fY}}} \quad (2.11)$$

### Face Wrinkling

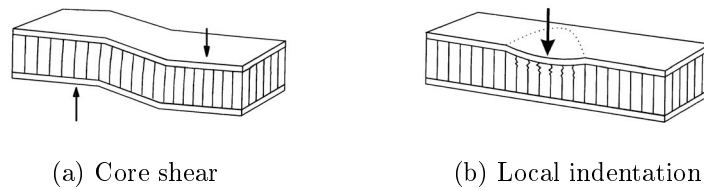
Face wrinkling is a buckling mode of the skin with a wavelength greater than the cell width of the honeycomb (Fig. 2.2c). Buckling may occur either in towards the core or outwards, depending on the stiffness of the core in compression and the adhesive strength. In practice, with 3-point bending, inward wrinkling of the top skin occurs in the vicinity of the central load. By modelling the skin as a plate on an elastic foundation, Allen [31] gives the critical compressive stress  $\sigma_{fw}$  that results in wrinkling of the top skin as

$$\sigma_{fw} = \frac{3}{(12(3 - \nu_{cxz})^2(1 + \nu_{cxz})^2)^{-1/3}} E_{fx}^{1/3} E_3^{2/3} \quad (2.12)$$

where  $\nu_{cxz}$  is the out-of-plane Poissons ratio and  $E_3$  the out-of-plane Young's modulus of the honeycomb core (see section 2.2.3).

### 2.2.2 Core Failure

Honeycomb sandwich structures loaded in bending can fail due to core failure. Pertinent failure modes are shear failure or indentation by local crushing in the vicinity of the loads, as illustrated in Fig. 2.3.



**Figure 2.3:** Failure modes in the core

#### Core Shear

Assuming simple beam behaviour, the shear stress varies through the face and core in a parabolic way under 3-point bending. If the faces are much stiffer and thinner than the core, the shear stress can be taken as linear through the face and constant in the

core. Neglecting the contribution from the skins, the mean shear stress in the core is given by

$$\tau_{cxz} = \frac{W}{2d} \quad (2.13)$$

Assuming brittle behaviour, failure occurs when the applied shear stress  $\tau_{xz}$  equals the shear strength  $\tau_{cs}$  of the honeycomb core in this direction.

$$\tau_{cxz} = \tau_{cs} \quad (2.14)$$

Low density Nomex cores are particular susceptible to this failure mode. Due to the anisotropy of the honeycomb structure (section 2.2.3) the shear strength of the core depends on the loading direction.

### Local Indentation

Failure of sandwich panels in 3-point bending can occur at the load point due to local indentation. Failure is due to core crushing under the indenter. The bending stiffness of the skin and the core stiffness determine the degree to which the load is spread out at the point of application. It is important here to mention the main failure characteristic by which indentation differs from skin wrinkling. In indentation the top skin deflects after failure with a wavelength of the same scale as the indenter-top skin contact length, whereas in skin wrinkling the deflection of the top skin after failure exhibits wavelengths that are larger than the contact length between the indenter and the top skin.

Indentation failure has not been adequately modelled for honeycomb sandwich panels. To include this important failure mechanism, we use a simple empirical approach used in handbooks on sandwich panel construction [53]. In the next chapters a more accurate model will be presented for indentation failure prediction. Here we assume that we know the length<sup>2</sup> of contact  $\delta$  between the central roller and the top skin. It is further assumed that the load is transferred uniformly to the core over this contact length, so that the out-of-plane compressive stress  $\sigma_{zz}$  in the core is given by

$$\sigma_{zz} = W/\delta \quad (2.15)$$

Failure is then predicted when this compressive stress equals the out-of-plane compressive strength  $\sigma_{cc}$  of the honeycomb core.

$$\sigma_{zz} = \sigma_{cc} \quad (2.16)$$

---

<sup>2</sup>This length derives from the assumption that the skins are ‘transparent’ enough to equate the contact length with the length of initial damage in the top skin-core interface



The above approach is deficient in three respects (i) the contact area must be estimated in some way - in the experiments described in section 2.4 this is measured, (ii) load transfer from the roller to the core is over-simplified; this will depend on the relative skin and core stiffnesses, (iii) failure in the core will not be governed solely by the compressive stress in the core but will also be influenced by the local shear stress. A more rigorous stress analysis of the contact region can be found in Chapter 3 and its implementation to predict local failure in honeycomb panels is presented in Chapter 4.

### 2.2.3 Honeycomb Mechanics

To evaluate the failure mechanisms described in section 2.2, stiffness and strength properties for the honeycomb core are required. In this section we use the results of references [25, 27] to express the properties of the honeycomb as a function of the properties of the solid material from which the honeycomb is made and the relative density  $\rho_c/\rho_s$  of the honeycomb. Although the theory is applicable to any honeycomb, in practice we will focus on the Nomex honeycomb core used in the beam failure experiments of section 2.4. Expressions are compared with published experimental data to evaluate the applicability of the theoretical models to the Nomex honeycomb core and to find the most suitable expressions for use in the beam calculations. The following notations ‘1’, ‘2’, ‘3’ for honeycomb’s main axes refer to those illustrated in Fig. 1.3.

The honeycomb Poisson’s ratio  $\nu_{cxz}$  required for the failure analysis (section 2.2.1) is  $\nu_{13}$  or  $\nu_{23}$  for in-plane Poisson strains due to out-of plane loading in the 3 direction. To a first approximation its value can be taken as that of the solid material (eq. (4.64) in ref.[25]), i.e.  $\nu_{13} = \nu_{23} = \nu_s$ .

The Young’s modulus of the honeycomb in the out-of-plane 3 direction is given by the rule of mixtures expression

$$\frac{E_3}{E_s} = \frac{\rho_c}{\rho_s} \quad (2.17)$$

In honeycombs, failure under out-of-plane compressive stresses occurs due to fracture of the cell walls or due to elastic or plastic buckling of the cell walls [26]. For Nomex honeycombs failure is due to a ‘crushing’ mechanism, initiated by elastic buckling and developing as a plastic buckling process. The relevant collapse strength  $\sigma_{cc}$  can be simply estimated using the rule of mixtures expression,  $\sigma_{cc}/\sigma_{sc} = \rho_c/\rho_s$ , where  $\sigma_{sc}$  is the compressive strength of the solid from which the core is made. Wierzbicki [66] gives an alternative expression for the failure stress based on a plastic collapse model. For a

honeycomb with regular hexagonal cells this approach predicts the collapse strength

$$\sigma_{cc} = 3.25\sigma_{sc} \left( \frac{\rho_c}{\rho_s} \right)^{5/3} \quad (2.18)$$

Zhang and Ashby [27] show that the out-of-plane shear strength and stiffness of honeycombs are independent of height and cell size. Honeycomb cores exhibit slight anisotropy in their out-of-plane shear strength and stiffness, due to the set of doubled walls. By using simple mechanics models based on an array of regular hexagons and considering the double wall effect approximate expressions for the shear strengths  $\tau_{31}$  and  $\tau_{32}$  are derived as

$$\frac{\tau_{31}}{E_s} = 1.7 \left( \frac{\rho_c}{\rho_s} \right)^3 \quad (2.19a)$$

$$\frac{\tau_{32}}{E_s} = 2.6 \left( \frac{\rho_c}{\rho_s} \right)^3 \quad (2.19b)$$

and for the shear moduli  $G_{31}$  and  $G_{32}$  as

$$\frac{G_{31}}{G_s} = 0.375 \left( \frac{\rho_c}{\rho_s} \right) \quad (2.20a)$$

$$\frac{G_{32}}{G_s} = 0.6 \left( \frac{\rho_c}{\rho_s} \right) \quad (2.20b)$$

The core shear modulus  $G_{cxz}$  used in equation (2.6) to calculate the skin stress should be taken as either  $G_{31}$  or  $G_{32}$  depending on the orientation of the ribbon direction in the honeycomb. This anisotropy leads to a dependence of skin failure loads on the honeycomb orientation. Similarly the core shear strength  $\tau_{cs}$  depends on the honeycomb orientation.

## Experimental Evaluation of Honeycomb Mechanics

The theoretical relations detailed in section 2.2.3 are those that we use for our calculations in section 2.3. In this section we compare the theoretical expressions with experimental data from reference [27] and manufacturers'<sup>3</sup> data sheets [53] for honeycombs made of Nomex (aramid paper impregnated in phenolic resin). Often it is observed that there is a wide variation amongst data from different sources reflecting the wide manufacturing tolerances in the constituent aramid sheet (particularly  $\rho_s$ ) and the difficulties in making accurate measurements.

---

<sup>3</sup>Hexcel Composites formerly Ciba Composites

The measurements of out-of-plane compressive properties are made by testing honeycombs under stabilised<sup>4</sup> compression. As depicted in Fig. 2.4(a) the prediction of Equation (2.17) for Young's modulus lie between the two sets of data and close to that of reference [27]. Fig. 2.4(b) shows that Wierzbicki's [66] equation (2.18) for compressive strength fits the experimental data better than the usual mixture's law, reflecting the plastic collapse mechanism of Nomex under compression.

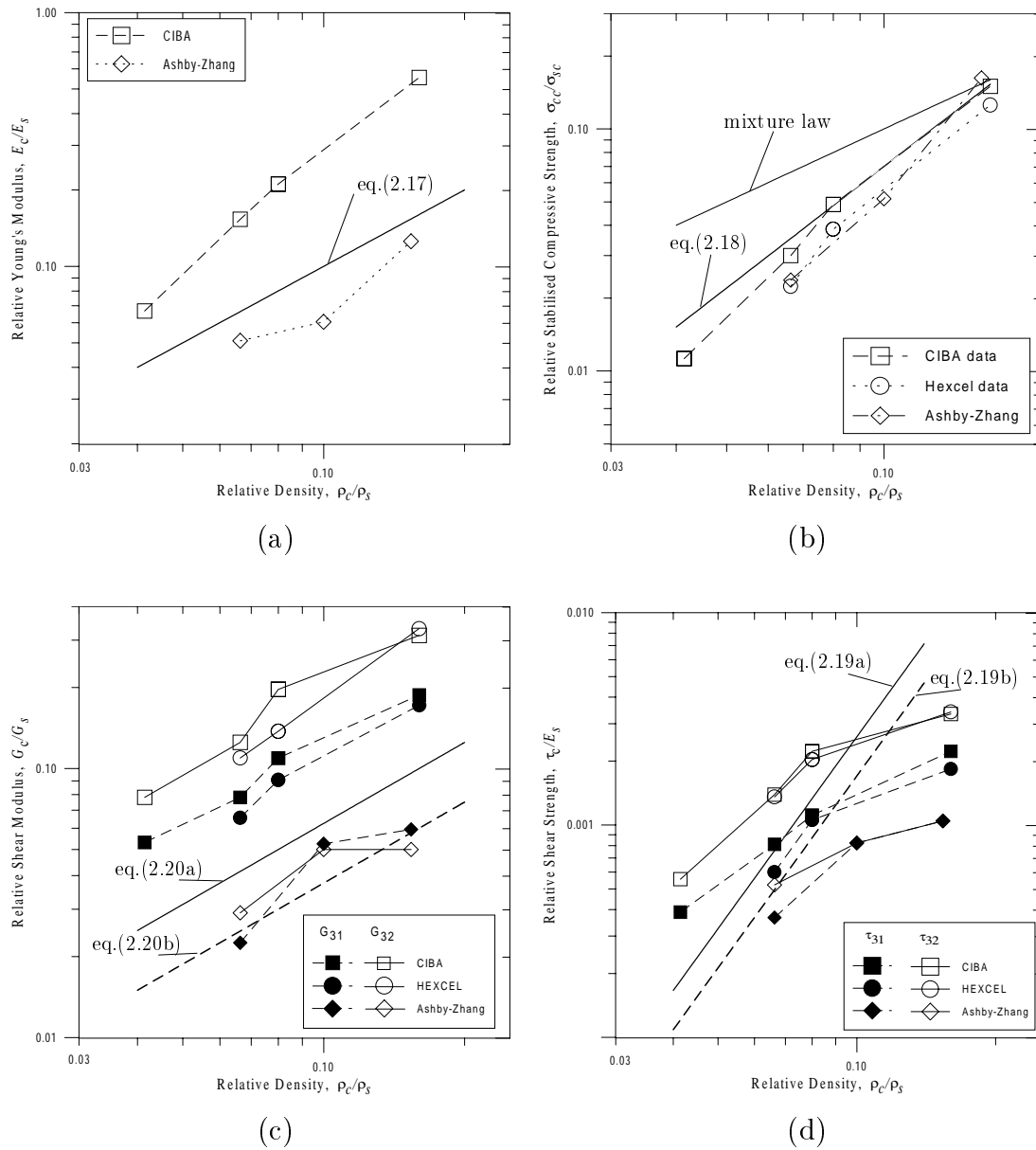
Figures 2.4(c,d) show plots of shear modulus and strength. Manufacturers' measurements are significantly higher than the measurements of Ashby and Zhang because of the different test setup. Ciba or Hexcel use a short beam test, where shear strength and stiffness are out-of-plane and measured indirectly (see eq. (2) in ref.[67]). Zhang and Ashby has tested the honeycombs in in-plane shear with an appropriate testing rig. We believe that the latter source gives a more direct estimate of shear properties. The major difference between equations (2.19a), (2.19b) and the experimental data of [27] for  $\rho_c/\rho_s > 0.1$  are due to debonding of honeycomb specimens from the rig. We can use equations (2.19a), (2.19b) when  $\rho_c/\rho_s > 0.1$ , since in the material systems considered here no debonding occurs.

## 2.3 Construction of a Failure Mode Map

Sections 2.2.1 and 2.2.2 have described various mechanisms of failure which occur with honeycomb sandwich panels, and the honeycomb mechanics needed to evaluate the failure loads for each of these mechanisms. In this section we describe how a map can be constructed detailing which failure mechanism actually occurs for a given material combination and beam geometry. This follows the work of Triantafillou and Ashby [41] for foam-core sandwich panels. The failure mode map is illustrated by way of examples in section 2.3.1. The failure loads depend on the properties of the skin and honeycomb solid material, the relative density  $\rho_c/\rho_s$  of the core, the thicknesses  $t$  and  $c$  of the skin and the core, and the beam span  $L$ . Because we include indentation failure, failure also depends on the loading details. In the experiments we use rollers to apply the load, so that failure depends on the roller radius  $R$ . The failure line load  $W_o$  can then be expressed as a function of the material properties and the beam parameters [41]  $W_o = f(t/L, t/R, \rho_c/\rho_s)$ . To evaluate this function the expressions for skin and core stresses [equations (2.7), (2.13), (2.15)] are substituted into the various failure criteria [equations (2.9), (2.10), (2.12) and (2.14), (2.16)] as described in section 2.2 to give the critical line loads as summarised in Table 2.1. The actual failure load and mode are

---


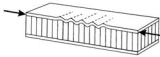

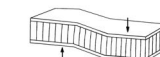

<sup>4</sup>Stabilised compression means restriction of the cell walls from slipping between the specimen and the rig plates during the test



**Figure 2.4:** Comparison of theoretical and experimentally measured out-of-plane (a) compressive modulus, (b) compressive strength, (c) shear modulus and (d) shear strength of Nomex honeycombs

given by the mode with the minimum failure load. Maps of the failure mode and failure load can then be drawn as a function of the beam geometry, for a given material system. The Matlab [68] programming language is used to evaluate the equations.

**Table 2.1:** Summary of failure criteria

Top skin yield		$W_o = 4\sigma_{fY} \frac{t}{L} \xi$
Intracell buckling		$W_o = \frac{8}{1-\nu_f^2} \left(\frac{t}{\alpha}\right)^2 E_f \frac{t}{L} \xi$
Face wrinkling		$W_o = 4B_1 E_f^{1/3} E_s^{2/3} \left(\frac{t}{L}\right) \left(\frac{\rho_c}{\rho_s}\right)^{2/3} \xi$
Core Shear		$W_o = 2AE_s d \left(\frac{\rho_c}{\rho_s}\right)^3$
Indentation		$W_o = 3.25\sigma_{sc} \left(\frac{\rho_c}{\rho_s}\right)^{5/3} \delta$

Note: The quantities  $\xi$  and  $A$  change according to the honeycomb ribbon orientation

### 2.3.1 A Failure Mode Map for Beams with a GFRP Skin and Nomex Core

The above section describes how a failure mode map can be constructed for a honeycomb sandwich panel. This is illustrated in this section using sandwich panels made of GFRP laminate skins and Nomex honeycomb cores of different densities. The core and skin thicknesses  $c$  and  $t$  are 9.4 mm and 0.38 mm respectively and the nominal honeycomb cell size is 3 mm. Experimental results for this sandwich panel type are presented in section 2.4. Further details of the panel construction, materials and material properties are given in that section. Fig. 2.5(b) shows the dependence of line load  $W_o$  at failure on core relative density  $\rho_c/\rho_s$  and face thickness to span  $t/L$  ratio, for a value of the radius of the roller to the skin thickness  $R/t$  of 26. Each surface corresponds to a different failure mode. The failure mode map, Fig. 2.5(a) is given by the projection of the intersections between failure surfaces on the  $\rho_c/\rho_s - t/L$  plane. Slightly different failure maps are calculated depending on whether the honeycomb ribbon lies in the longitudinal direction along the beam axis, or transverse to the beam axis. Differences arise from the anisotropy in the strength and stiffness of honeycomb in shear [c.f. equations (2.8) and (2.19a,b)]. As noted in section 2.2.2, failure by indentation is estimated using an empirical approach and relies on experimental measurements of the contact area as described in section 2.4. Indentation is the only mechanism which depends on

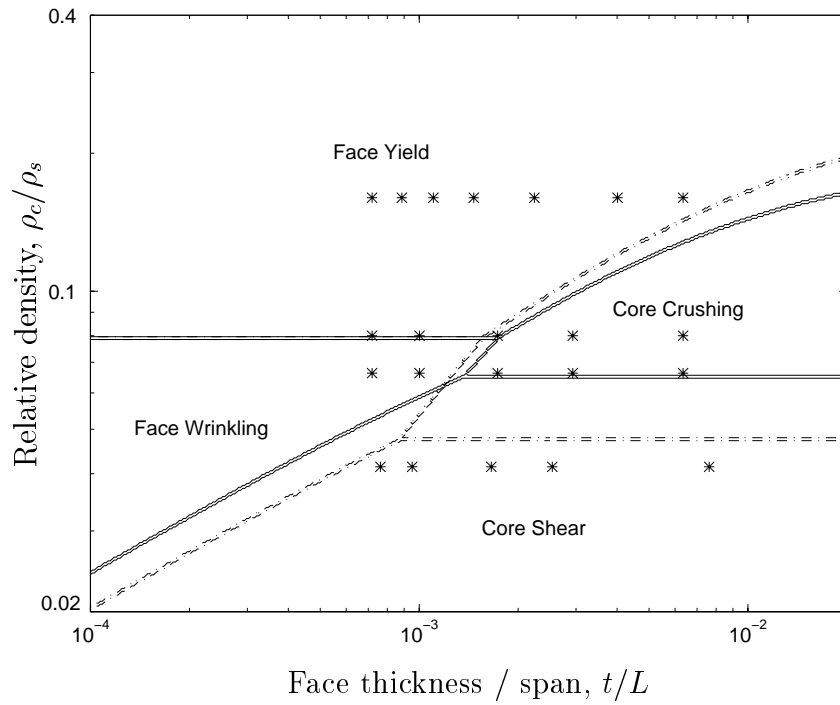
the roller diameter. This will be a more widespread mechanism of failure with smaller roller diameters. For the honeycomb geometry chosen for these plots, intra-cell dimpling is not predicted. At the map boundaries, the failure loads for the mechanisms either side of the boundary are equal. In practice failure near a boundary may be due to a combination of the two mechanisms and coupling between the two mechanisms may reduce the load below that predicted for each of the modes independently.

The failure mode map shown in Fig. 2.5(a) is useful where a designer has specified face and core thicknesses and wishes, for example, to select an appropriate span or relative density. More commonly, however, the span is fixed, a standard skin construction and thickness is specified, and only the core thickness or density can be relatively easily changed. In this case it is more useful to plot a map of the failure modes and loads as a function of core relative density and core thickness to span ratio  $c/L$ , at a fixed skin thickness to span ratio  $t/L$  and roller radius to face thickness ratio  $R/t$ . Figure 2.6 shows such maps for three typical values of  $t/L$  with  $R/t = 26$ . Note that for long spans (Fig. 2.6a) the core crushing failure mode vanishes, while for short spans face wrinkling is not predicted (Fig. 2.6c).

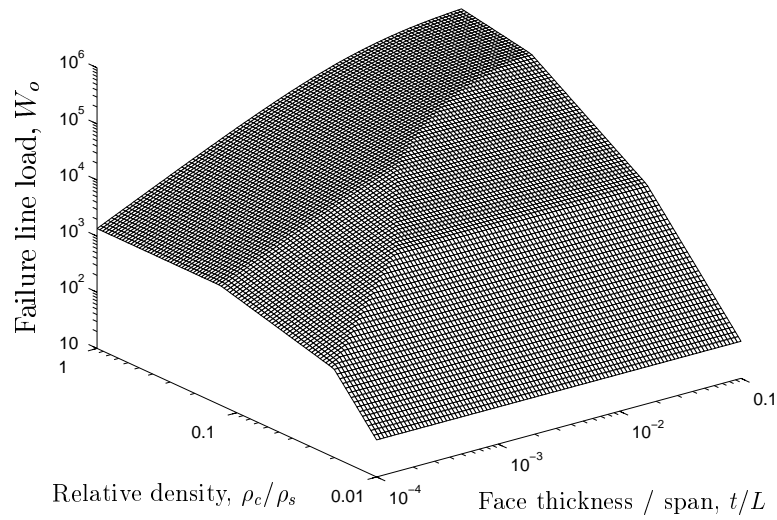
## 2.4 Experiments

Sandwich panels were made of Nomex honeycomb core and GFRP laminate skins and were supplied by Hexcel Composites. All panels had the same skin cross-ply laminate on either side of the core, as depicted in Fig. 2.7. Each laminate comprised two glass preregs; the outer with a resin content of 27% and the inner with 41%, giving a skin thickness  $t$  of 0.38 mm. The Nomex honeycomb cores used in the panels are designated by the manufacturer as Aeroweb® type A1. Panels with core densities of 29, 48, 64 and 128 kg/m<sup>3</sup> were used. For most of the tests the honeycomb had a nominal cell size of 3 mm, but for tests described in section 2.5.4 a cell size of 13 mm was used. The core thickness  $c$  was 9.4 mm. Mechanical properties of the skin and the honeycomb's constituent solid material (aramid paper + resin) are listed in Table 2.2. Since the compressive strength of the laminate has been inferred from bending tests of sandwich beams, this is not an independent measurement. Hexcel quote a value of 265 MPa, based on simple beam theory [equation (2.4)] for long beams. Using the beam model [equation (2.7)] with a correction for shear in the core, a revised estimate for the compressive strength of the laminate of 300 MPa is inferred from the data at long spans.

Panels were cut into beams using a diamond wheel. A width  $b$  of 40mm was chosen



(a)



(b)

**Figure 2.5:** (a) Failure mode map. Solid lines refer to beams in which the honeycomb ribbon lies along the beam axis; dashed lines for when the ribbon lies transverse to the beam axis. The \* symbol identifies experimental measurements described in section 2.4, (b) Failure load surface for ribbon lying along the beam axis

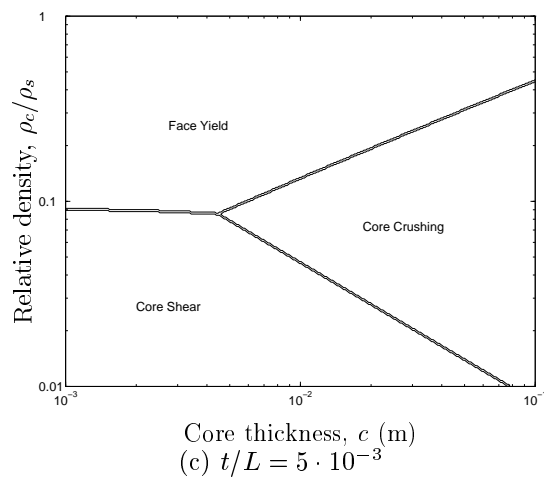
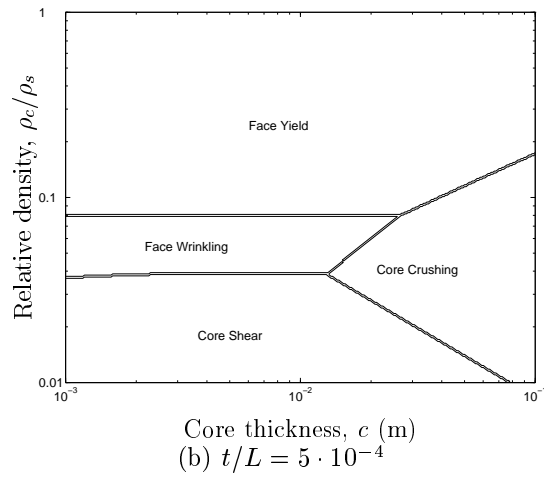
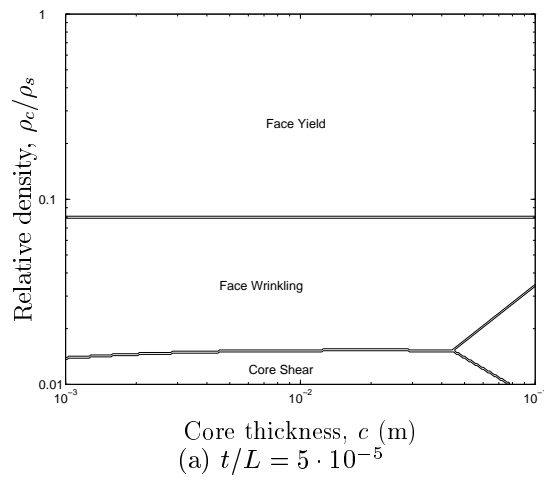


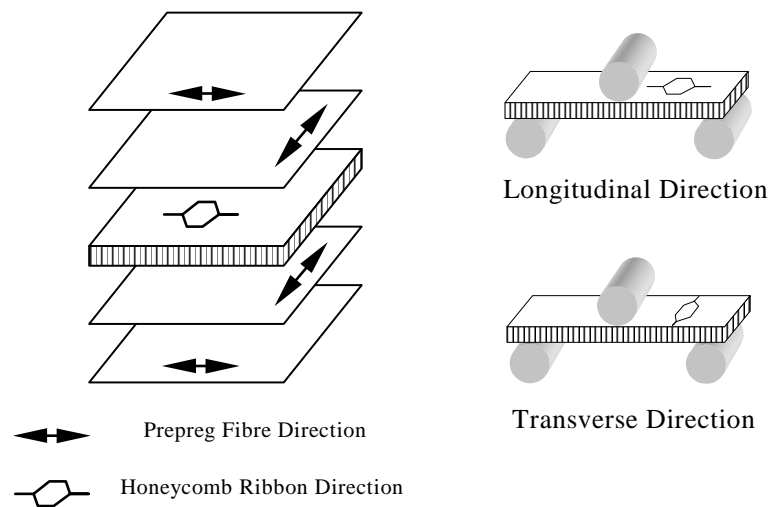
Figure 2.6: Failure mode map for three typical values of  $t/L$  and  $R/t = 26$



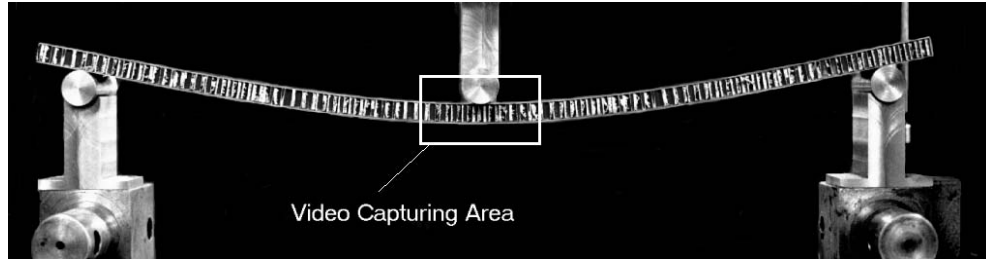
	Nomex [26]	Laminate skin [69]
Young's modulus, (GN/m <sup>2</sup> )	$E_s = 0.9$	$E_f = 20.5$
Shear modulus, (GN/m <sup>2</sup> )	$G_s = 0.32$	$G_f = 4.2$
Compressive strength, (MN/m <sup>2</sup> )	$\sigma_{sc} = 80$	$\sigma_{fY} = 300$
Poisson's ratio	$\nu_s = 0.4$	$\nu_f = 0.17$
Density, (Mg/m <sup>3</sup> )	$\rho_s = 0.724$	–

**Table 2.2:** Material properties of Nomex and laminate skin

so that it was greater than twice the sandwich height and three times the cell size, as recommended in by ASTM standards [70]. Beams were cut with the ribbon direction either in the longitudinal direction along the beam axis or in the transverse direction, as depicted in Fig. 2.7. Beams of varying spans and core relative densities were made to probe the various regions of the failure mode maps (Fig. 2.5). Specimens were tested in 3-point bending, applying the load through rollers of diameter of 20 mm (c.f. ASTM standard C393-62 [70]). The crosshead speed was kept constant through the test and was chosen so that the maximum load occurred between 3 and 6 min after the start of the test. Displacement of the central loading point relative to the end rollers was monitored using an LVDT and logged on a computer. The central section of the beam (where failure invariably occurred) was also recorded on a video recorder (Fig. 2.8) as the test progressed. To model failure due to local indentation (section 2.2.2), it is necessary to define the value the length of the contact area  $\delta$  between the central roller and the top skin. This was estimated experimentally by putting carbon paper between the roller and the specimen. For all the specimens tested  $\delta$  was between 2 and 3 mm,

**Figure 2.7:** Layup details

with a typical value of 2.5 mm. This information was used to estimate the failure load due to indentation as described in section 2.2.2.



**Figure 2.8:** Test setup

### 2.4.1 Experimental Results

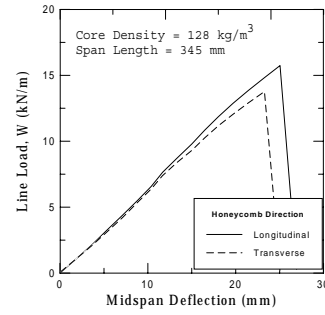
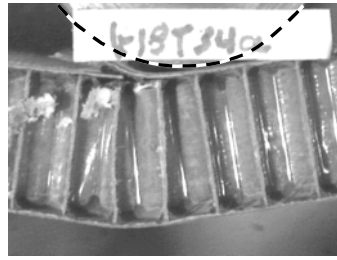
Figures 2.9(a-d) show photographs of the section under the central load just after failure, illustrating four failure modes observed during the tests of those beams with 3 mm honeycomb cell size. These were taken from videos recorded during the tests. Beam details for each of these figures are given in Table 2.3; to scale the photographs note that the cell size is 3 mm for all the specimens of Fig. 2.9, except Fig. 2.11(a,b) which has the larger cell width of 13 mm. For clarity the roller seen in the top half of the figures has been outlined in Fig. 2.9(a). Corresponding load–deflection curves are included in Fig. 2.9. With all the failure mechanisms except intracell buckling (Fig. 2.11a,b) and core shear (Fig. 2.9d), failure occurred in a brittle manner with little non-linearity in the load displacement curves before failure and a sharp drop in load at failure. For short span tests where indentation occurred (Fig. 2.9c), the beam has a significant post-failure strength as the core progressively crushes. Table 2.3 presents the average<sup>5</sup> line loads  $W_o$  at failure and corresponding observed failure mechanisms. The mode is described as ‘Complex’ when failure appeared to occur simultaneously in the core and in the face. Those mechanisms denoted as ‘mode 1  $\leadsto$  mode 2’ (i.e. Intracell dimpling  $\leadsto$  core crushing) indicates the appearance of mode 1, as elastic instability before the final failure mode 2.

The measured effect of skin thickness to span ratio on the failure load is compared with theory in Figs. 2.10(a)-(d) for the different core densities. The theoretical graphs are sections through the load surface, Fig. 2.5(b), at constant core relative density. Experimental mechanisms of failure are indicated on these graphs to allow a comparison between the actual and predicted failure mechanisms.

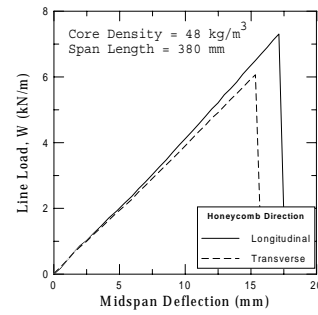
<sup>5</sup>Most of tests were repeated and the difference between failure loads was less than 10%

Core Density (kg/m <sup>3</sup> )	Honeycomb ribbon direction	Span length (mm)	$t/L$	Measured line fail.load (kN/m)	Observed failure modes
29 (3mm cell)	Long.	500	7.6E-04	3.8	Face wrinkling
		400	9.5E-04	4.2	Face wrinkling
		230	1.7E-03	5.1	Core shear→face wrinkl.
		150	2.5E-03	5.6	Core shear→crushing
		50	7.6E-03	6.4	Core shear→crushing
	Trans.	500	7.6E-04	3.0	Face wrinkling
		400	9.5E-04	3.4	Face wrinkling
		230	1.7E-03	4.1	Core shear→face wrinkl.
		150	2.5E-03	4.8	Core shear→crushing
		50	7.6E-03	6.0	<i>Core shear→crushing</i>
48 (3mm cell)	Long.	530	7.2E-04	6.2	Face wrinkling
		380	1.0E-03	7.5	Face wrinkling
		220	1.7E-03	9.3	Complex
		130	2.9E-03	11.0	Core crushing
		60	6.4E-03	11.9	Core crushing
	Trans.	530	7.2E-04	5.3	Face wrinkling
		380	1.0E-03	6.1	<i>Face wrinkling</i>
		220	1.7E-03	7.8	Complex
		130	2.9E-03	9.2	Core crushing
		60	6.4E-03	10.8	Core crushing
64 (3mm cell)	Long.	530	7.2E-04	8.2	Face yield
		380	1.0E-03	10.2	Face yield+wrinkling
		220	1.7E-03	13.8	Complex
		130	2.9E-03	15.6	Core crushing
		60	6.4E-03	17.2	Core crushing
	Trans.	530	7.2E-04	6.6	Face yield
		380	1.0E-03	8.0	Face yield+wrinkling
		220	1.7E-03	10.4	Complex
		130	2.9E-03	12.3	Core crushing
		60	6.4E-03	14.5	Core crushing
128 (3mm cell)	Long.	530	7.2E-04	11.6	Face yield
		430	8.9E-04	13.2	Face yield
		345	1.1E-03	17.0	Face yield
		260	1.5E-03	23.2	Face yield
		170	2.2E-03	31.3	Face yield
		95	4.0E-03	42.1	Complex
		60	6.4E-03	47.5	Core crushing
	Trans.	490	7.8E-04	9.4	Face yield
		430	8.9E-04	10.9	Face yield
		345	1.1E-03	14.7	<i>Face yield</i>
		260	1.5E-03	17.9	Face yield
		170	2.2E-03	26.5	Face yield
		95	4.0E-03	38.1	Complex
		60	6.4E-03	44.4	<i>Core crushing</i>
64 (13mm cell)	Long.	500	7.6E-04	4.0	Intracell dimpl.→face peel.
		230	1.7E-03	8.9	<i>Intracell dimpl.→face peel.</i>
		150	2.5E-03	11.2	Intracell dimpl.→core crush.
		50	7.6E-03	21.1	Intracell dimpl.→core crush.
	Trans.	500	7.6E-04	4.2	Intracell dimpl.→face peel.
		230	1.7E-03	9.1	Intracell dimpl.→face peel.
		150	2.5E-03	11.3	Intracell dimpl.→core crush.
		50	7.6E-03	20.8	Intracell dimpl.→core crush.

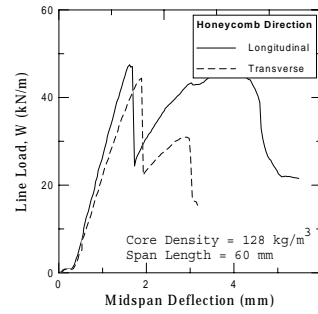
**Table 2.3:** Experimental results. Photographs of failure given in Fig. 2.9 and 2.11 correspond to the entries in italics in the final column of this table



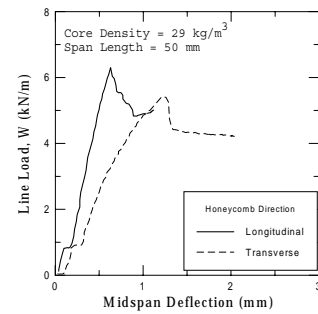
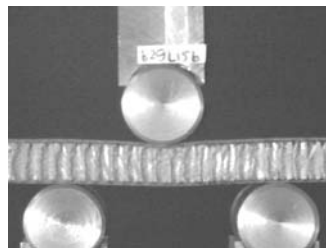
(a) Face yield ( $\rho_c = 128 \text{ kg/m}^3$ ,  $L = 340 \text{ mm}$ )



(b) Face wrinkling ( $\rho_c = 48 \text{ kg/m}^3$ ,  $L = 380 \text{ mm}$ )



(c) Core crushing ( $\rho_c = 128 \text{ kg/m}^3$ ,  $L = 60 \text{ mm}$ )



(d) Core crushing ( $\rho_c = 128 \text{ kg/m}^3$ ,  $L = 340 \text{ mm}$ )

**Figure 2.9:** Photographs of the different failure modes (for transverse ribbon direction) and corresponding load deflection curves (for both ribbon directions)

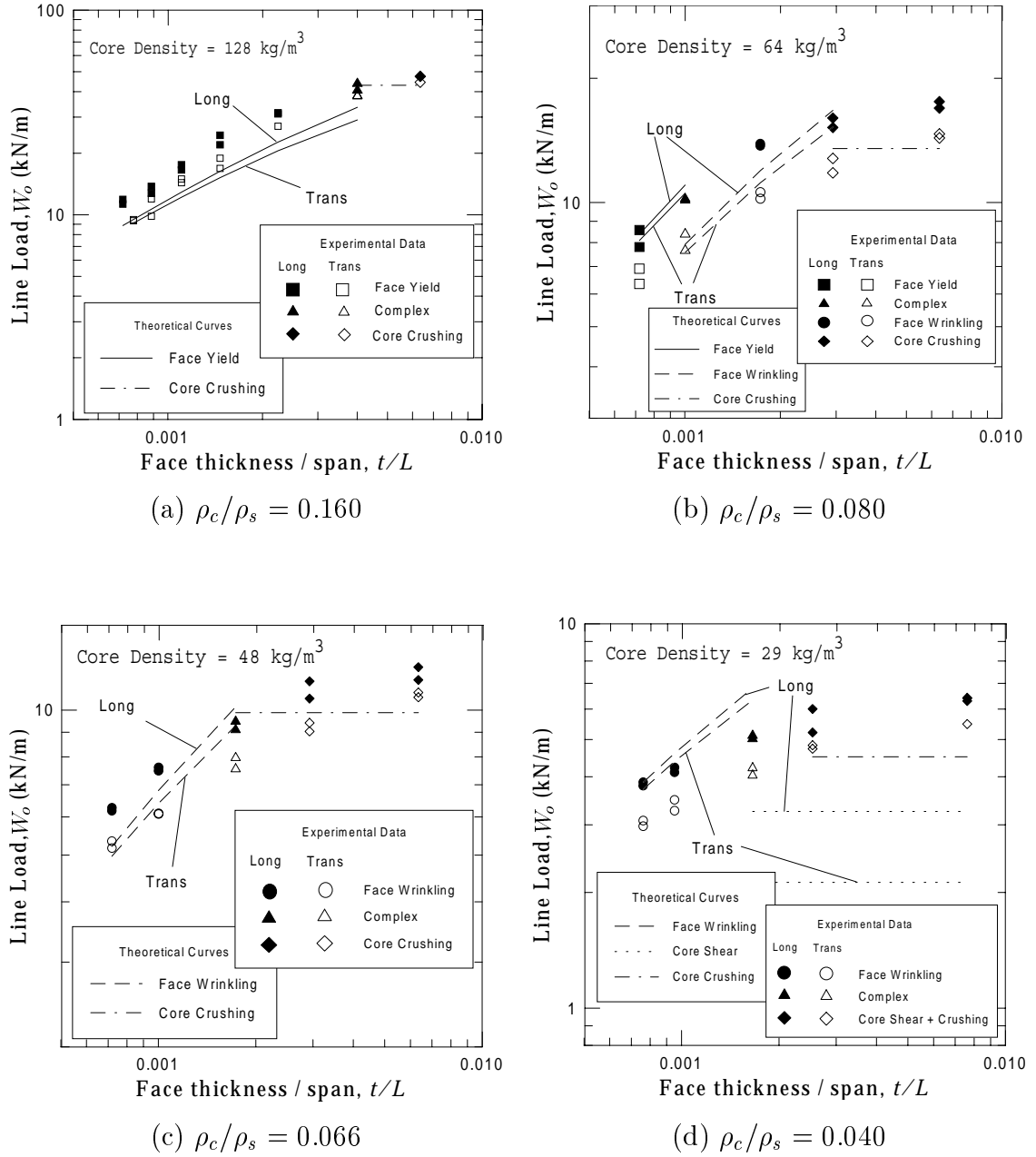


Figure 2.10: Variation of failure load  $W_o$  with skin thickness to span ratio  $t/L$

## **2.5 Discussion**

Figure 2.10 shows that, in general, the experimental failure loads agree satisfactorily with theoretical values and that the observed failure modes are generally the same as the predicted modes (Fig. 2.5). Where a transition from one failure mode to another occurs, the mechanism of failure is mixed, but the failure load is still adequately predicted. The main source of deviations arises from the errors in predicting the honeycomb material properties (section 2.2.3).

### **2.5.1 Skin Failure**

The laminate face yielding strength has been chosen to fit data at long spans, as discussed in section 2.4. At the longest spans with the 64 kg/m<sup>3</sup> honeycomb, face yield occurs although wrinkling is predicted, but as shown in Fig. 2.5(a), these points are very close to the boundary between these two mechanisms.

### **2.5.2 Core Failure**

Failure load predictions for core crushing are adequate for the higher density cores but predictions are poor for the lower density cores. The photograph in Figure 2.9(d) illustrates a beam with a low density core in transverse direction near the failure load, where core shear failure is predicted. Final failure is a mixture of core shear and crushing under the indenter. The difference in the initial slopes of the load–deflection curves<sup>6</sup> for the specimens with different ribbon directions reflects the anisotropy associated with the core shear stiffness. Non-linearity in the curve for the transverse direction indicates that there may be some ductile shear of the core prior to final failure. The significant under-prediction of the failure load [Fig. 2.10(d)] due to core shear is because final failure does not occur when the core fails in shear. Predictions of failure based on the core crushing strength would give a relatively good agreement with measurements in this case. Again this highlights the need for more elaborate models of core failure near loading points.

### **2.5.3 Effect of Ribbon Direction**

Specimens with ribbon running in the longitudinal direction fail at a significantly higher load than those with ribbon in the transverse direction in all cases except where failure

---

<sup>6</sup>The kinks in the load deflection curves at a low load are an artefact of the measuring system.

is by intracell dimpling (section 2.5.4). For face failure modes, a slight difference is predicted, associated with the effect of core shear stiffness on the stress in the skins, although the measured differences are somewhat greater than the prediction. The theoretical model described for core crushing does not include any anisotropic material properties. The substantial difference between the strengths for the two ribbon orientations suggest that an improved model is necessary, looking in more detail at the stresses around an indenter and including the effect of core shear.

### **2.5.4 Intra-cell Buckling**

Section 2.2.1 defines a critical honeycomb cell size above which failure occurs by intra-cell buckling instead of by top face yielding. For the materials used here, this transition is predicted at a cell size of approximately 9 mm. This hypothesis was tested by using specimens with a cell size 13 mm, a core density of  $64 \text{ kg/m}^3$  and a range of skin thickness to span ratios. All of the specimens with the larger cell size exhibited elastic intracell buckling. Final failure did not occur immediately, but at a higher load, either by delamination of the top-face or by core crushing for long or short spans respectively. Fig. 2.11(a) shows the section under the central roller at the onset of intra-cell buckling, while Fig. 2.11(b) shows the section when final failure occurs by delamination. Figure 2.11(c) compares the failure load and failure mechanisms for this set of tests. The theory [equation (2.10)] under-predicts the final failure load because it relates to the initial buckling instability and not the final delamination or core failure. Failure loads are independent of the honeycomb ribbon direction, because the single and double-walls paper walls make up a smaller proportion of the honeycomb for a given honeycomb density.

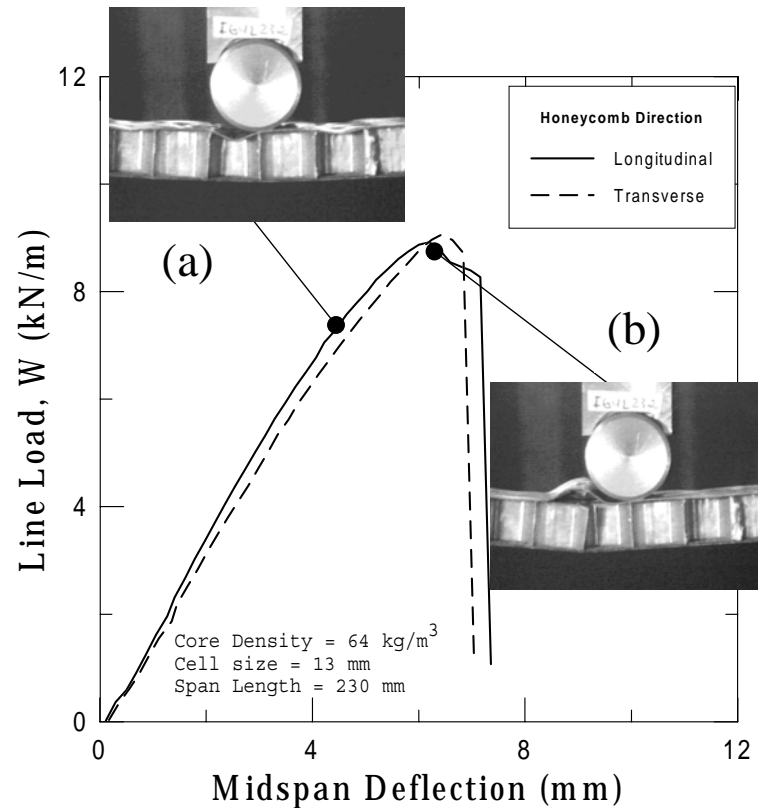
## **2.6 Conclusions**

Previous research on honeycomb mechanics and the behaviour of sandwich beams in 3-point bending have been combined to model the behaviour of honeycomb sandwich panels. It is assumed that the skin and core materials behave in a brittle manner. The failure mechanisms considered were face yield, face wrinkling, intra-cell buckling, core shear and indentation at the load points, leading to core crushing. The latter is treated in an empirical way, using measurements of the bearing area at the load points. The failure loads for each region are estimated assuming that there is no coupling between failure mechanisms. Following the work of Triantafillou and Gibson [41], failure mode maps are derived with axes as the core relative density and the ratio of the face thickness

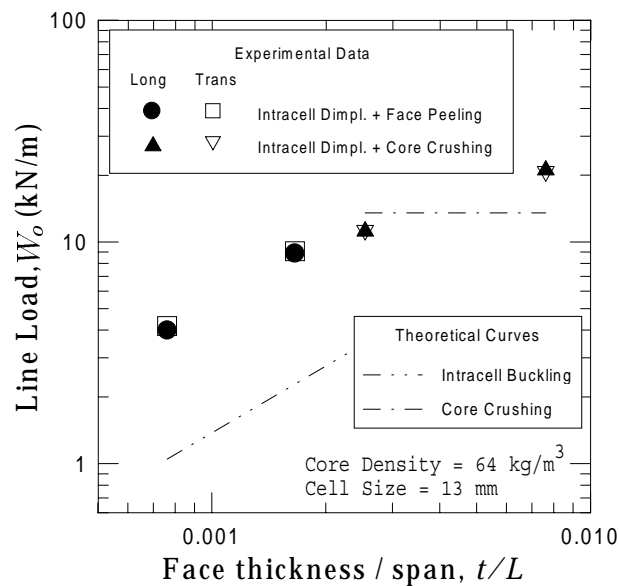
to span length. Each map is appropriate for a single value of the ratio of the radius of the roller to the skin thickness. Regions in which the various failure mechanisms occur are identified on the maps. Alternative axes for the map of core relative density and the core thickness are suggested, as a more useful set of parameters for a beam designer or manufacturer. Although the maps are generated for three-point bending, the method can straightforwardly be applied to other loading geometries, for example four-point bending. The method is illustrated using the widely used combination of cross-ply GFRP laminate skins with a Nomex/phenolic resin honeycomb core.

Experimental tests showed that, in general, the maps predicted adequately failure modes and failure loads. The transition from face yielding to intra-cell buckling for long span beams was demonstrated by increasing the honeycomb cell size from 3 to 13 mm. Failure near the load points due either to core shear or core indentation was not modelled well. To model this behaviour more sophisticated models of the contact region and of the failure criteria in the core are needed. Chapters 3 and 4 show how the implementation of the high-order sandwich beam theory of Frostig [46] provides a better insight into the mechanism of localised effects induced by concentrated loads and helps to produce an improved indentation failure analysis for honeycomb sandwich beams.





(a) Elastic intra-cell buckling (b) Final failure due to top skin delamination



(c) Experimental results compared with theory

**Figure 2.11:** Photographs and results of specimens with 13 mm cell size

# Chapter 3

## Indentation Resistance of Sandwich Beams

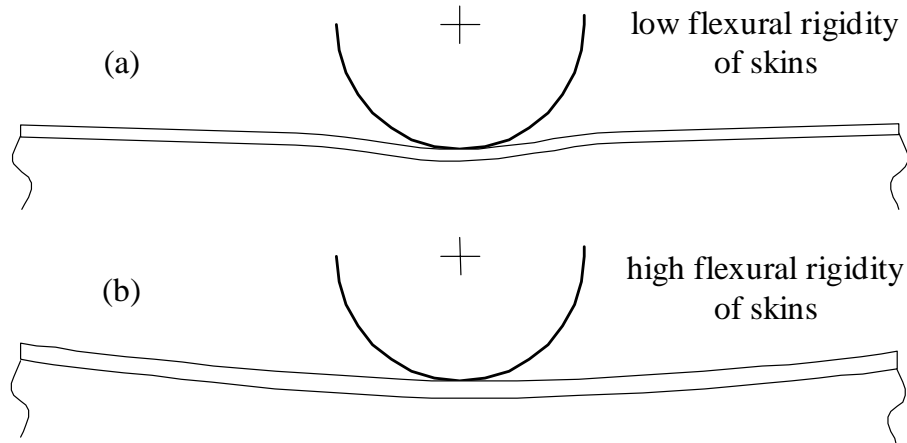
### 3.1 Introduction

The experiments described in the previous chapter revealed the important role of the flexural rigidity of the skins and the transverse shear stiffness of the core on the overall resistance of a sandwich beam to indentation. In the literature the importance of the core behaviour in affecting indentation failure has been considered; however, the influence of the skin's flexural rigidity is generally overlooked. This omission derives from the fact that in practical applications the skins are quite stiff and the influence of skin flexural rigidity can be neglected. One of the main aims of this chapter is to focus on the role of skin rigidity in indentation failure. Before introducing any analytical methods, it is instructive to consider two extreme cases, as illustrated in Fig. 3.1.

- For very flexible skins (Fig. 3.1a), there is large local deformation under the load which can easily lead to core failure.
- For very rigid skins (Fig. 3.1b), indentation failure will be relatively hard, as the skins spread the load.

Skin flexibility is a prerequisite for indentation failure and the core's transverse flexibility enhances this susceptibility. In this chapter the high-order sandwich beam theory (HOSBT) is used to analyse the bending behaviour of sandwich beams under localised loads and extract conclusions about their indentation resistance by examining the flexibility of the top skin to the external applied loads. The ability of HOSBT to cope with the localised effects that appear in sandwich beams at the load points is experimentally verified by Surface Displacement Analysis in section 3.3. Section 3.4 introduces a length scale that characterises the susceptibility of a sandwich beam to localised effects.

In section 3.5 high-order sandwich beam theory is used to predict the contact stress distribution between a cylindrical indenter and the top skin of a sandwich beam.



**Figure 3.1:** The behaviour of flexible and rigid skins

## 3.2 High-Order Sandwich Beam Theory

The mathematical formulation of high-order sandwich beam theory (HOSBT) is introduced by Frostig and Baruch [46]. ‘High-order’ refers to the non-linear way in which the in-plane and vertical displacements are allowed to vary through the height of the core. The core vertical displacement is assumed to have a quadratic variation with height  $z$ . Other core displacements also vary in a non-linear way, with the exact variation being expressed in terms of Fourier series. This contrasts with simple beam theory where the core in-plane displacements are assumed to vary in a linear way through the depth, and the out-of-plane displacements are assumed to be constant. These high-order variations allows modelling of the more complicated changes in core geometry which occur at loading points. Thus the basic assumptions of HOSBT are:

- The shear stresses in the core are uniform through the height of the core.
- The core vertical displacement variation is a quadratic polynomial in  $z$  [see equation (3.11)], allowing the core to distort and its height to change.
- The core is considered as a 3D elastic medium, which has out-of-plane<sup>1</sup> compressive and shear rigidity, whereas its resistance to in-plane<sup>2</sup> normal shear stresses is negligible.

<sup>1</sup>‘Out-of-plane’ refers to 3 direction as illustrated in Fig. 1.3 or the direction normal to the plane of the sandwich panel

<sup>2</sup>‘In-plane’ refers to 1-2 plane as illustrated in Fig. 1.3 or the plane of the sandwich panel

This high-order analysis is based on variational principles; the details of derivation of the governing equations and associated boundary conditions are presented in ref. [46]. In this study we examine the bending behaviour and the localised effects of sandwich beams formulating a two dimensional model of a sandwich beam with unit width and span  $L$ , which consists of a core with thickness  $c$ , Young's and shear modulus  $E_c$  and  $G_c$  respectively, and two skins with the same thickness  $t = t_t = t_b$ , Young's modulus  $E_f$  and Poisson's ratio  $\nu_f$ , as depicted in Fig. 3.2(b). An external distributed load  $q_t$  is applied on the top skin. The displacement and stress fields of the core are expressed in terms of the followings five unknowns: the in-plane deformations  $u_t$  and  $u_b$  in the  $x$ -direction of the centroid of the top and bottom skin respectively; their corresponding vertical displacements  $w_t$  and  $w_b$ ; and the shear stresses  $\tau_x$  in the core. The relevant geometric parameters and the notation of stresses and displacements appear in Fig. 3.2. The governing equations (see equations (37), (39) and (41)-(43) in ref [46]) are given below:

$$\left. \begin{aligned} A_t u_{t,,x} + \tau_x &= 0 \\ A_b u_{b,,x} - \tau_x &= 0 \\ D_t w_{t,,,,x} - \frac{E_c}{c}(w_b - w_t) - \frac{c+t}{2}\tau_{x,x} &= q_t \\ D_b w_{b,,,,x} + \frac{E_c}{c}(w_b - w_t) - \frac{c+t}{2}\tau_{x,x} &= 0 \\ u_t - u_b - \frac{c+t}{2}w_{t,x} - \frac{c+t}{2}w_{b,x} - \frac{c}{G_c}\tau_x - \frac{c^3}{12E_c}\tau_{x,,x} &= 0 \end{aligned} \right| \quad (3.1)$$

where  $A_t = A_b = E_f t / (1 - \nu_f^2)$  and  $D_t = D_b = E_f t^3 / [12(1 - \nu_f^2)]$  are the in-plane and flexural rigidity of the skins. The notation  $()_{,,,x}$  for example denotes the 4th partial derivative with respect to  $x$ . For a simply supported sandwich beam the solution can be expressed as a Fourier series expressing the variation of the relevant variables in the  $x$  direction as

$$u_t(x) = \sum_{m=1}^M C_m^{ut} \cos \frac{m\pi x}{L} \quad (3.2)$$

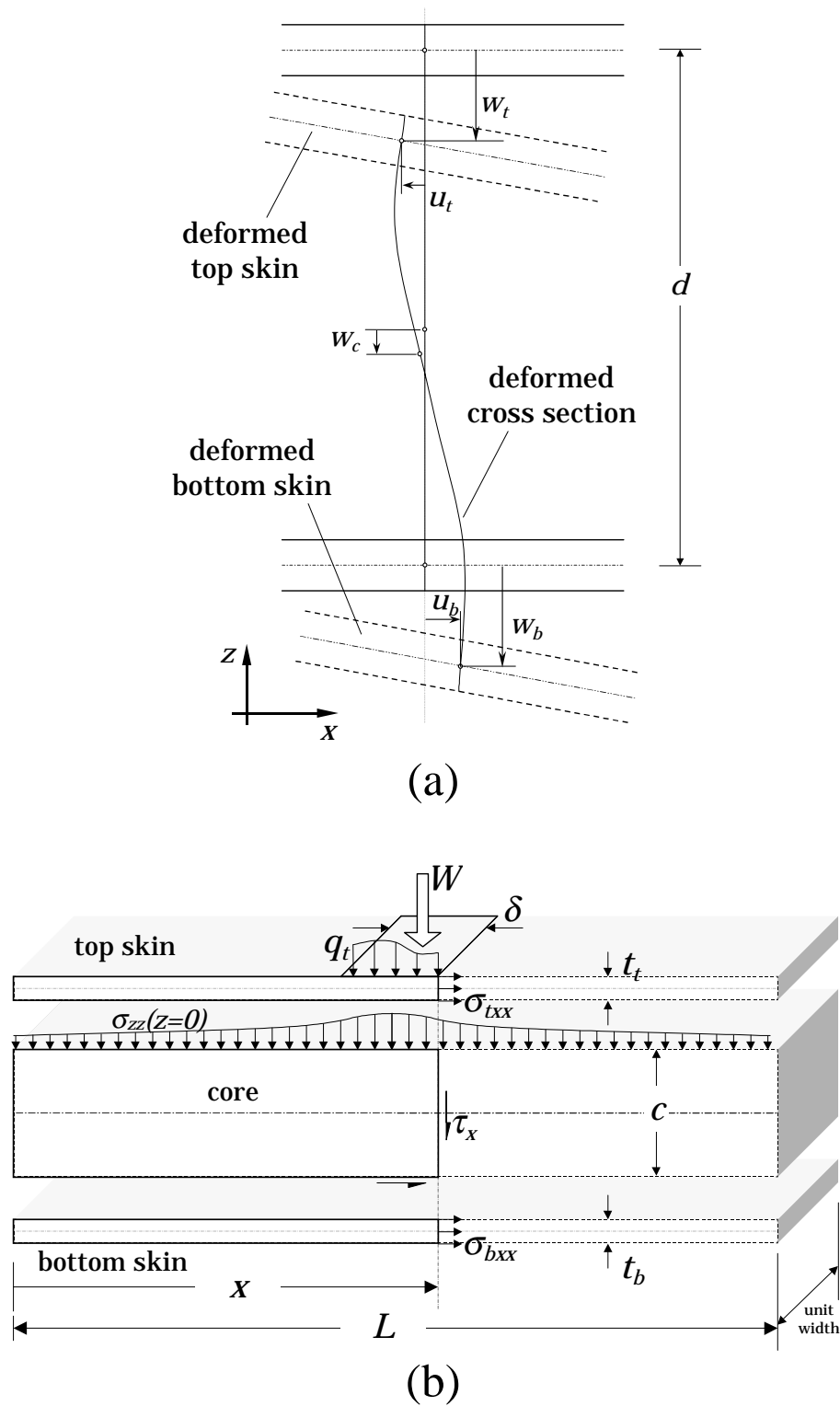
$$u_b(x) = \sum_{m=1}^M C_m^{ub} \cos \frac{m\pi x}{L} \quad (3.3)$$

$$w_t(x) = \sum_{m=1}^M C_m^{wt} \sin \frac{m\pi x}{L} \quad (3.4)$$

$$w_b(x) = \sum_{m=1}^M C_m^{wb} \sin \frac{m\pi x}{L} \quad (3.5)$$

$$\tau_x(x) = \sum_{m=1}^M C_m^{\tau_x} \cos \frac{m\pi x}{L} \quad (3.6)$$

where  $M$  = number of terms in the series; and  $C_m^{ut}, C_m^{ub}, C_m^{wt}, C_m^{wb}$  and  $C_m^{\tau_x}$  are constants to be determined. We assume that the external loads are exerted only on the top skin.



**Figure 3.2:** (a) Nonlinear displacement patterns, (b) Beam geometry and stresses. The origin of the  $z$ -coordinate is always taken at the top of the beam element, either skin or core, which is being considered

So in terms of the Fourier series we set

$$q_t(x) = \sum_{m=1}^M C_m^{qt} \sin \frac{m\pi x}{L} \quad (3.7)$$

where  $C_m^{qt}$  is a constant that depends on the distribution of the external load. After substituting every term of the Fourier series (3.2)-(3.6) in the governing equations (3.1), the problem can be expressed in matrix form as

$$[\mathcal{D}] \cdot [\mathcal{C}] = [\mathcal{Q}] \quad (3.8)$$

where

$$\mathcal{D} = \begin{bmatrix} -A_t(\frac{m\pi}{L})^2 & 0 & 0 & 0 & 1 \\ 0 & -A_b(\frac{m\pi}{L})^2 & 0 & 0 & -1 \\ 0 & 0 & -D_t(\frac{m\pi}{L})^4 + \frac{E_c}{c} & -\frac{E_c}{c} & \frac{c+t}{2} \frac{m\pi}{L} \\ 0 & 0 & -\frac{E_c}{c} & -D_b(\frac{m\pi}{L})^4 + \frac{E_c}{c} & \frac{c+t}{2} \frac{m\pi}{L} \\ 1 & -1 & -\frac{c+t}{2} \frac{m\pi}{L} & -\frac{c+t}{2} \frac{m\pi}{L} & \frac{c}{G_c} + \frac{c^3}{12E_c} (\frac{m\pi}{L})^2 \end{bmatrix}$$

$$\mathcal{C} = \begin{bmatrix} C_m^{ut} \\ C_m^{ub} \\ C_m^{wt} \\ C_m^{wb} \\ C_m^{\tau_x} \end{bmatrix} \quad \text{and} \quad \mathcal{Q} = \begin{bmatrix} 0 \\ 0 \\ C_m^{qt} \\ 0 \\ 0 \end{bmatrix}$$

By solving (3.8) with respect to matrix  $\mathcal{C}$  for every  $m = 1, 2 \dots M$  the Fourier coefficients in equations (3.2)-(3.6) can be determined. These equations can then be used to calculate all the in-plane and vertical displacements and core shear stresses. The in-plane normal stresses  $\sigma_{txx}$  in the top skin<sup>3</sup>, and the out-of-plane normal stresses  $\sigma_{zz}$  in the top skin-core interface are calculated indirectly as

$$\sigma_{txx} = E_f u_{t,x} \quad (3.9)$$

$$\sigma_{zz} = \frac{c}{2} \tau_{x,x} + \frac{E_c}{c} (w_b - w_t) \quad (3.10)$$

### 3.3 Surface Displacement Analysis

An experimental verification of high-order sandwich beam theory (HOSBT) has been undertaken by Thomsen and Frostig [71]. They conducted a series of photoelastic

---

<sup>3</sup>Only top skin compressive failure is considered

experiments, compared the results with analytical calculations and demonstrated a good agreement between the photoelastic measurements and the predictions based on the HOSBT. In this section a similar comparative study is conducted with respect to the displacement field in the core. The objective is to compare the analytical and experimental displacement distributions in sandwich beams with a ‘soft’ core as, for example the Nomex cores used in Chapter 2. Special emphasis is given to the local out-of-plane compression of the core under the localised loads, as this will be important in determining failure of the core.

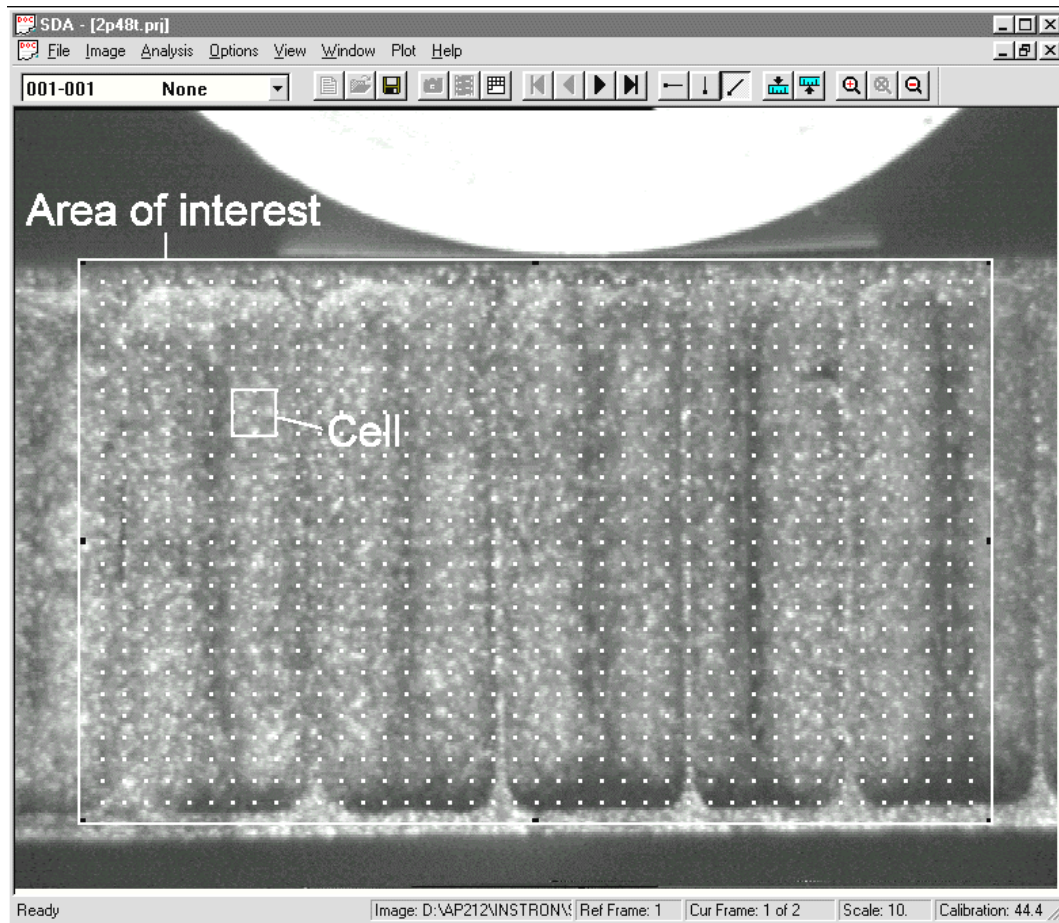
For the analytical predictions, the equations described in section 3.2 are implemented in a Matlab code to calculate the vertical displacement field within the core by the following equation (given in ref.[46])

$$w_c(x, z) = -\tau_{x,x} \frac{-z^2 + cz}{2E_c} + (w_b - w_t) \frac{z}{c} + w_t \quad (3.11)$$

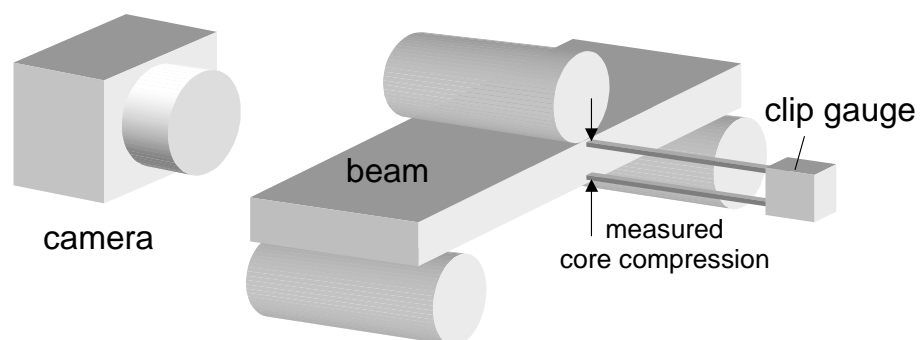
The experimental determination of vertical displacements in the core is achieved by Surface Displacement Analysis. SDA is a Windows based software developed by Instron Corporation, which detects and maps horizontal and vertical displacement of points on the surface of a specimen or structure. There are two main parts to the procedure; image capture and image analysis. SDA captures images of the surface of a material or structure using a video camera and a frame grabber board. The surface requires a random speckle pattern, either natural or applied, which has to be illuminated to ensure good contrast. Image frames of the surface of the specimen are captured at intervals while it deforms under load.

Then SDA compares and analyses pairs of these image frames using a designated area of interest, as depicted in Fig. 3.3. Each area of interest contains one or more analysis cells. During analysis, the pattern in each cell of the current frame is compared with the pattern in the corresponding cell of the reference frame. The software maps the deformation of the surface as a series of vectors displayed on the image, one vector for each cell. The software also calculates the strain for each cell. SDA contains a graphics module that plots displacement and strain. If the software is calibrated to the dimensions of the image, absolute displacement values can be obtained.

In this study we tested sandwich beams cut out from the panels described in section 2.4. Testing was under 3-point bending at a constant displacement rate of 0.5 mm/min. The beams’ width was 30mm, the span 60 mm and the rollers’ diameter 20 mm. The experimental setup is shown in Fig. 3.4. The clip gauge measures the midspan core compression during loading, while the video camera captures images of the other cross section of the beam. To apply a random speckle pattern of that cross



**Figure 3.3:** Surface Displacement Analysis software window, showing the reference image frame of a side cross section (painted to have a random speckle pattern) and the ‘area of interest’ where the analysis takes place



**Figure 3.4:** Experimental setup



section, at first it was painted black and then fine-sprayed with white paint to produce a pattern of random white dots on a black background (see the image in Fig. 3.3). The three dimensional surface of the cross section, arising from the honeycomb structure and the subsequent buckling of the cell walls, causes errors in the image processing and mapping of displacements using SDA. However in the initial stage of loading (with little buckling) the results are satisfactory and illustrative of the localised effects that occur under the central load.

For a sandwich beam with Nomex honeycomb core with density of  $48 \text{ kg/m}^3$  the load deflection curve is shown in Fig. 3.5. The same figure also shows the clip gauge measurements of midspan core compression against top skin deflection. For Surface Displacement Analysis two frames are chosen; the first reference frame, just before loading (point A in Fig. 3.5), and the second when the applied line load reaches the arbitrary value of  $6 \text{ kN/m}$ , labelled B in Fig. 3.5.

The SDA graphics module, after calibration, plots contours of equal vertical displacements within the core in mm, as depicted in Fig. 3.6(a). It should be noted that the camera was fixed relative to the central roller so that the specimen appears to move upwards with zero displacements at the roller. The SDA measurements demonstrate the occurrence of localised deflections under the applied load due to the core local compression. The contour of  $0.045 \text{ mm}$  close to the bottom skin indicates the total compression of the core in the midspan of the sandwich beam. This value agrees well with that measured by the clip gauge (see the dashed line in Fig. 3.5).

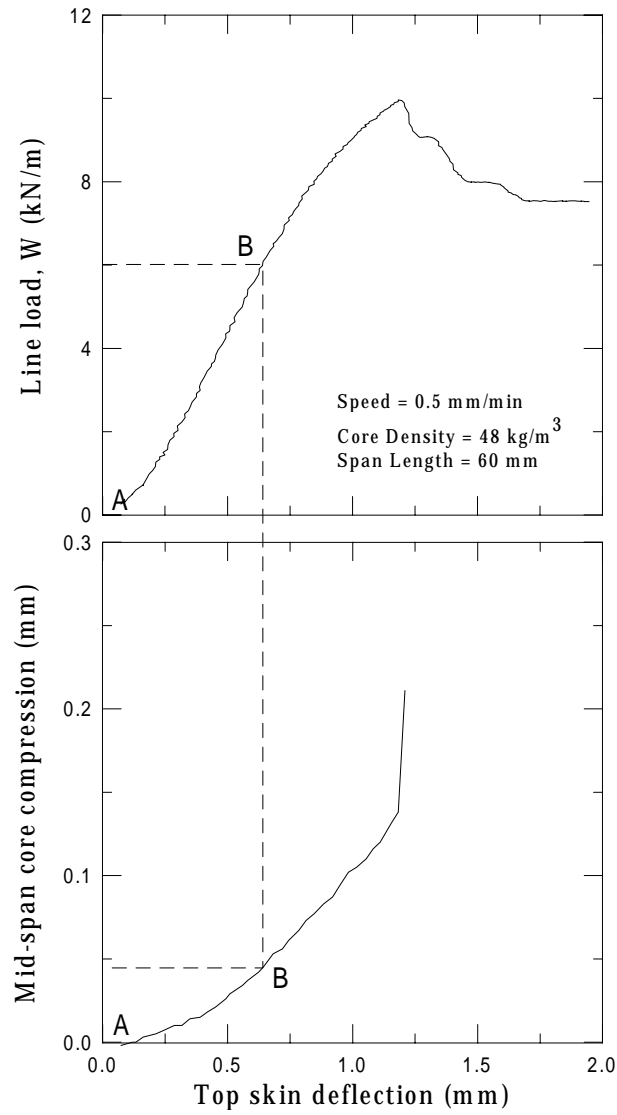
Fig. 3.6(b) shows a theoretical plot at the corresponding load of  $6 \text{ kN/m}$ , using equation (3.11). These calculations use the material properties of the skin and the honeycomb and the geometric attributes of the sandwich beam (Table 2.2). The total applied load is taken as  $6 \text{ kN/m}$  and applied uniformly over an area of  $2 \text{ mm long}^4$ . A comparison between the theory and experiments shown in Fig. 3.6 show that HOSBT provides an analytical tool that is capable of predicting the localised effects due to concentrated loads both qualitatively and quantitatively.

### 3.4 Effect of Spreading Stresses

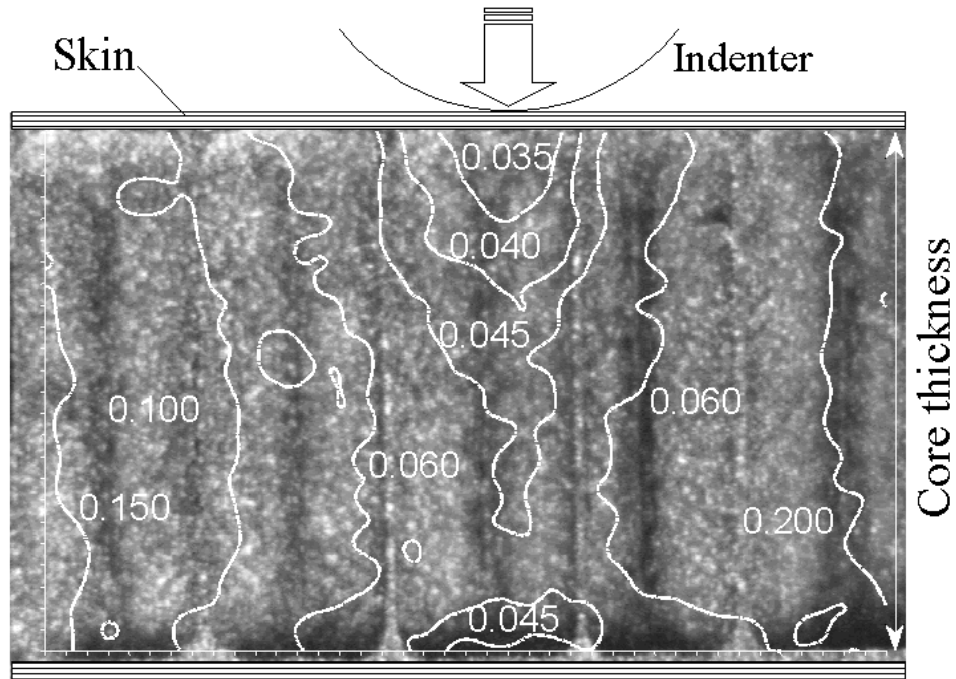
After demonstrating the applicability of high-order sandwich beam theory, in this section we use it to investigate the mechanism that controls the behaviour of a sandwich beam under localised loads. One of the key factors that governs the behaviour of a sandwich beam under localised loads is the shape of the normal stress distribution

---

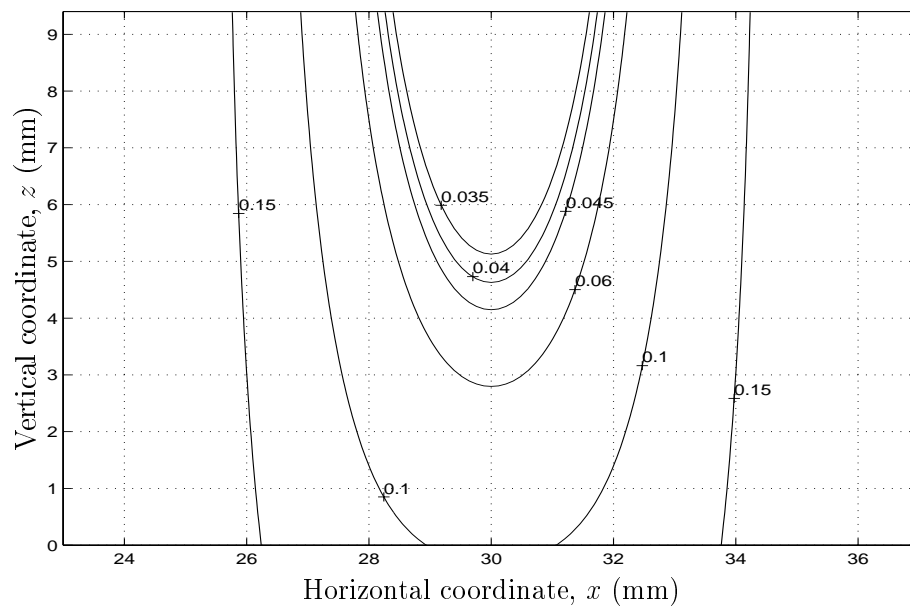
<sup>4</sup>The reason for this is explained in section 3.5



**Figure 3.5:** Load-deflection and core compression curves. A and B correspond to the frames used for processing by SDA. The dashed line indicates the total midspan core compression at a line load of 6 kN/m



(a)



(b)

**Figure 3.6:** Vertical displacement field in the core produced by (a) SDA and (b) HOSBT model. All contour values are in mm and the scaling in both plots is the same

along the beam in the top skin-core interface (see Fig. 3.2). Two extreme cases can be considered; a very rigid top skin that spreads the external stress in the interface, or a ‘membrane’ skin allows the applied stresses to pass intact through the interface into the core.

In this section we extract a dimensionless quantity which characterises the behaviour of a sandwich beam under 3-point bending, independently of the applied central load. We do this by defining an index which measures the ‘transparency’ of the top skin - i.e. to what extent the top skin-core interface ‘feels’ the stresses exerted on the external surface of the top skin. For this purpose we rewrite the matrices  $\mathcal{D}$  and  $\mathcal{Q}$  introduced in equation (3.8) as

$$\mathcal{Q} = \begin{bmatrix} 0 \\ 0 \\ C_m^{qt} \\ 0 \\ 0 \end{bmatrix} \text{ and } \mathcal{D} = \begin{bmatrix} \mathbf{A}_f & 0 & 0 & 0 & 1 \\ 0 & \mathbf{A}_f & 0 & 0 & -1 \\ 0 & 0 & \mathbf{D}_f & \mathbf{E}_c & \mathbf{C}_t \\ 0 & 0 & \mathbf{E}_c & \mathbf{D}_f & \mathbf{C}_t \\ 1 & -1 & -\mathbf{C}_t & -\mathbf{C}_t & \mathbf{G}_c \end{bmatrix} \text{ where } \begin{cases} \mathbf{A}_f = -A_t \left(\frac{m\pi}{L}\right)^2 \\ \mathbf{D}_f = -D_t \left(\frac{m\pi}{L}\right)^4 + \frac{E_c}{c} \\ \mathbf{E}_c = -\frac{E_c}{c} \\ \mathbf{C}_t = \frac{c+t}{2} \frac{m\pi}{L} \\ \mathbf{G}_c = \frac{c}{G_c} + \frac{c^3}{12E_c} \left(\frac{m\pi}{L}\right)^2 \end{cases}$$

Using the Symbolic Toolbox of Matlab equation (3.8) is solved with respect to the matrix  $\mathcal{C}$

$$[\mathcal{C}] = [\mathcal{Q}][\mathcal{D}]^{-1} \implies \begin{bmatrix} C_m^{ut} \\ C_m^{ub} \\ C_m^{wt} \\ C_m^{wb} \\ C_m^{\tau_x} \end{bmatrix} = C_m^{qt} \begin{bmatrix} -\frac{\mathbf{C}_t}{\mathbf{R}_1 + \mathbf{R}_2} \\ \frac{\mathbf{C}_t}{\mathbf{R}_1 + \mathbf{R}_2} \\ \frac{\mathbf{R}_1}{(\mathbf{D}_f - \mathbf{E}_c)(\mathbf{R}_1 + \mathbf{R}_2)} \\ -\frac{\mathbf{R}_2}{(\mathbf{D}_f - \mathbf{E}_c)(\mathbf{R}_1 + \mathbf{R}_2)} \\ \frac{\mathbf{A}_f \mathbf{C}_t}{\mathbf{R}_1 + \mathbf{R}_2} \end{bmatrix} \quad (3.12)$$

$$\text{where } \mathbf{R}_1 = \mathbf{D}_f(\mathbf{A}_f \mathbf{G}_c - 2) + \mathbf{A}_f(\mathbf{C}_t)^2 \text{ and } \mathbf{R}_2 = \mathbf{E}_c(\mathbf{A}_f \mathbf{G}_c - 2) + \mathbf{A}_f(\mathbf{C}_t)^2$$

Substituting equations (3.4)-(3.6) and the above Fourier coefficients into (3.10) the normal stresses in the top skin-core interface are given as

$$\begin{aligned} \sigma_{zz} &= \sum_{m=1}^M \left( -\frac{c}{2} \frac{m\pi}{L} C_m^{\tau_x} + \frac{E_c}{c} (C_m^{wb} - C_m^{wt}) \right) \sin \frac{m\pi x}{L} \\ &= \sum_{m=1}^M \left( -\frac{c}{2L} \frac{\mathbf{A}_f \mathbf{C}_t}{\mathbf{R}_1 + \mathbf{R}_2} + \frac{\mathbf{E}_c}{\mathbf{D}_f - \mathbf{E}_c} \right) C_m^{qt} \sin \frac{m\pi x}{L} \end{aligned} \quad (3.13)$$

Equation (3.13) shows that the Fourier coefficients for the stress  $\sigma_{zz}$  can be separated into two parts; one part containing the coefficient  $C_m^{qt}$  (units of stress), which depends on the distribution of the load, and a second part represented by the dimensionless ‘transmission coefficient’  $C_m^{\sigma_{zz}}$ , which is entirely dependent on the geometric attributes and material properties of the sandwich beam, where  $C_m^{\sigma_{zz}}$  is given by

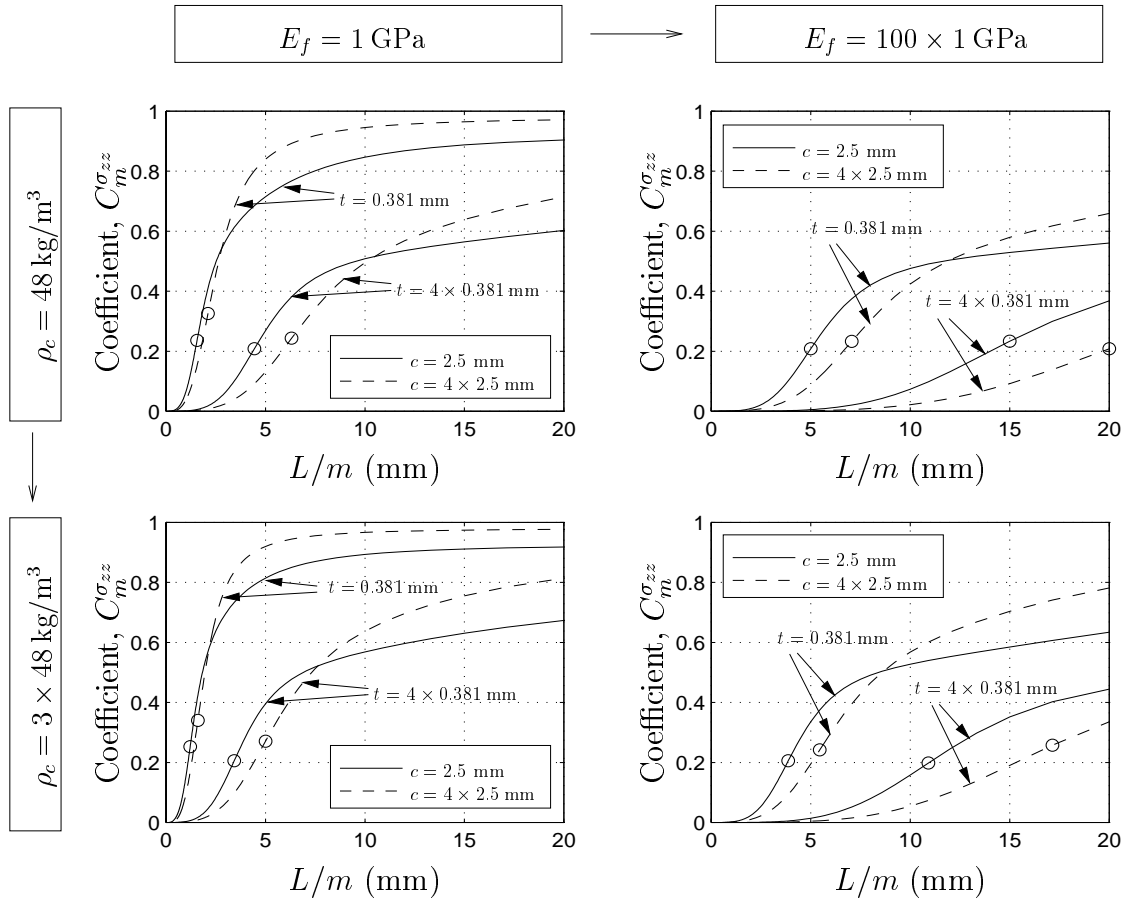
$$\begin{aligned} C_m^{\sigma_{zz}} &= -\frac{c}{2L} \frac{m\pi}{\mathbf{R}_1 + \mathbf{R}_2} \frac{\mathbf{A}_f \mathbf{C}_t}{\mathbf{D}_f - \mathbf{E}_c} + \frac{\mathbf{E}_c}{\mathbf{D}_f - \mathbf{E}_c} \\ &\approx -\frac{\mathbf{A}_f (\mathbf{C}_t)^2}{\mathbf{R}_1 + \mathbf{R}_2} + \frac{\mathbf{E}_c}{\mathbf{D}_f - \mathbf{E}_c} \quad \text{if } t \lll c \end{aligned} \quad (3.14)$$

For any geometry and material combination this transmission coefficient is a discrete function of the parameter  $L/m$ , which is the semi-wavelength of every term in the Fourier series. The value of  $C_m^{\sigma_{zz}}$  varies from 0 (small  $L/m$ ) to 1 (large  $L/m$ ). 0 implies no transmission of this Fourier component of applied stress while 1 implies total transmission through the top skin. Thus we conduct a parametric study, in which we calculate the variation of  $C_m^{\sigma_{zz}}$  with  $L/m$  for the range of material and geometric parameters given in Table 3.1. Fig. 3.7 plots this variation. Each sub-plot shows curves for variations in the skin thickness  $t$  and core depth  $c$ . Changing from one sub-plot to the next represents a change in either skin stiffness  $E_f$  or core density  $\rho_c$ , as indicated by the arrows to the left and top of the figure.

Parameter	Low Value	→	High Value
$t$ , (mm)	0.381	→	$4 \times 0.381$
$E_f$ , (GPa)	1	→	$100 \times 1$
$\rho_c$ , (kg/m <sup>3</sup> )	48	→	$3 \times 48$
$c$ , (mm)	2.5	→	$4 \times 2.5$
Note: The $\rho_c$ refers to the density of Nomex honey-comb with $\rho_s = 724$ kg/m <sup>3</sup>			

**Table 3.1:** The range of the geometric and material parameters used in the parametric study

To characterise the transparency of the skin, it is helpful to identify a semi-wavelength  $L/m$  below which the values of the coefficient  $C_m^{\sigma_{zz}}$  are close to zero so that these wavelengths cannot be transmitted. Examining the curves in Fig. 3.7 it can be seen that the curves all have similar shapes, and that the inflection point in each curve can be used to characterise where  $C_m^{\sigma_{zz}}$  is small. The semi-wavelength at the inflection point characterises the susceptibility of sandwich beams to localised effects, and this semi-wavelength is defined as the *spreading length*  $\lambda$ . In general the larger  $\lambda$  is, the broader is the distribution of the normal out-of-plane stresses in the top skin-core interface, and vice versa.



**Figure 3.7:** Parametric Study; change of transmission coefficient  $C_m^{\sigma_{zz}}$  with wavelength  $L/m$  for variations in the parameters  $t$ ,  $E_f$ ,  $c$  and  $\rho_c$ . The boxed labels show each time the parameters and the arrows indicate the direction of each parameter's increase. The position of inflection is marked by a  $\circ$  symbol

Spreading length  $\lambda$  is a function of the skin thickness  $t$ , skin Young's modulus  $E_f$ , core density  $\rho_c$  and core thickness  $c$ , but it is independent of span length  $L$ . Table 3.2 shows the influence of each parameter to spreading length  $\lambda$ . This table shows the influence of changing the various parameters from the low values given in the left hand column of Table 3.1. Table 3.2 shows that the skin thickness  $t$  is the most significant factor as expected; the larger the skin thickness the stronger the effect of 'spreading stresses'. A similar effect is shown with increasing stiffness  $E_f$  although, given the big change in stiffness of  $\times 100$ , this effect is less important. Core density also affects  $\lambda$ ; the stiffer is the core, the less the external stresses spread. Core thickness  $c$  seems to play a small role.

**Table 3.2:** Change of spreading length  $\lambda$

Low values from Table 3.1 for $t, c, E_f, \rho_c$	$t \rightarrow 4t$	$c \rightarrow 4c$	$E_f \rightarrow 100E_f$	$\rho_c \rightarrow 3\rho_c$
1.6	4.4	2.1	5.0	1.2

At this point, it is important to note that  $\lambda$  is not directly related to the strength of the sandwich beam. Instead it measures how the top skin is able to spread the external load over the core.  $\lambda$  is property of the beam material and geometry. In the following sections we show how it can be normalised and provide a dimensionless index to characterise the spreading effect in sandwich beams under indentation loads.

### 3.5 Contact Pressure Distribution

Having used the high-order sandwich beam theory to characterise the way in which contact loads are transmitted through the top skin, in this section we investigate how this methodology can be applied to the contact between an indenter and a sandwich beam. In the literature there are only a few references relating to the contact stresses exerted between the top skin of a simply supported sandwich beam and an indenter which applies 3-point bending on the beam. Frostig & Baruch [45] examine analytically the effect of four types of localised load distributions; a point load, uniform, sinusoidal distributions or two concentrated loads. These represent very flexible, intermediate and very stiff indenters respectively. Johnson [72] (p.143) investigates thin plates in contact with a rigid indenter and concludes that the contact stress distribution changes from having a maximum in the centre to one in which the pressure is concentrated at the edges, when the thickness of the plate increases. A different problem is examined by Keer and Ballarini [73], who investigate the problem of a rigid punch in smooth

contact with an initially stressed transversely isotropic elastic beam. In this study we investigate how sandwich beams behave under contact with a rigid central roller, calculating the pressure distribution under the indenter and through the beam.

Fig. 3.8 shows a rigid cylinder of radius  $R$  which is pressed into contact with a sandwich beam of unit width and length  $L$ , such that the contact width is  $\delta$ . Equation (3.4) can be used to calculate the top skin displacements for a given distribution of the external load. Following standard contact methods [72] we can divide the contact into a number of discrete sections, calculate the displacements resulting from a unit load on each of these sections, and superimpose the results to find deflections for any contact load. In particular, for a given pressure distribution  $q_t(x)$  it is possible to find the corresponding distribution of heights  $P_i$  (Fig. 3.8a,b) along the top skin. Conversely, we shall show that for a given roller geometry, we can evaluate the contact width and contact pressure by inverting this approach.

The shape of discrete pressure elements can be step functions (Fig. 3.8a) or overlapping triangles (Fig. 3.8b). The second choice is better because the total distributed load function is smoother along the  $x$  direction. In addition the Fourier series converges more quickly for a triangle shape rather than for a rectangular one. The pressure elements on the top skin can be described using the series

$$q_i = P_i \hat{q}_i = P_i \sum_{m=1}^M C_m^{q_i} \sin \frac{m\pi x}{L} \quad (3.15)$$

where  $P_i$  is the height of the triangular distribution and

$$C_m^{q_i} = -\frac{8L}{m^2\pi^2 v} \sin\left(\frac{m\pi x_i}{L}\right) \left(-1 + \cos\left(\frac{m\pi v}{2L}\right)\right)$$

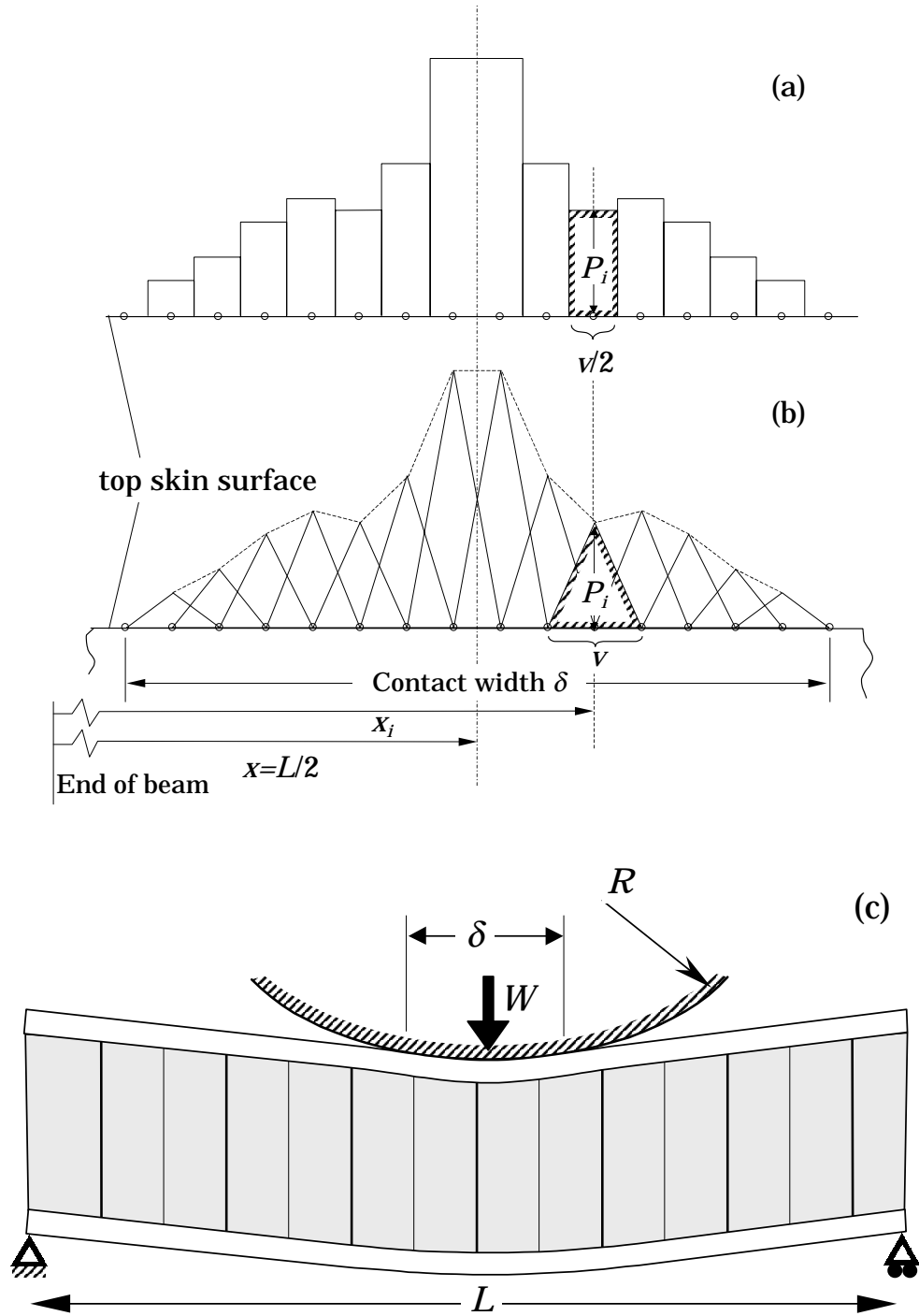
are the Fourier coefficients for an isosceles triangle of unit magnitude. Each unit length has coordinate  $x_i$  and base width  $v$ .  $\hat{q}_i$  is the distribution of pressure  $q_i$  with unit amplitude. For this and subsequent symbols, the ‘hat’ refers to variables relating to this unit pressure distribution. Using the procedure described in section 3.2, the vertical displacements  $w_t^i(x)$  of the top skin associated with each of the triangular pressure elements are given by equation (3.4)

$$w_t^i(x) = P_i \sum_{m=1}^M (C_m^{w_t})^i \sin \frac{m\pi x}{L} = P_i \hat{w}_t^i \quad (3.16)$$

If  $N$  is the number of pairs of symmetrical triangular pressure elements covering a contact width  $\delta$ , then the total overall top skin deflection is given by

$$w_t(x) = \sum_{n=1}^N w_t^i(x) = \sum_{n=1}^N P_i \hat{w}_t^i \quad (3.17)$$





**Figure 3.8:** Discrete contact pressure elements; (a) uniform (piecewise constant), (b) overlapping triangles (piecewise linear) and (c) Geometric definitions

In the case where load is applied by a rigid indenter, which is in perfect contact with the top skin, the top skin deflection follows the shape of the indenter within the contact area. In this section we examine the case of a cylindrical indenter, for comparison with our experiments, but the calculations can be applied to any indenter shape. Having a cylinder of  $R$  radius as a central indenter and assuming perfect contact with the top skin within contact of width  $\delta$ , then the top skin deflection for all  $x \subseteq [\frac{L}{2} - \frac{\delta}{2}, \frac{L}{2} + \frac{\delta}{2}]$  is

$$\begin{aligned} w_t^R(x) &= \sqrt{R^2 - \left(x - \frac{L}{2}\right)^2} - R + w_{t(L/2)} \\ &= \sqrt{R^2 - \left(x - \frac{L}{2}\right)^2} - R + \sum_{n=1}^N P_i \sum_{m=1}^M (C_m^{w_t})_i \sin \frac{m\pi}{2} \\ &= \sqrt{R^2 - \left(x - \frac{L}{2}\right)^2} - R + \sum_{n=1}^N P_i \hat{w}_{t(L/2)}^i \end{aligned} \quad (3.18)$$

where the superscript  $R$  denotes the deflection at the roller. We can also write the equality, only for  $x \subseteq [\frac{L}{2} - \frac{\delta}{2}, \frac{L}{2} + \frac{\delta}{2}]$ , as

$$\begin{aligned} w_t(x) &= w_t^R(x) \\ \text{giving } \sum_{n=1}^N P_i (\hat{w}_{t(x)}^i - \hat{w}_{t(L/2)}^i) &= \sqrt{R^2 - \left(x - \frac{L}{2}\right)^2} - R \end{aligned} \quad (3.19)$$

If we write the above equality for  $N$  different values of  $x_j \in [\frac{L}{2} - \frac{\delta}{2}, \frac{L}{2}]$ , which represent different values of  $w_t(x_j) = w_t^R(x_j)$  along the left half<sup>5</sup> of the contact width  $\delta$ , then we get a system of  $N$  equations with  $N$  unknowns which are the distributions of pressure  $P_i$ . This system can be written in a matrix form

$$[\mathcal{P}] \cdot [\mathcal{W}] = [\mathcal{R}] \quad \text{where} \quad (3.20)$$

$$\mathcal{P} = \begin{bmatrix} P_1 & P_2 & \cdots & P_N \end{bmatrix}$$

$$\mathcal{W} = \begin{bmatrix} \hat{w}_{t(x_1)}^1 - \hat{w}_{t(L/2)}^1 & \hat{w}_{t(x_2)}^1 - \hat{w}_{t(L/2)}^1 & \cdots & \hat{w}_{t(x_N)}^1 - \hat{w}_{t(L/2)}^1 \\ \hat{w}_{t(x_1)}^2 - \hat{w}_{t(L/2)}^2 & \hat{w}_{t(x_2)}^2 - \hat{w}_{t(L/2)}^2 & \cdots & \hat{w}_{t(x_N)}^2 - \hat{w}_{t(L/2)}^2 \\ \vdots & \vdots & \ddots & \vdots \\ \hat{w}_{t(x_1)}^N - \hat{w}_{t(L/2)}^N & \hat{w}_{t(x_2)}^N - \hat{w}_{t(L/2)}^N & \cdots & \hat{w}_{t(x_N)}^N - \hat{w}_{t(L/2)}^N \end{bmatrix}$$

$$\mathcal{R} = \begin{bmatrix} \sqrt{R^2 - (x_1 - \frac{L}{2})^2} - R & \sqrt{R^2 - (x_2 - \frac{L}{2})^2} - R & \cdots & \sqrt{R^2 - (x_N - \frac{L}{2})^2} - R \end{bmatrix}$$

---

<sup>5</sup>Or right half, because of symmetry

Substitution of  $P_i$  into equation (3.15) and summation for all  $N$  triangular pressure elements gives us the contact pressure distribution

$$q_t(x) = \sum_{i=1}^N q_i \quad (3.21)$$

The same concept of superposition can be used to calculate the other stresses, i.e.  $\sigma_{zz}$ . The total load is derived by integration along the  $x$  direction

$$\begin{aligned} W &= \int_0^L q_t(x) dx = \sum_{i=1}^N P_i \sum_{m=1}^M C_m^{q_i} \int_0^L \sin \frac{m\pi x}{L} dx \Rightarrow \\ W &= \frac{2L}{\pi} \sum_{i=1}^N P_i \sum_{m=1}^M m C_m^{q_i}, \quad \text{for } m = 1, 3 \dots M \end{aligned} \quad (3.22)$$

In principle this approach can be used to determine the variation in load distribution and the contact arc  $\delta$  as the total load  $W$  increases. In practice a problem arises at small  $\delta$ . As it is necessary to span the whole beam length with elements, the number of elements needed to deal with sharp variations in pressure becomes prohibitively large. This method is used in the following section to answer the following questions.

1. How accurate is it to assume that the load is distributed uniformly over the contact length  $\delta$ ?
2. How ‘transparent’ is the top skin to the external loads. In other words, how does the distribution of normal stress  $\sigma_{zz}(x)$  in the top skin-core interface compare with the contact stress distribution  $q_t(x)$ ?

### 3.5.1 Case Study

In this section the results from the aforementioned methodology for two extreme cases of skin’s flexural rigidity are presented to illustrate the effect of indenter’s size on the contact stress distribution and the top skin’s transparency to external loads. We consider one sandwich beam (denoted as beam A) with very flexible skins, i.e. 1-ply [90] GFRP laminates with  $t = 0.191$  mm and  $E_f = 1$  GPa, which gives  $\lambda = 0.8$  mm, and another (beam B) with very rigid skins, i.e. 2-ply [0,90] laminates with  $t = 0.381$  mm and  $E_f = 20$  GPa, which corresponds to  $\lambda = 3.7$  mm. Both beams have unit depth, are 60 mm long, have Nomex honeycomb with core density of 128 kg/m<sup>3</sup>, are simply supported and loaded in 3-point bending by a central roller. For each beam two radii for the central roller are considered;  $R = 5$  mm and  $R = 10$  mm. The methodology described in the previous section requires the contact width  $\delta$  as an input data. To

compare results for each roller,  $\delta$  is adjusted manually in a simple numerical algorithm so that, for each beam, the maximum normal stresses in the top skin-core interface are approximately equal.

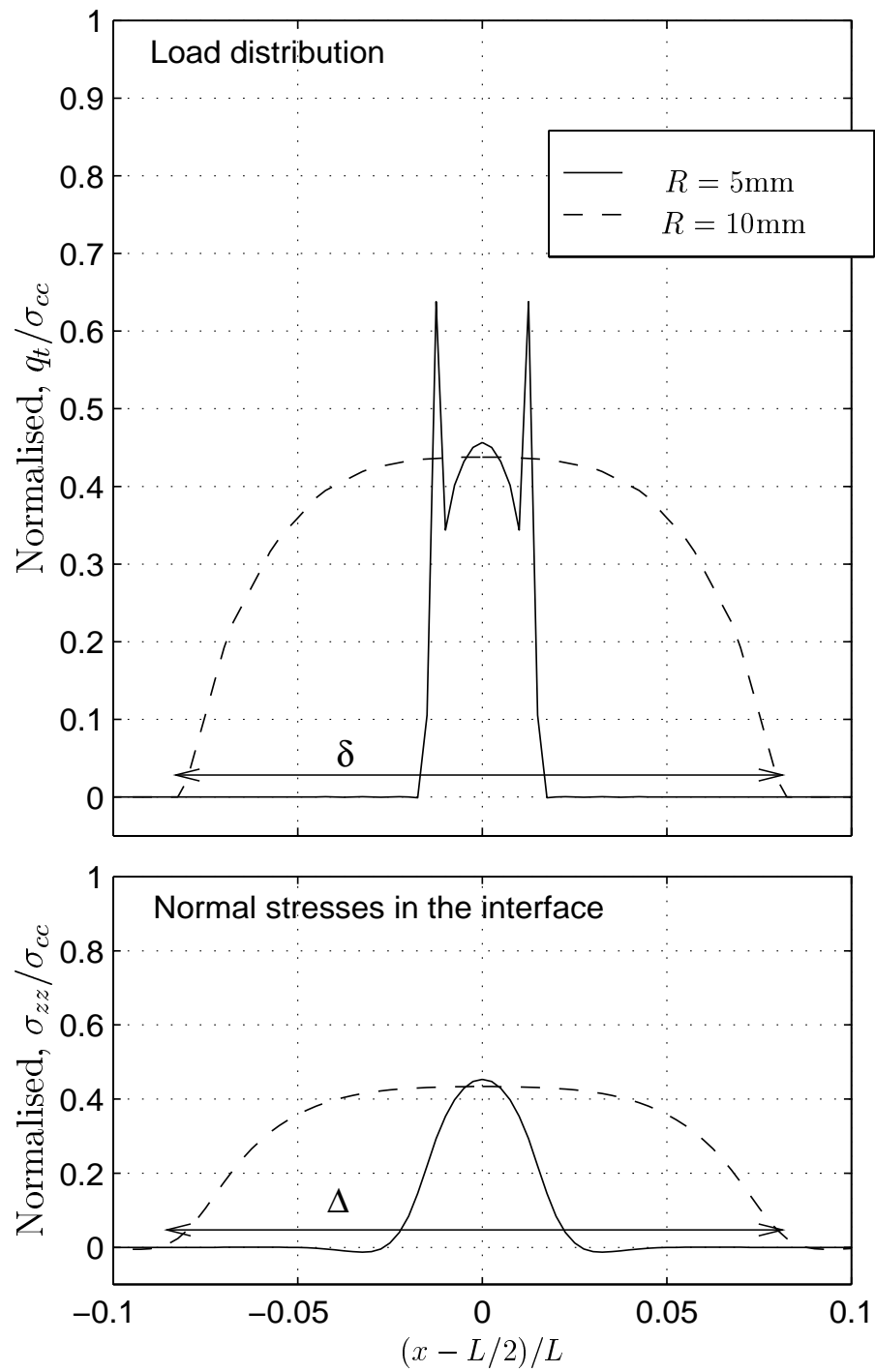
Fig. 3.9 and Fig. 3.10 show the distributions of contact stresses  $q_t/\sigma_{cc}$  and the corresponding normal stresses in the top skin-core interface  $\sigma_{zz}/\sigma_{cc}$  (normalised by the core's out-of-plane compressive strength) for beams A and B, respectively. For beam B the input value of  $\delta$  is chosen to give  $\max \sigma_{zz}/\sigma_{cc} \approx 1$ . However, for beam A this is not feasible. The much greater flexibility of the beam means that it is not possible to generate stresses in the core greater than half the compressive strength of the core without the beam bending excessively. Further loading, by increasing the value of  $\delta$ , induces large skin deformations, which also make HOSBT incapable to model the behaviour of the sandwich beam. Thus for beam A the input value of  $\delta$  is chosen to give  $\max \sigma_{zz}/\sigma_{cc} \approx 0.4$ . However, this difference in peak stress between the two beams is immaterial, as the calculations are elastic and the stress distributions are independent of the applied load.

A particular feature of the contact pressure distribution for the flexible beam A, with  $R = 5$  mm, and for the stiffer beam B with  $R = 10$  mm is the sharp peaks in pressure at the edges of the contact. This feature is also noted by Johnson [72] for similar contacts. These peaks, however, are not transmitted through the skins.

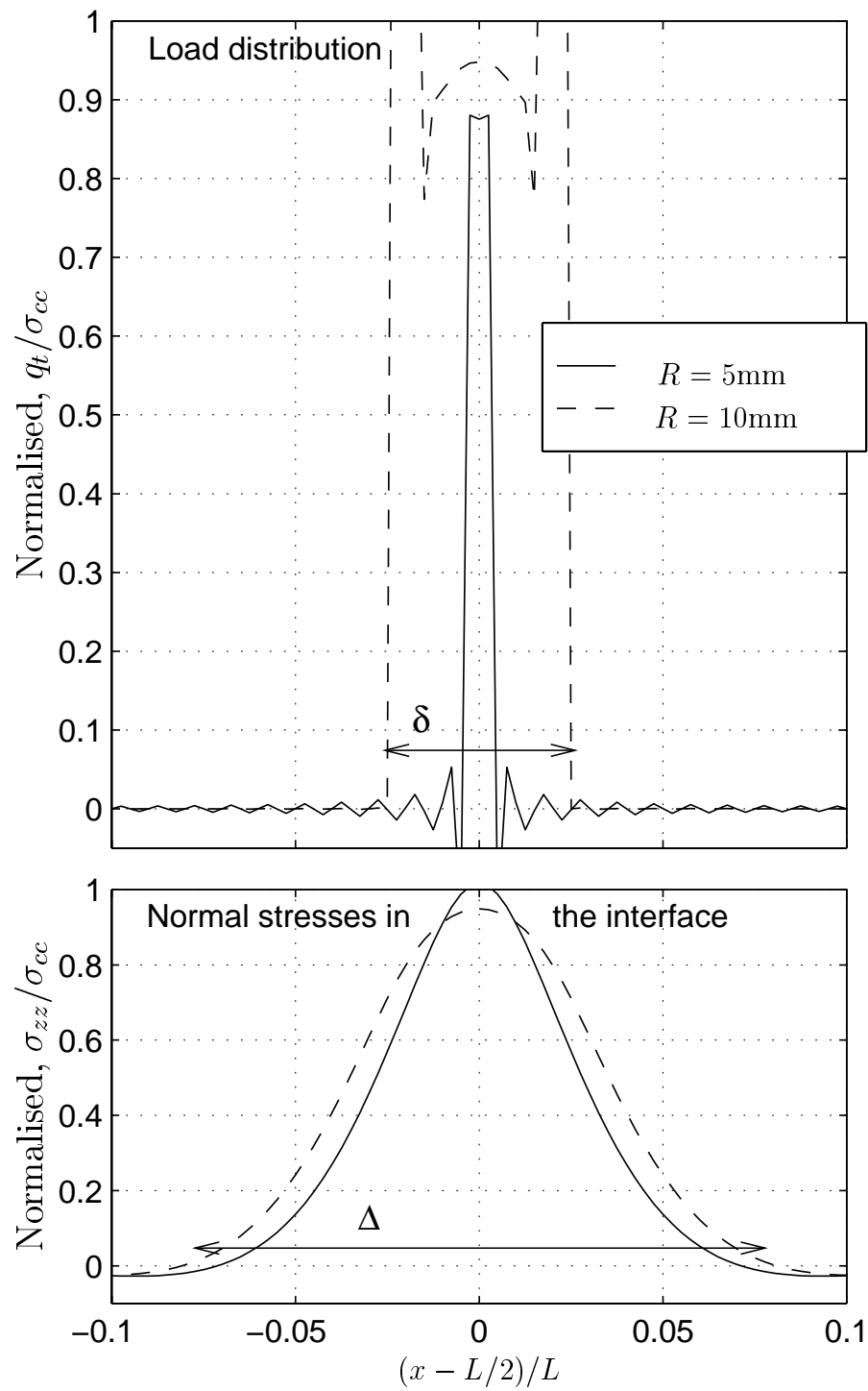
To characterise the degree to which the skins are able to spread the load, we need to compare the width of the contact patch  $\delta$  and the width over which there are significant pressures transmitted across the interface. This latter width can be characterised by a length  $\Delta$ , given when the pressures have positive non-zero values.

Results show that, for the beam B with a rigid skin, Fig. 3.10, the pressure width  $\Delta$  of the pressure distribution in the interface is considerably more than the contact width  $\delta$ , and does not change significantly with roller diameter or contact width. The skin is sufficiently rigid to spread the local pressure distribution out. For beam A with a more flexible skin, Fig. 3.9, the width of the pressure distribution in the interface corresponds to that of the contact. The ratio  $\Delta/\delta$  can be used to measure how well the contact load has been spread out. For a very flexible skin this will equal 1, while for a very rigid skin this will tend to a large value which will depend on the roller radius.

By considering a range of skin stiffnesses changing the thickness  $t$  or/and Young's modulus  $E_f$ , this method can be used to find the variation of  $\Delta/\delta$  for a range of beam spreading lengths  $\lambda$ , for the two roller diameters 5 and 10 mm. This is illustrated in Fig. 3.11. This figure shows that, for very flexible skins with small  $\lambda$ , the width of the contact equals the width of the region in which there are significant pressures across



**Figure 3.9:** Distributions of contact stresses  $q_t/\sigma_{cc}$  and the corresponding normal stresses in the top skin-core interface  $\sigma_{zz}/\sigma_{cc}$  (normalised by the core's out-of-plane compressive strength) for beam A with  $\lambda = 0.8\text{ mm}$



**Figure 3.10:** Distributions of contact stresses  $q_t/\sigma_{cc}$  and the corresponding normal stresses in the top skin-core interface  $\sigma_{zz}/\sigma_{cc}$  (normalised by the core's out-of-plane compressive strength) for beam B with  $\lambda = 3.7\text{ mm}$

the interface, with  $\Delta/\delta = 1$  as expected. As the spreading length  $\lambda$  increases, the distribution of pressure in the interface broadens with respect to the contact width, with larger  $\Delta/\delta$ . This change depends on roller diameter. If we take the transition from flexible to rigid behaviour when  $\Delta/\delta$  equals 2, then this occurs for  $\lambda/R$  equal to 0.24 and 0.25 for the 5 and 10 mm rollers respectively.

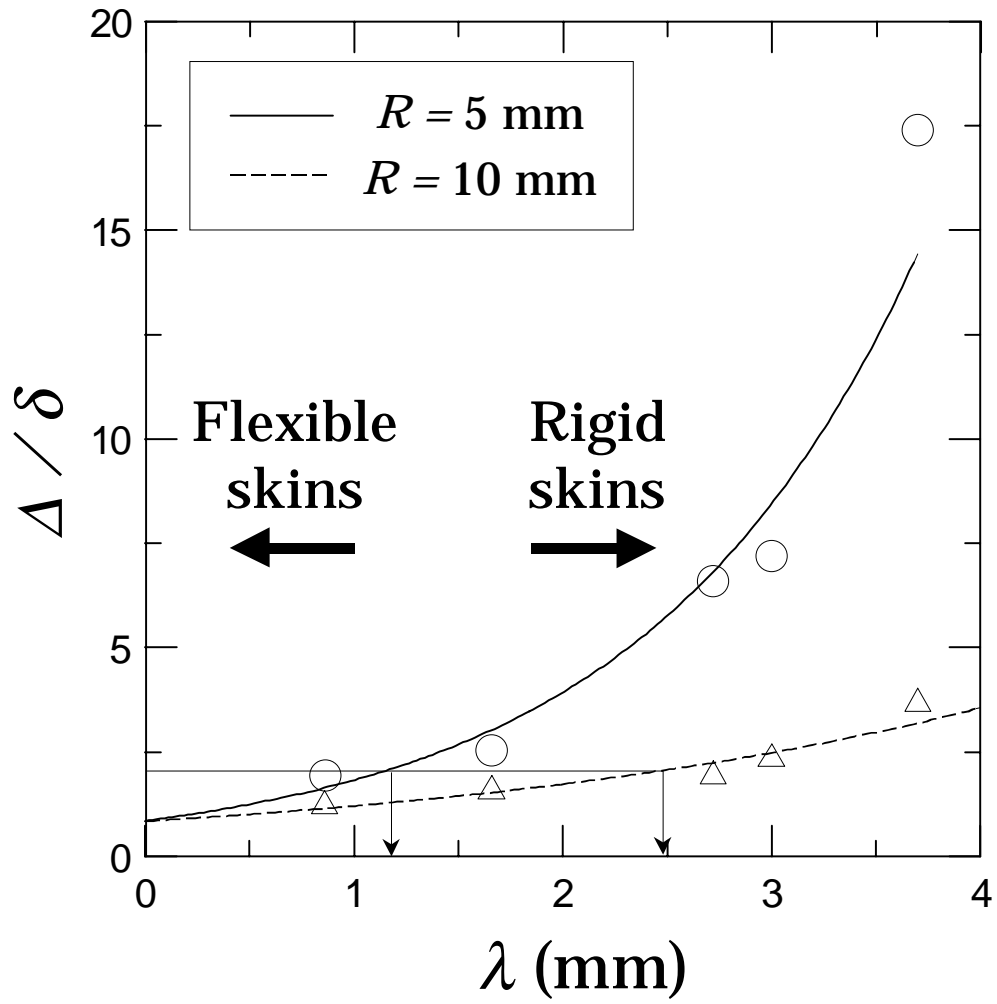
This case study demonstrates the usefulness of the spreading length  $\lambda$  in characterising the beam flexibility. It also allows us to answer the questions posed in section 3.5, relating to the assumptions commonly used to model the contact. Firstly, for practical beams with large  $\lambda$ , the distribution of pressure over the contact is not important, and the assumption that the external load is applied uniformly across the beam will be reasonable. However, this contact distribution will not be transmitted to the interface and the core unchanged. By contrast, Fig. 3.10 shows that it is essential to model beams with stiff skins accurately in order to get a reasonable estimate of the stress distribution in the core. The commonly used assumption that the failure can be predicted using (Failure line load) = (Core's out-of-plane compressive strength,  $\sigma_{cc}$ )  $\times$  (Contact width,  $\delta$ ) will be poor, unless a judicious choice of  $\delta$  is made, based on experimental measurements. In the final section 3.6, we summarise the conclusions from this chapter, including guidelines of a more accurate failure analysis.

### 3.6 Concluding Remarks

The benefits of using the high-order sandwich beam theory (HOSBT) to analyse the behaviour of sandwich beams under indentation are presented. The capabilities of HOSBT are verified experimentally by Surface Displacement Analysis. The symbolic manipulation of the governing equations of HOSBT is used to extract a *spreading length*  $\lambda$ . This is a property of a sandwich beam, depending mainly on the skin's flexural stiffness and characterising the susceptibility of the sandwich beam to indentation loads.

A further manipulation of HOSBT gives an insight into the contact mechanics for loading of a beam by a cylindrical indenter. The way in which the contact pressure is transmitted through the core is examined. A case study shows the fact that sandwich beams used as standard in industry have skins which are rigid enough to spread the external loads.

The most important conclusion from this section is that the maximum stresses  $\sigma_{zz}$ , which are responsible for indentation failure, cannot be predicted in a straightforward way for sandwich beams with rigid skins, even if the contact width  $\delta$  is known. For



**Figure 3.11:** Dependence of spreading effect on roller's radius  $R$  and determination on how flexible or rigid are the skins with respect to the indentation resistance of the sandwich beam



sandwich beams with very flexible skins, the approximation of dividing the total line load  $W$  by  $\delta$  can give us reliable estimation of the failure stresses in the skin-core interface. However for commercially applied sandwich configurations the former case is the dominant.

Thus, in practice one should follow the following steps for indentation failure analysis of sandwich beams:

1. For a particular indenter's size and shape do one test to measure the  $\delta$  just before failure (since  $\delta$  develops with the increase of  $W$ ). This value for  $\delta$  can be assumed for other beam geometries.
2. Use the approximation that the external stresses are uniform within this measured  $\delta$  length. For sandwich beams with small  $\lambda$  this approximation is good, while for sandwich beams with large  $\lambda$  the exact distribution of contact load does not affect the core stresses significantly.
3. Use high order sandwich beam theory and apply the equations (3.8), (3.9) and (3.10) to calculate the stress field in the core. Compare them with the maximum allowables to predict failure.

This approach is adopted in the next chapter to undertake an indentation failure analysis.

# Chapter 4

## Indentation Failure Analysis

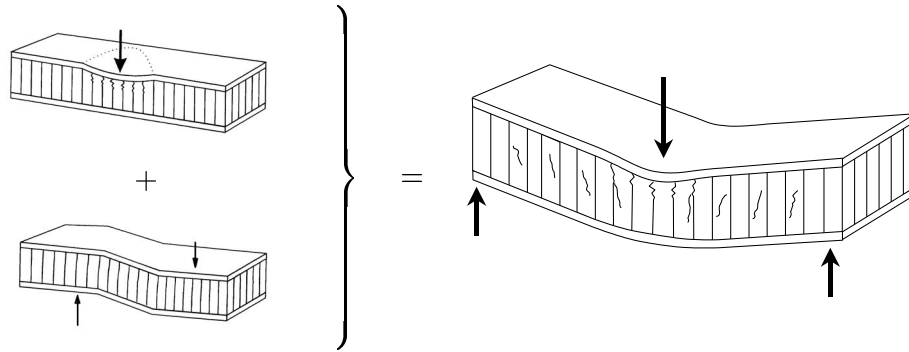
### 4.1 Introduction

If we assume that the behaviour of a sandwich beam is elastic up to failure, the high-order sandwich beam theory can be used to calculate the stresses in the core due to the indentation loading. This can then be compared with the core's out-of-plane compressive strength. However, a more accurate failure criterion for the core is determined from biaxial tests on Nomex honeycomb cores and used in this analysis. Finally short beam 3-point bending tests with three different central roller diameters verify the theoretical predictions and show the importance of the skin flexural rigidity on the beam's overall strength.

### 4.2 Failure Envelope for Nomex Honeycombs

A straightforward way to calculate the failure load by indentation for honeycomb cores is by equating the maximum of the out-of-plane normal stresses  $\sigma_{zz}$  with the allowable stresses  $\sigma_{cc}$ . However the experiments in Chapter 2 showed that the interaction of core shear and out-of-plane stresses was important. The concept of the indentation failure due to these combined stress components is depicted in Fig 4.1. Therefore, before performing an indentation analysis, we investigate both theoretically and experimentally in this section the two-dimensional failure envelope of Nomex honeycombs under shear and out-of-plane compression loading and we define a new failure criterion.

References to biaxial loading tests for cellular materials are not common in the literature. Gibson *et al.* [74] have performed a series of tests on a variety of foams under biaxial, axisymmetric and hydrostatic loading conditions. Zhang and Ashby [28] have investigated the in-plane biaxial buckling behaviour of Nomex honeycombs. More

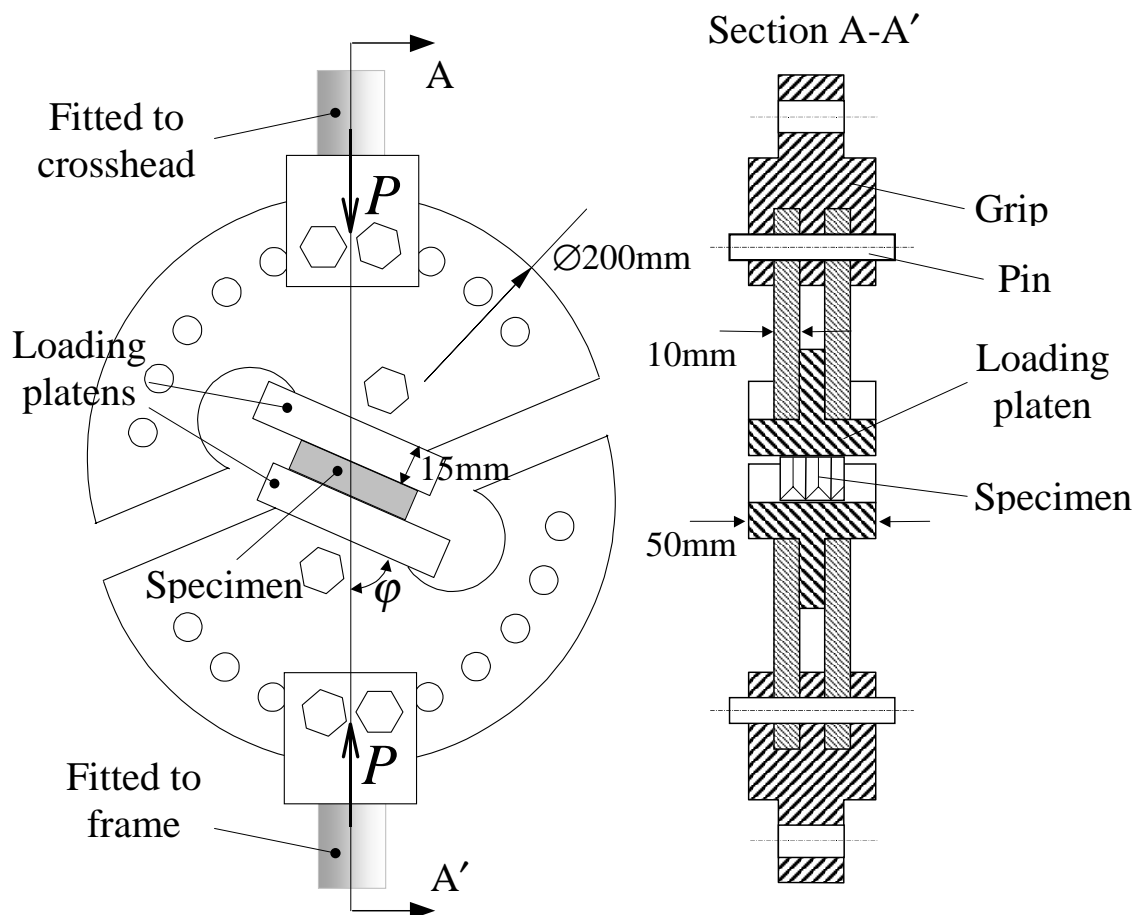


**Figure 4.1:** Combined indentation failure mechanism

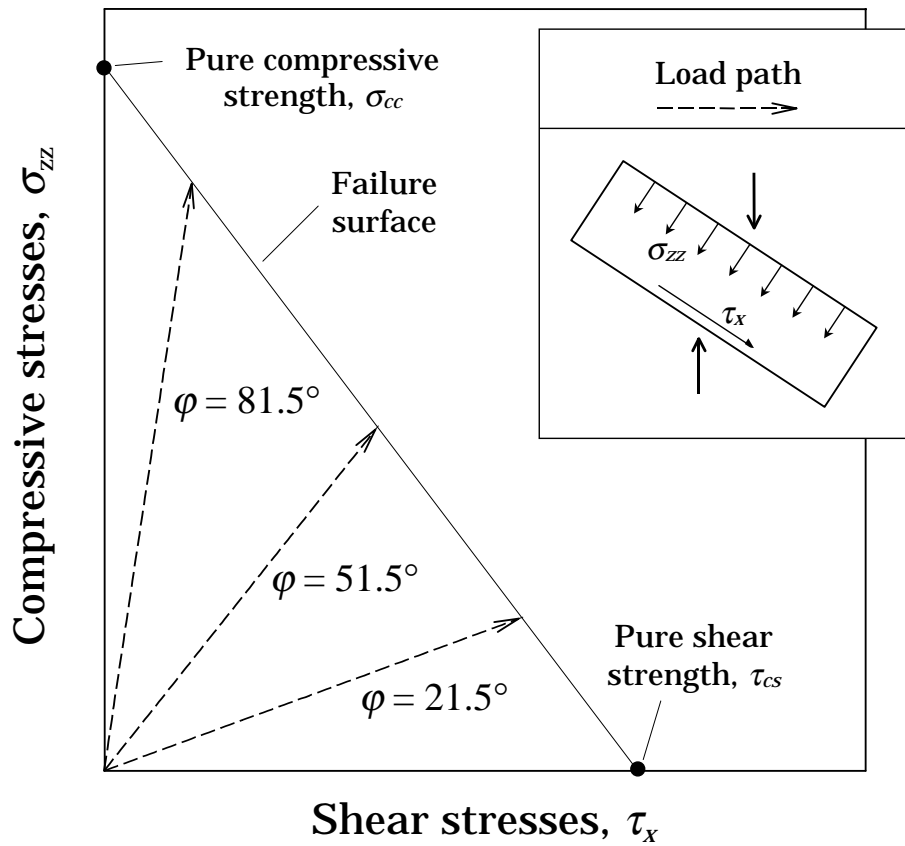
recently Stronge and Klintworth [75] have studied the yield surfaces for honeycombs under biaxial macroscopic stresses.

In this chapter Nomex honeycombs are tested under combined shear and compressive out-of-plane loading. For this purpose, we used the Arcan test rig as illustrated in Fig. 4.2. This geometry was adapted for shear testing of composite materials by Arcan *et al.* [76] and extended to biaxial testing of butterfly-shaped specimens by Voloshin and Arcan [77]. The rig consists of two pairs of plane circular S-shaped parts with antisymmetric cutouts. To accommodate honeycomb specimens we added two loading platens. The bottom pair of semicircular fixtures are gripped to the frame of a servo-hydraulic testing machine. The upper pair are mounted to the load cell and actuator transferring the load to the specimen, which is attached between the two rectangular plates. To ensure a uniform stress through the specimen, the grips are clamped rather than being pivoted, since Marloff's finite element analysis [78] shows that stress uniformity under biaxial conditions is not good. The perimetric holes in the semicircular plates allow a change of the angle  $\varphi$  between the plane of the specimen and the loading direction and therefore the ratio ( $\tan \varphi$ ) of compression to shear applied to the specimen between the central plates. The specimens are rectangular plates of no more than 45 mm in width or length.

The success of such tests depends on being able to attach the specimen to the loading platens effectively. In this case the flat external surface of the skins can be easily attached with standard acrylic adhesive. Specimens were prepared by cutting rectangular pieces from each of the available sandwich panels of 4 different densities as described in Chapter 2. Although the aim of this work is to examine the behaviour of the honeycomb core, the presence of the skins does not pose any difficulties; on the contrary they restrict movement of the honeycomb walls relative to the grips and help attachment of the specimen to the rig. For each core density, tests were conducted for

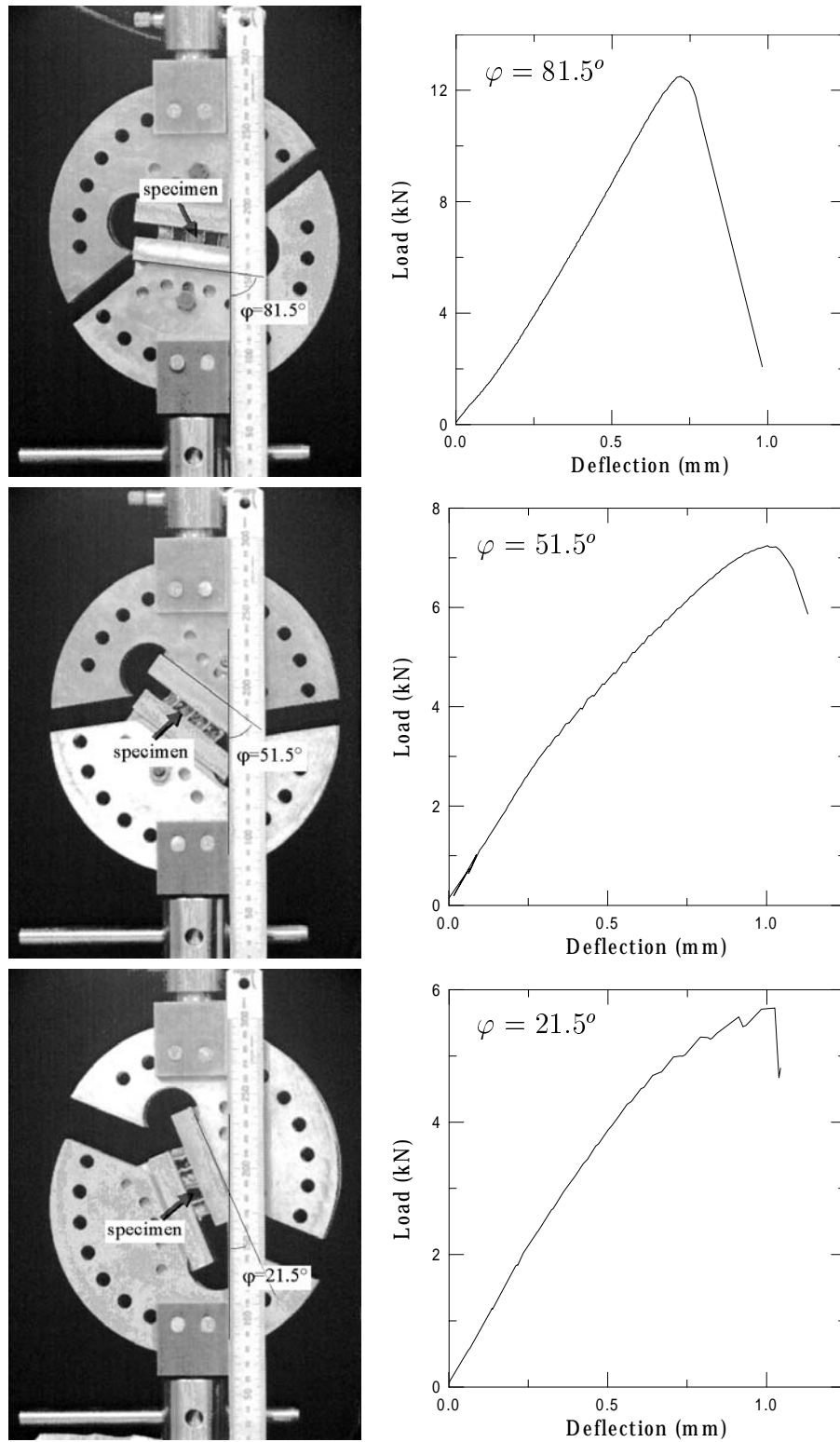
**Figure 4.2:** The Arcan-type rig

both orientations of the honeycomb ribbon (longitudinal and transverse). Loading was monotonic up to failure, with a constant displacement rate of 0.3 mm/min. In order to cover a wide range from nearly pure compression to nearly pure shear, tests were made at three angles of  $\varphi = 21.5^\circ$ ,  $51.5^\circ$  and  $81.5^\circ$ . Fig. 4.3 shows the corresponding load paths. Failure for each of the shear angles  $\varphi$  defines one point on the failure surface, with corresponding values of the core normal and shear stresses  $\sigma_{zz}$  and  $\tau_x$  at failure. In Fig. 4.4 photos of the three angle setups and typical load-deflection curves are presented. The deflection is measured from the crosshead displacement of the machine.



**Figure 4.3:** Load paths and determination of failure envelope

The failure peak loads give the combination of normal compressive load ( $P \sin \varphi$ ) and shear load ( $P \cos \varphi$ ) which leads to failure. Assuming that these loads are distributed uniformly over the external surfaces (of area  $b \times L$ ) of both skins, the compressive and shear stresses in the core are given by  $P \sin \varphi / (bL)$  and  $P \cos \varphi / (bL)$  respectively. The calculated failure stresses  $\sigma_{zz}$  and  $\tau_x$  are normalised by the core's out-of-plane compressive strength  $\sigma_{cc}$  and shear strength  $\tau_{cs}$  respectively, as given by equations (2.18), (2.19a) and (2.19b). Normalised stresses  $\sigma_{zz} / \sigma_{cc}$  are plotted against  $\tau_x / \tau_{cs}$  for every



**Figure 4.4:** The three angle setups and the corresponding load-deflection curves (here for specimens with  $128 \text{ kg/m}^3$  core density)

angle, core density and both honeycomb ribbon directions in Fig. 4.5. Except for the honeycombs with density 128 kg/m<sup>3</sup> the failure envelopes are well approximated by a linear failure criterion given by

$$\frac{\sigma_{zz}}{\sigma_{cc}} + \frac{\tau_x}{\tau_{cs}} = 1 \quad (4.1)$$

as illustrated in Fig. 4.5 by the dashed line. The inconsistency observed in the 128 kg/m<sup>3</sup> honeycombs is due to an inconsistency in the measured shear stresses, and does not affect the accuracy of our calculations.

Thus equation (4.1) allows us to define a failure criterion for combined loading cases, as required for an indentation failure analysis.

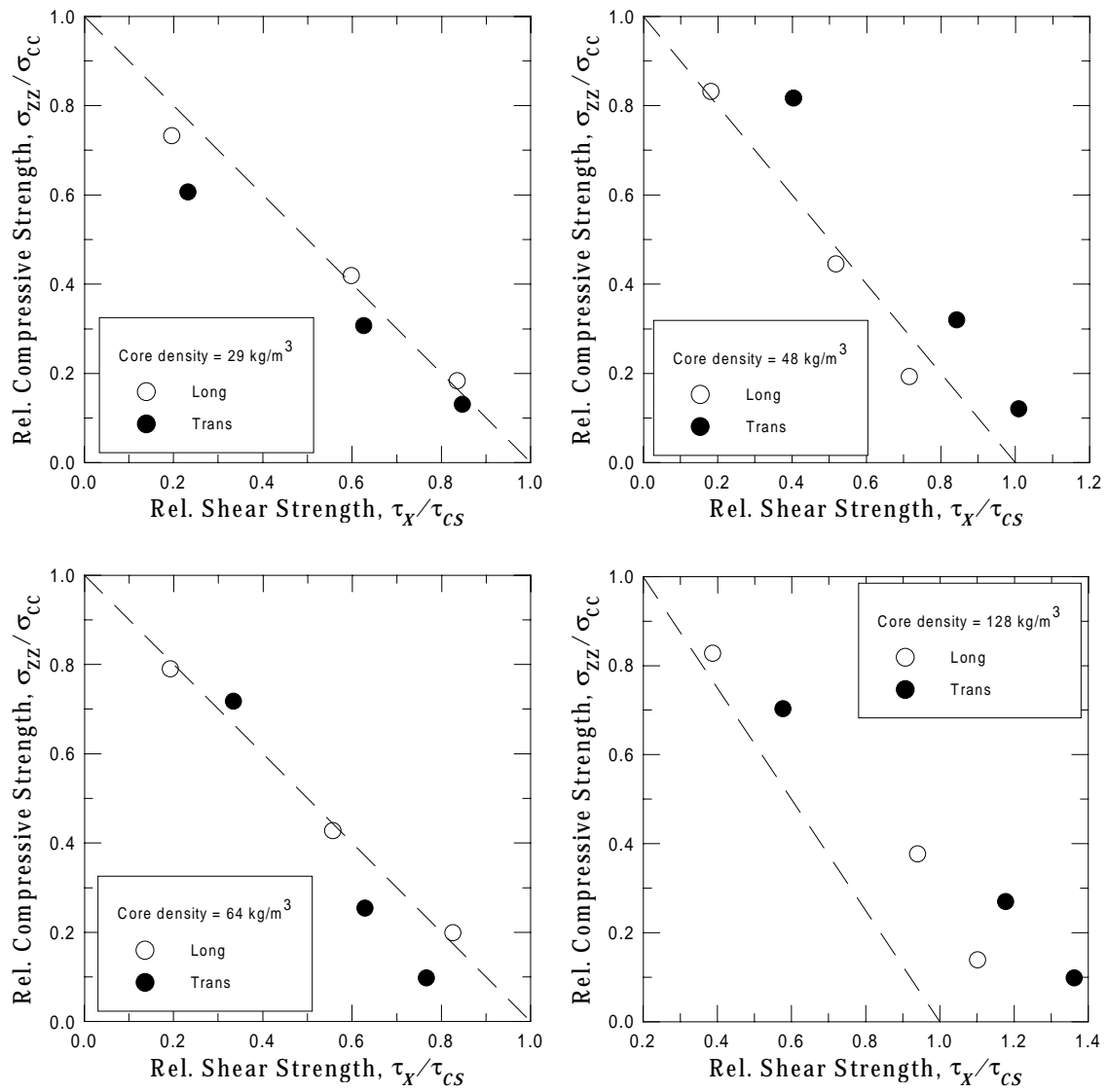
### 4.3 Failure Analysis with HOSBT

In section 3.2 the basics of high-order sandwich beam theory's implementation to sandwich beam bending behaviour analysis were presented. Here the equations needed for a failure analysis for honeycomb sandwich beams loaded under 3-point bending are assembled. To simplify our calculations we assume that the external loads (applied by the central roller) are uniform within a given width  $\delta$  in the midspan of the beam. This assumption is discussed in section 3.6. So for a uniformly distributed load applied in the midspan of the beam the Fourier coefficient  $C_m^{qt}$  [c.f. eqn. (3.7)] reads

$$C_m^{qt} = \frac{4W}{m\pi\delta} \sin\left(\frac{m\pi}{2}\right) \sin\left(\frac{m\pi\delta}{2L}\right) \quad \text{or} \quad C_m^{qt} = W\hat{C}_m^{qt} \quad (4.2)$$

where  $W$  is the total line load. For the failure analysis, we need to know the stress field in the core-top skin interface; i.e. the out-of-plane normal stresses  $\sigma_{zz}$  and  $\tau_x$  (see Fig. 3.2b). Substitution of the above coefficients  $C_m^{qt}$  into equation (3.12) gives the Fourier coefficients  $C_m^{wt}$ ,  $C_m^{wb}$ , and  $C_m^{\tau_x}$  for the top and bottom skin deflections and for core shear stresses

$$\begin{aligned} C_m^{wt} &= C_m^{qt} \frac{\mathbf{R}_1}{(\mathbf{D}_f - \mathbf{E}_c)(\mathbf{R}_1 + \mathbf{R}_2)} \\ C_m^{wb} &= C_m^{qt} \frac{-\mathbf{R}_2}{(\mathbf{D}_f - \mathbf{E}_c)(\mathbf{R}_1 + \mathbf{R}_2)} \\ C_m^{\tau_x} &= C_m^{qt} \frac{\mathbf{A}_f \mathbf{C}_t}{\mathbf{R}_1 + \mathbf{R}_2} \end{aligned}$$



**Figure 4.5:** Failure envelopes for Nomex honeycombs. The dashed line corresponds to the linear failure criterion given by equation (4.1)



Then from equations (3.4)-(3.6) and (3.10), the required stresses are given as follows

$$\sigma_{zz}(x) = W \sum_{m=1}^M \hat{C}_m^{qt} \left( \frac{\mathbf{E}_c}{\mathbf{D}_f - \mathbf{E}_c} - \frac{c m \pi}{2L} \frac{\mathbf{A}_f \mathbf{C}_t}{\mathbf{R}_1 + \mathbf{R}_2} \right) \sin \frac{m \pi x}{L} \equiv W \hat{\sigma}_{zz}(x) \quad (4.3)$$

$$\tau_x(x) = W \sum_{m=1}^M \hat{C}_m^{qt} \frac{\mathbf{A}_f \mathbf{C}_t}{\mathbf{R}_1 + \mathbf{R}_2} \cos \frac{m \pi x}{L} \equiv W \hat{\tau}_x(x) \quad (4.4)$$

The variation of the stresses  $\sigma_{zz}(x)$  and  $\tau_x(x)$  with position  $x$  along the beam and with load  $W$  can be represented in  $\sigma$ - $\tau$  space by lines such as that shown dashed in Fig. 4.6. For every  $W$  the lowest part of the curve corresponds to the edge of the beam ( $x = 0$ ), where shear stresses are dominant, but still there are some out-of-plane normal stresses (hence the curve does not touch the  $x$ -axis). Towards the midspan of the beam, (i.e. the upper section of the curve) the out-of-plane normal stresses increase, while the shear stresses decrease (falling to zero at  $x = L/2$ ). As  $W$  increases, the stresses increase until the failure envelope, shown by a solid straight line, is reached at a failure load  $W_o$ . This failure load will differ significantly from that based on pure compressive loading.

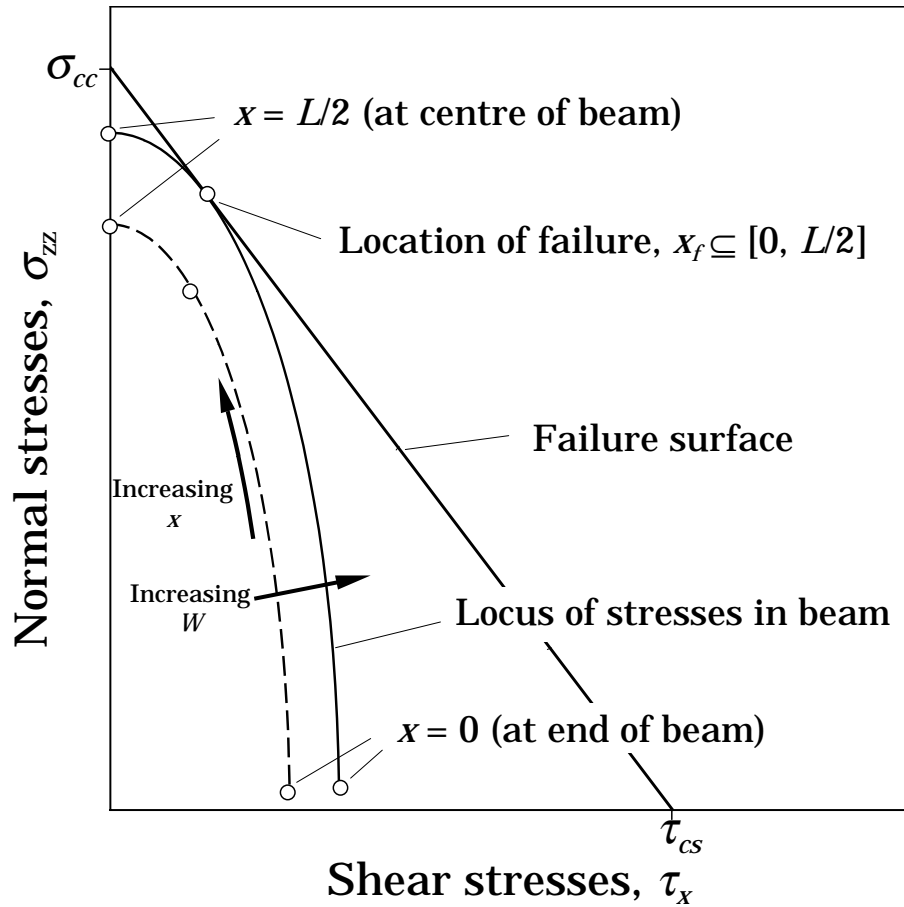


Figure 4.6: Combined failure criterion

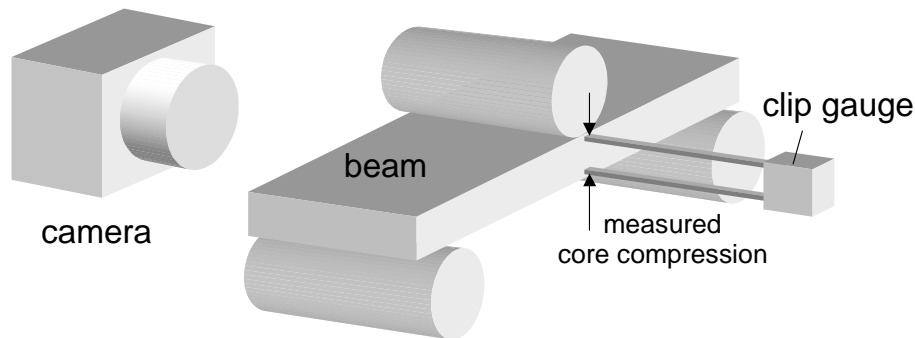
$W_o$  can be calculated after substituting equations (4.4) and (4.3) into equation (4.1) and finding the minimum value of the following expression

$$W = \frac{\sigma_{cc}}{\hat{\sigma}_{zz}(x) + \frac{\sigma_{cc}}{\tau_{cs}} \hat{\tau}_x(x)} \quad (4.5)$$

## 4.4 Experimental Work

To validate the theoretical predictions for the indentation failure loads, 3-point bending tests were performed on short sandwich beams. Beams 70 mm long and 30 mm wide were cut in both honeycomb ribbon directions from Nomex core sandwich panels. Panels had nominal core densities 29, 48, 64 and 128 kg/m<sup>3</sup> with a 3 mm cell size and 32 kg/m<sup>3</sup> with a 5 mm cell size. To observe in detail the vertical deflections during loading we painted one of the specimens' long cross sections so that the surface of the honeycomb walls became black and the edges of both skins and of honeycomb walls became white.

The experimental setup is depicted in Fig. 4.7. It consists of a video camera and recorder, which keep track of the high contrast black and white cross sections of the specimens during loading. The specimens are simply supported by two rollers of 20 mm diameter. The distance between them is 60 mm. 3-point bending tests were performed with 3 different diameters (6, 10 and 20 mm) of the central roller in a servohydraulic testing machine. The loading rate was 0.5 mm/min. As well as the midspan top skin deflection and the load measurements, which are given by the machine's transducers, we attached in the midspan of every specimen a clip gauge to measure the relative displacement between the skins.



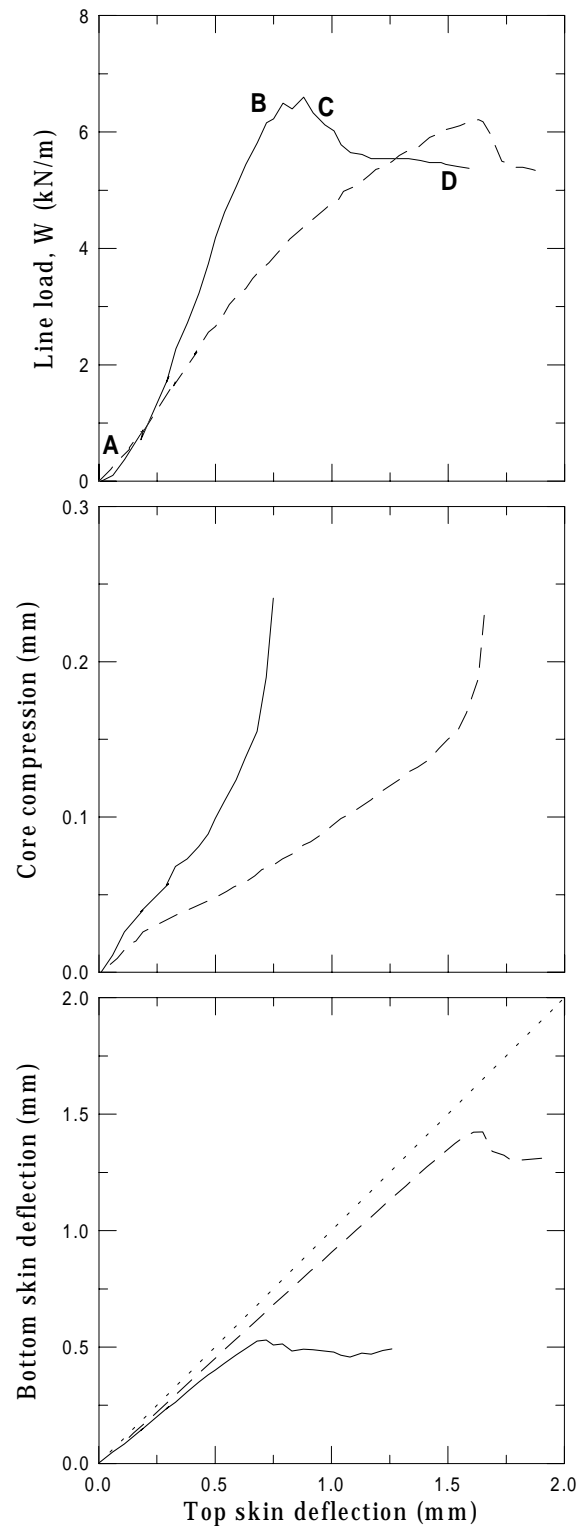
**Figure 4.7:** Experimental setup

The experimental measurements of midspan core compression from the clip gauge, of load from the load cell and of top skin deflection from the crosshead displacement

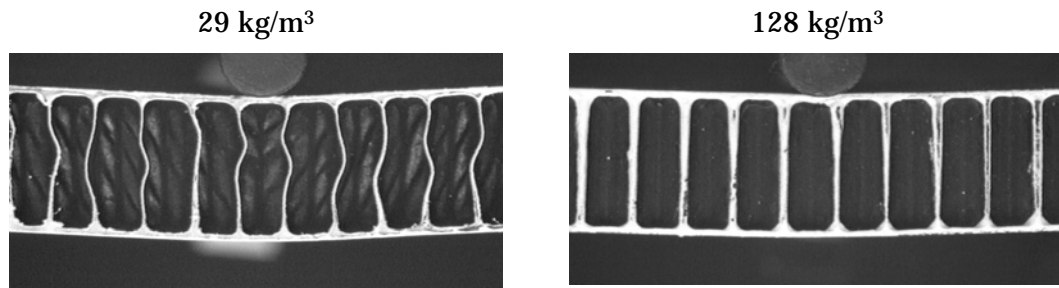
transducer are plotted for every central roller size and every core density in Figs. A.1, A.2 and A.3 in Appendix A. A representative combined plot is shown here in Fig. 4.8. The bottom skin deflection vs top skin deflection curves show clearly the different response of the two skins; the top skins exhibit larger absolute deflections than the bottom skins. This is due to the compression of the core as shown clearly by the core compression vs top skin deflection curves. Core compression is almost linear up to failure. For all core densities the core compression is more severe for the beams with longitudinal honeycomb ribbon direction, due to the higher shear stiffness of the Nomex honeycomb in the longitudinal direction than in the transverse direction. This difference confirms the importance of the core shear stiffness in indentation failure. The difference between longitudinal and transverse ribbon directions is also reflected in the line load-deflection curves; in the former case the beam has a higher overall flexural rigidity.

The letters A, B, C, and D in the upper plot of Fig. 4.8 indicate critical stages of the loading procedure (i.e. before loading, just before failure, just after failure and well after failure). At these points video snapshots were captured. These are presented for every central roller size and core density in Figs. A.4, A.5 and A.6 in Appendix A. Here we present some key photos for discussion. Fig. 4.9 shows two video images captured just before failure (position B in Fig. 4.8) during 3-point bending loading with a 6mm diameter central roller. It is apparent how the low density core is deformed with significant shear, causing the honeycomb cell walls to buckle elastically. Fig. 4.10 shows the effect of core density after failure, when the total deflection is approximately 2 mm. The high out-of-plane stiffness of the high density core does not allow the damage to propagate within the core and the skins fail eventually by compressive macrobuckling. For the same reason the indented top skin follows tightly the curvature of the roller for high density cores, while for low density cores the top skin is indented over a wider area without following the indenter's curvature (see Fig. 4.11).

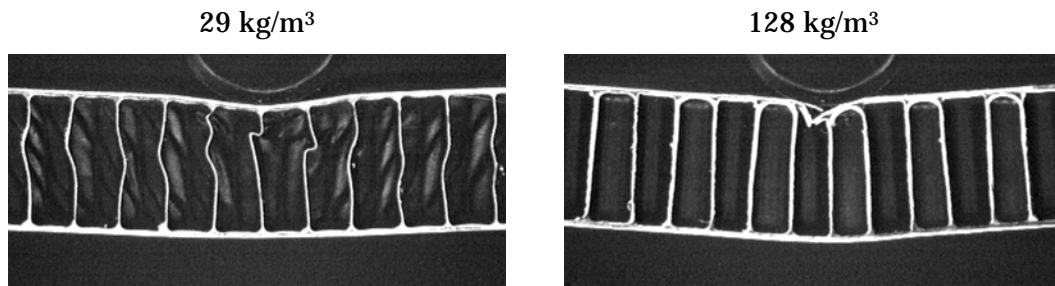
After comparing the corresponding curves amongst Figs. A.1, A.2 and A.3 we realise that there are no significant differences due to the central roller's size. This is in accordance with the prediction made in Chapter 3. This insensitivity to the indenter's size is confirmed by comparing the corresponding failure peak loads in Fig. 4.12. The same figure also shows the satisfactory theoretical predictions using the high-order sandwich beam theory in conjunction with the mixed failure criterion. The values of out-of-plane core compressive strength and core shear strength calculated in section 2.2.3 for every core density and ribbon direction are substituted in equation (4.5) and the minimum value of this provides the theoretical predictions of failure loads, which are represented by the lines in Fig. 4.12. The advantage of using the mixed failure crite-



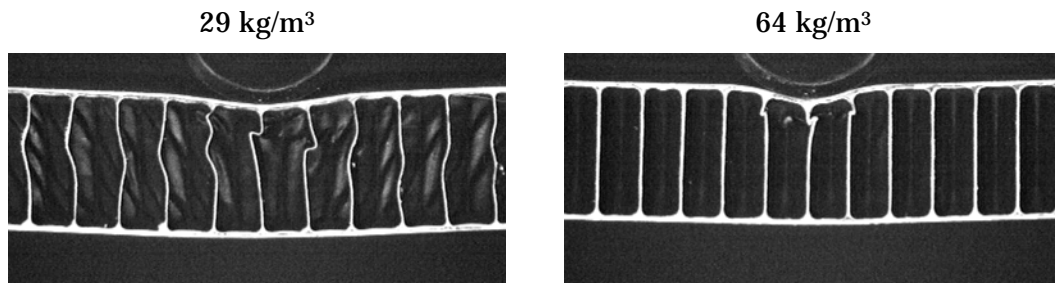
**Figure 4.8:** Typical experimental results for sandwich beam with  $29 \text{ kg/m}^3$  core density loaded by a roller with diameter of 6 mm. Midspan bottom skin deflection, midspan core compression, and line load are plotted against midspan top skin deflection. Lines legend: (—) longitudinal and (---) transverse honeycomb ribbon direction



**Figure 4.9:** The pre-failure influence of core density. Video images captured just before failure during 3-point bending loading with a 6mm diameter central roller



**Figure 4.10:** The post-failure influence of core density. Video images captured after failure (2 mm total deflection) during 3-point bending loading with a 10mm diameter central roller



**Figure 4.11:** The post-failure influence of core density on extent of damage. Video images captured after failure (2 mm total deflection) during 3-point bending loading with a 10mm diameter central roller

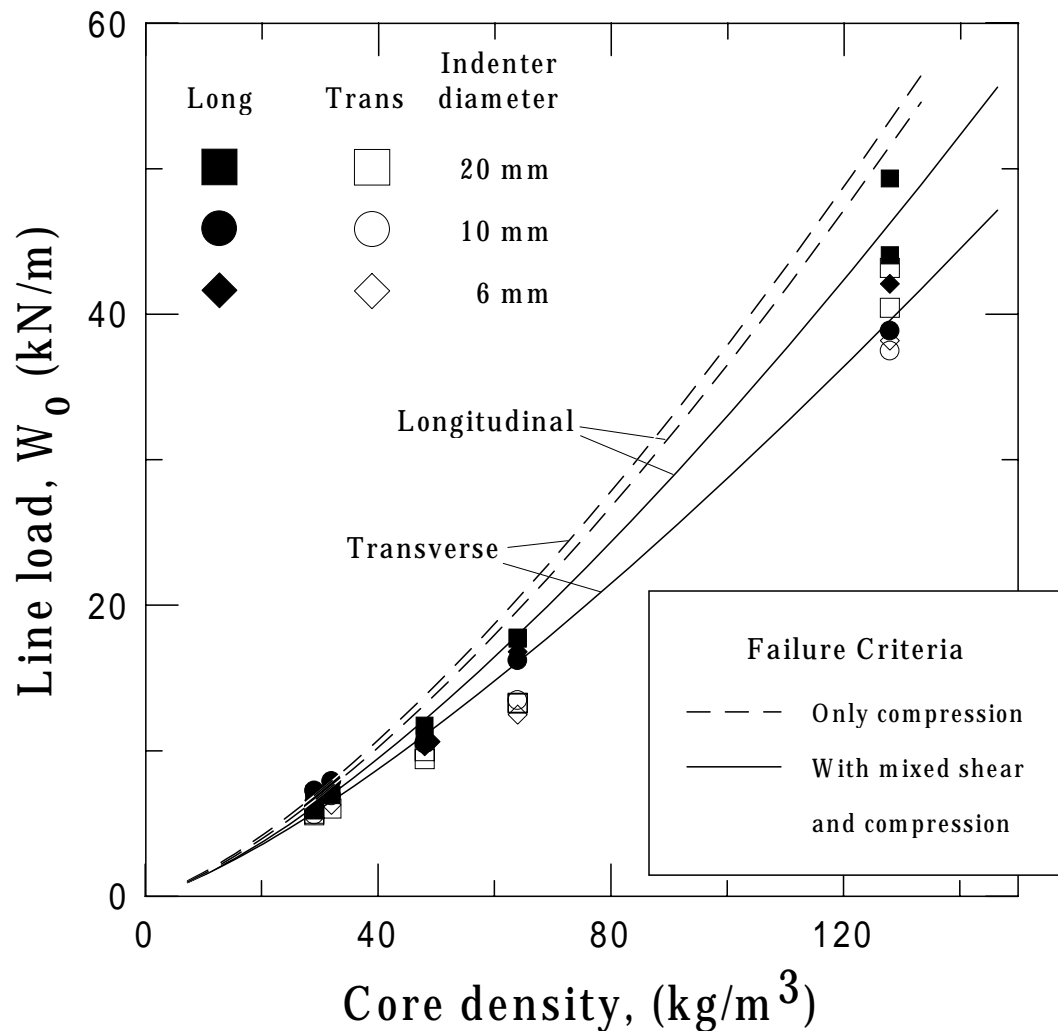
tion instead of simply checking when the maximum out-of-plane stresses in the top skin-core interface reach the out-of-plane compressive strength of the honeycomb core is illustrated in Fig. 4.12. It is shown that, without the correction of the mixed criterion, the theoretical predictions are larger than the experimental data measurements of the failure loads, especially as the core density increases. Also the use of the mixed failure criterion ‘catches’ the different indentation resistance of sandwich beams due to the different honeycomb ribbon direction. The sandwich beams with longitudinal honeycomb ribbon direction have slightly higher strengths than those with a transverse ribbon direction. The difference increases with the core density.

## 4.5 Concluding Remarks

A systematic approach has been developed to determine the failure load of sandwich honeycomb structures under indentation loading. Firstly the failure envelope for Nomex honeycombs under simultaneous out-of-plane compression and shear has been determined by biaxial tests using an Arcan rig. A linear dependence on pure compression and shear proves to be a good approximation for the failure envelope of Nomex honeycombs.

The implementation of high-order sandwich beam theory allows a more accurate failure analysis for sandwich beams subjected to localised loads. Using the failure envelope determined by the biaxial tests, a mixed failure criterion has been introduced to predict the indentation failure, caused by the simultaneous action of out-of-plane compressive and shear stresses exerted in the vicinity of a localised load. This criterion can predict failure that ranges from pure core crushing to pure core shear.

The short beam bending tests validated the theoretical predictions of high order beam model. Video captures of the deformed side cross section illustrate the involvement of core shear in the elastic behaviour of sandwich beams with low density cores. Also these tests showed the different post-failure damage extent between sandwich beams with different core densities. They showed that the mixed failure criterion offers a significant improvement in predicting indentation strength, as compared with models which do not include combined loading. This model is particularly needed in high core densities which induce more severe stress fields in the core. Moreover this approach explains observed differences in behaviour for longitudinal and transverse ribbon directions.



**Figure 4.12:** Theory (lines) vs experimental results (symbols) for failure line load  $W_o$

# Chapter 5

## Failure Maps using HOSBT

### 5.1 Introduction

In Chapter 2 failure mode maps for Nomex honeycomb sandwich beams with GFRP laminate skins are produced using simplified beam models and honeycomb mechanics. However, the simplified model for indentation failure prediction used in chapter 2 can not be used with great confidence, especially where core crushing and shear interact. In the previous chapter a theoretical model based on high-order sandwich beam theory (HOSBT) and a mixed failure criterion for Nomex honeycombs has been shown to give accurate predictions of the peak loads when sandwich beams made of GFRP skins and Nomex honeycomb fail by indentation. Here the use of high-order beam theory is extended as a compact computational tool, which determines the maximum stresses in the skins and the core. Thus by comparing the calculated maximum stresses with the relevant allowable stresses, we find the range of design parameters where each failure mode is dominant. Frostig and Shenhar [40] have conducted an analogous failure analysis for foam core sandwich panels by using the HOSBT, but for failure patterns and criteria different than those we present here. In particular, the failure mode of skin wrinkling is not examined. Furthermore, specifically for the failure mode of indentation, the failure criterion for the core was based on the maximum principal stresses. Although this approach is appropriate for foams that are isotropic, in case of honeycombs, which are orthotropic, a more suitable failure criterion is that based on the normal and shear stresses exerted in the top skin-core interface. Thus in this chapter we make use of the mixed failure criterion, introduced in the previous chapter. Based on the above approach, new failure mode maps for Nomex honeycomb sandwich beams are constructed and provide the basis for design optimisation carpet plots.



## 5.2 Reconstruction of Failure Maps

In chapter 3 we presented the basics of high order beam theory's implementation to sandwich beam bending behaviour analysis. By assuming a linear elastic response for the sandwich beam up to failure, it is feasible to use the appropriate equations derived by high order beam theory to calculate the maximum stresses in the skins and the core under 3-point bending. The advantages of such approach are: (1) use of a compact computational tool to calculate all the maximum stresses in the sandwich beam, and (2) ability to use mixed failure criteria for the core to model more accurately the indentation failure, as shown in the previous chapter.

The experimental results presented in Chapter 2 show that the short beams finally failed by core crushing under the central load, but with an increased interaction of core shear as the core density gets smaller. Thus in this chapter the core shear is not considered as a separate failure mode. The failure in the honeycomb core is treated as one mixed failure mode and denoted as *core indentation*. The theoretical determination of the peak load for this mode is presented thoroughly in the previous chapter and gives

$$W_o = \min \frac{\sigma_{cc}}{\hat{\sigma}_{zz}(x) + \frac{\sigma_{cc}}{\tau_{cs}} \hat{\tau}_x(x)} \quad (5.1)$$

These calculations are based on the assumption that the external loads (applied by the central roller) are uniform within a measured width  $\delta$  in the midspan of the beam. As explained in Chapter 3, the rigidity of the laminate skins used in the examined sandwich beams is high enough that the calculations are insensitive to the contact area between the indenter and the top-skin. It is assumed in this chapter that this remains true.

For the skin failure we need to know the maximum normal stresses  $\sigma_{txx}$  exerted on the cross-section of the top skin. Equation (3.9), after substitutions, gives

$$\sigma_{txx}(x) = W \sum_{m=1}^M \hat{C}_m^{qt} \frac{\mathbf{C}_t}{\mathbf{R}_1 + \mathbf{R}_2} \frac{m\pi}{L} \sin \frac{m\pi x}{L} \equiv W \hat{\sigma}_{txx}(x) \quad (5.2)$$



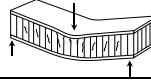
This is a function of the  $x$  coordinate and the maximum value is reached (as expected) in the midspan of the beam, i.e. for  $x = L/2$

$$\max \sigma_{txx} = W \hat{\sigma}_{txx}(x=L/2) \quad (5.3)$$

Now the failure loads for every failure mode are calculated by equating these maximum stresses with the allowable stresses  $\sigma_{fY}$ ,  $\sigma_{fw}$  for skin compressive yield and skin wrinkling respectively.

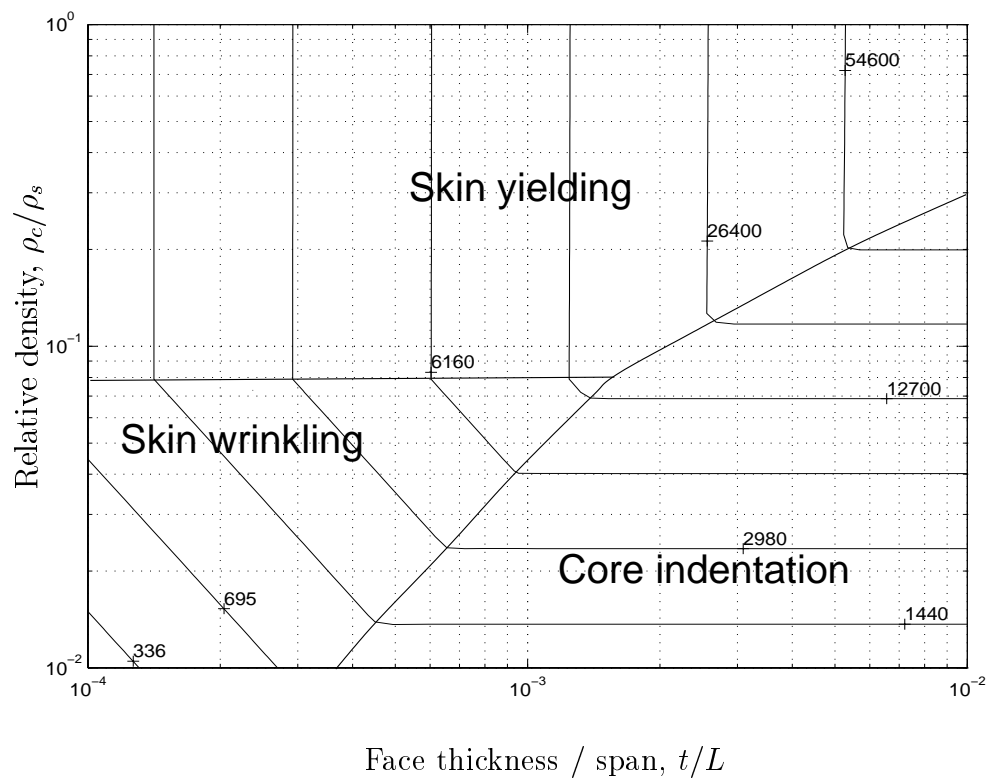
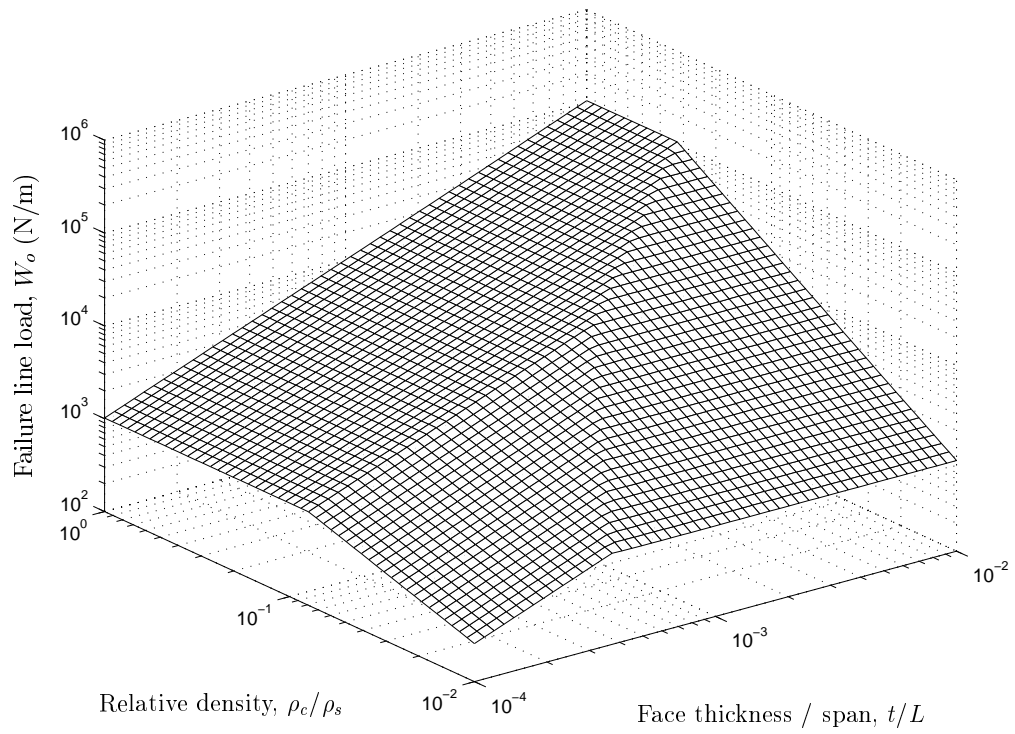
As in Chapter 2, a failure map for this type of sandwich beam is constructed by finding the minimum failure loads for each of the failure modes in Table 5.1 for each value of the design parameters (i.e.  $t/L$  and  $\rho_c/\rho_s$ ). Then we plot the minimum load

**Table 5.1:** Expressions for peak failure loads

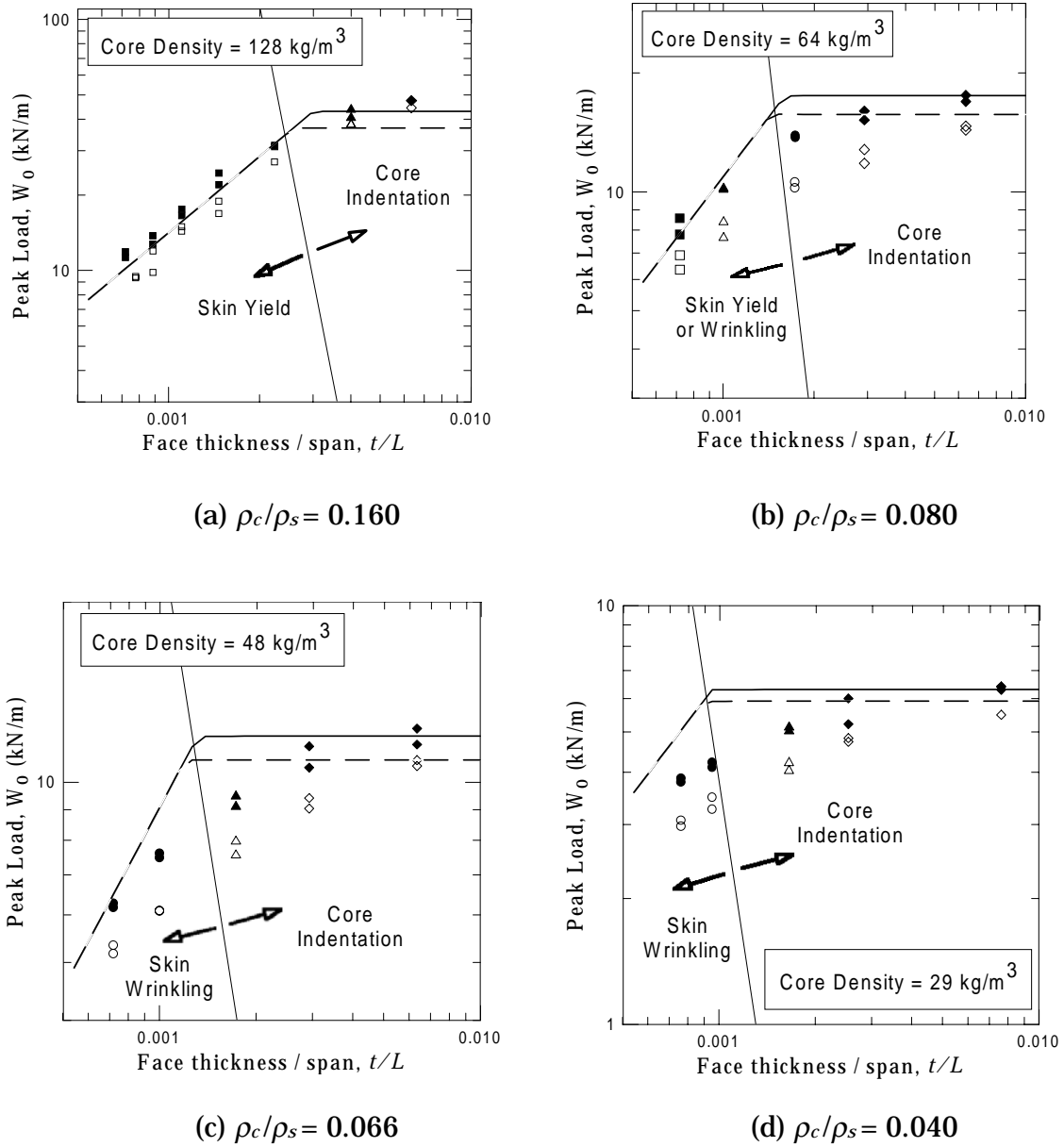
Top skin yield		$W_o = \sigma_{fY}/\hat{\sigma}_{txx}$
Face wrinkling		$W_o = \sigma_{fw}/\hat{\sigma}_{txx}$
Indentation		$W_o = \min \frac{\sigma_{cc}}{\hat{\sigma}_{zz}(x) + \frac{\sigma_{cc}}{\tau_{cs}} \hat{\tau}_x(x)}$

$W_o$  against the skin thickness over span ratio  $t/L$  and the core relative density  $\rho_c/\rho_s$ . The projection of the lines where two modes intersect provides the boundaries for the corresponding failure mode map, as depicted in Fig. 5.1. By comparing this map with those given in Fig. 2.5, one can see that the failure modes of pure core crushing or shear are now replaced by a core indentation region. The upper part of the indentation ‘area’ (higher core densities) corresponds to core crushing under the vicinity of the localised loads, whereas the lower part (lower densities) is characterised mainly by core shear.

A comparison between the failure loads calculated with HOSBT and the experimental results presented in Chapter 2 is depicted in Fig. 5.2 for all four examined core densities. The theoretical predictions for core crushing are more accurate for the new failure prediction, especially for the lower core densities of 29 or 48 kg/m<sup>3</sup> (c.f. Fig. 2.10). Also this new approach predicts the observed differences in behaviour for longitudinal and transverse honeycomb ribbon direction. Although the high-order sandwich beam theory provides a robust and compact computational tool for all the modes, there are two drawbacks; firstly, when the skin fails, the model calculates the same failure load for the longitudinal and transverse direction of the honeycomb core and secondly the predictions for the mode of skin wrinkling are overpredicted, especially closer to the transition from skin wrinkling mode to indentation mode. The latter is due to fact that HOSBT allows for local bending of the top skin before failure and therefore the calculated in-plane normal stresses  $\sigma_{txx}$  in the midspan are lower than those calculated by simplified beam models. Indeed the distribution of in-plane normal stresses  $\sigma_{txx}$  along the beam is triangular when predicted by simple beam theory, while HOSBT gives a curve tangential to this triangular distribution close to midspan. This discrepancy causes the differences in prediction.



**Figure 5.1:** Improved failure map for Nomex honeycomb sandwich beams. Each contour represents sandwich beams of equal strength in N/m



**Figure 5.2:** Comparison with the experimental results from Chapter 2. Lines show the predictions of HOSBT failure analysis and the symbols represent the experimental data (c.f. Fig. 2.10). Solid lines and symbols correspond to the longitudinal ribbon direction, while dashed lines and hollow symbols correspond to the transverse ribbon direction

### 5.3 Optimisation Carpet Plots

When designing a load-bearing structure the most important functional requirements are stiffness, strength and weight. In general these are attributes that we want to maximise or minimise. Minimum weight design is considered by Triantafillou and Gibson [33] for foam core sandwich beams and extended in Gibson's book [25]. In both cases, indentation is not examined as a possible core failure mode; only core shear failure is considered. They conclude that, in minimum weight design of a foam core sandwich beam of a given strength, the top skin and core must fail simultaneously. In this work we use the failure maps to optimise the design of honeycomb sandwich beams with a graphical methodology. Here it is assumed that the failure in the core is by indentation and is a result of the simultaneous effect of core shear and out-of-plane compression (Fig. 4.1).

Fig. 2.6 shows a useful practical form of a failure map. In this section we consider a typical case study, seeking an optimum design for a sandwich beam which is loaded under 3-point bending and for which the material properties and skin thickness are given. The ratio  $c/L$  and the relative core density  $\rho_c/\rho_s$  are variables to be optimised. Hence it is most useful to present failure maps in terms of  $c/L$  and  $\rho_c/\rho_s$ . Fig. 5.3 presents the data for Fig. 5.1 in this form, showing contours of equal failure line load. By adding to this map contours of equal stiffness and mass, carpet plots are produced which can be used to find the optimum design configuration. Such a carpet plot is shown in Fig. 5.5, where for clarity the mass contours and only one strength and one stiffness contour are shown. The full set of stiffness contours are plotted in Fig. 5.4.

Two optimisation cases are considered; strength limited design or stiffness limited design. These constraints are represented as hatched contours in Fig. 5.5. In addition a geometric constraint is included. In this case we suppose that the ratio of core thickness to span cannot exceed  $5 \times 10^{-2}$ . Where a minimum strength constraint is applied the potential choices are restricted to the upper right area of the map. By considering the mass contours, it is clear that the design which minimises the mass lies at point A on the intersection of the skin wrinkling - core indentation region on the strength contour. However, if other considerations impose a value of  $c/L$  less than  $2.4 \times 10^{-2}$  (the value of  $c/L$  which corresponds to point A) this conclusion would no longer hold. It may also be desirable to choose a panel which fails by indentation because this is a safer failure mode than the alternatives. For the material combination considered, the optimum design point lies on the border between core indentation and skin failure for a range of strength constraints. This accords with the relevant conclusion of ref. [33]

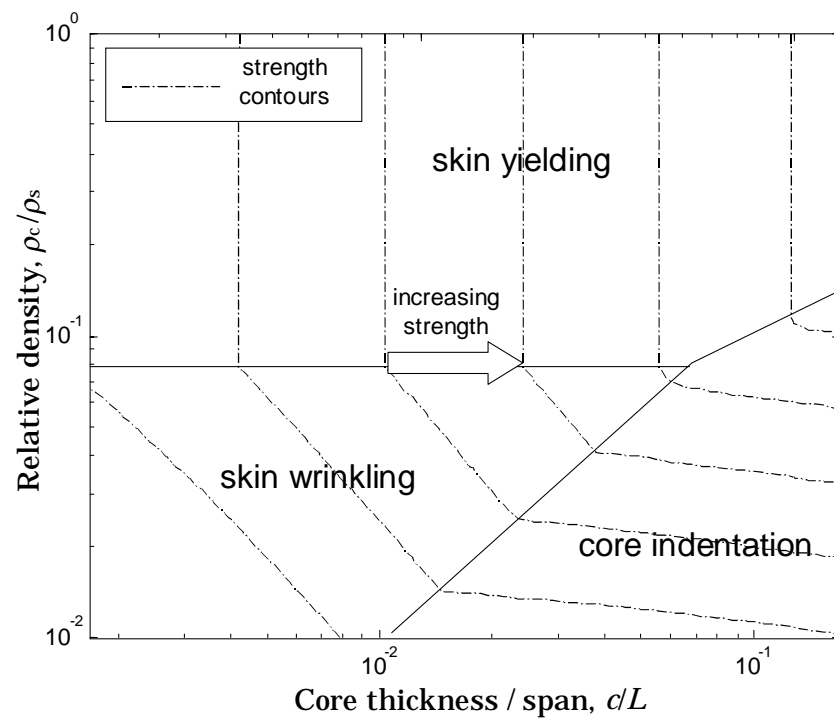


Figure 5.3: Strength contour plot corresponding to Fig. 5.1

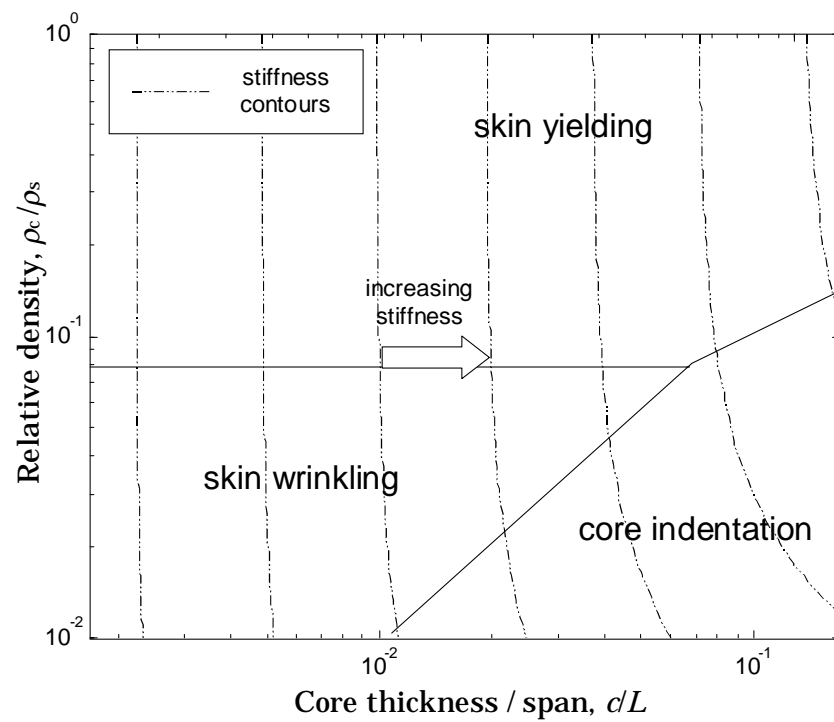
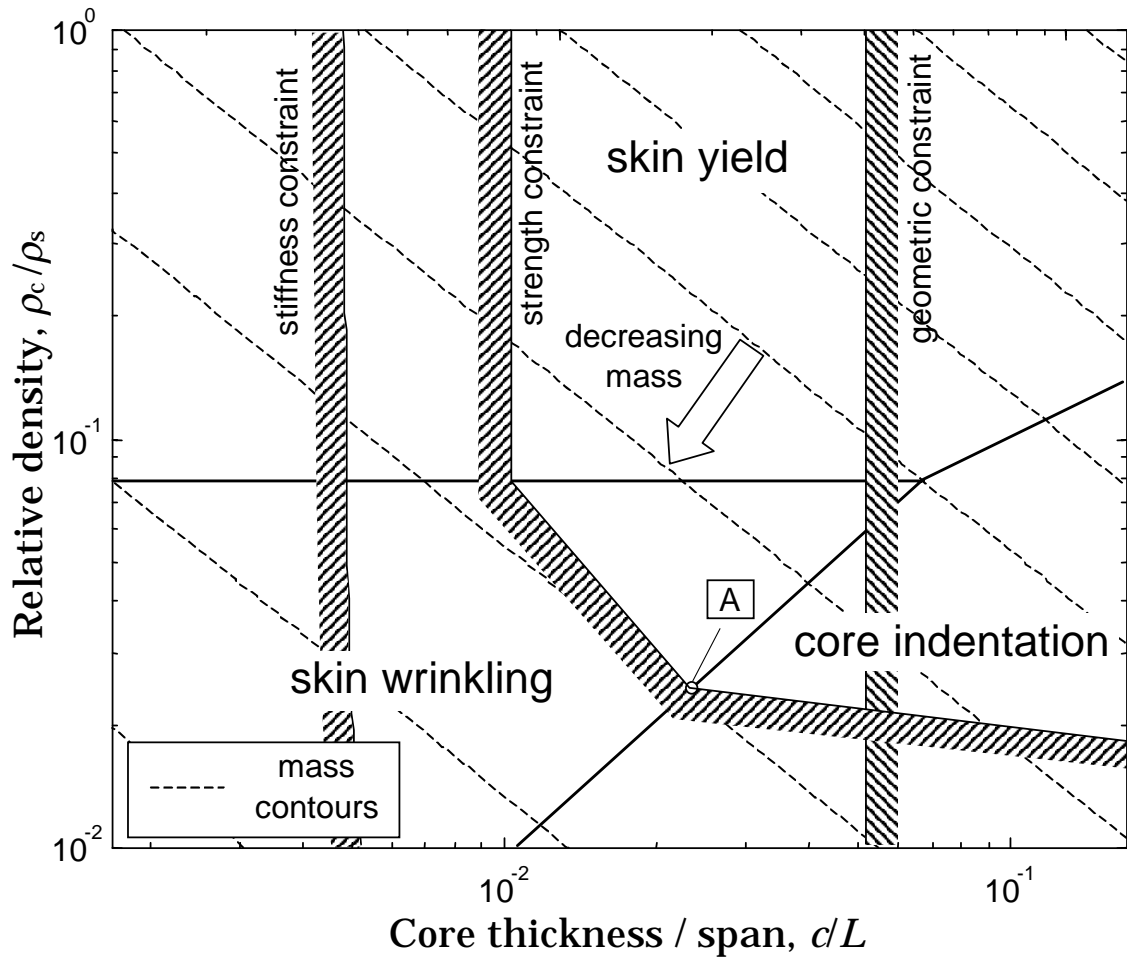


Figure 5.4: Stiffness contour plot

and [25] that the minimum design is such that the skin and core fail at the same peak load.

The above illustration assumes that stiffness criteria are always satisfied. Consider instead a stiffness limited design with a stiffness constraint shown by the hatched contour in Fig. 5.5. Now, the contours of mass suggest that the beam with minimum mass would be that with the minimum available relative density of the core. In practice some other constraint, for example a geometric constraint, a strength constraint, or a manufacturing constraint, will limit the extent to which the core density can be reduced. Indeed this ‘stiffness-limited’ case study illustrates the need to model strength of these panels, as this will be necessary to determine the optimum design.



**Figure 5.5:** Optimisation carpet plot for  $t/L = 5 \times 10^{-4}$  with  $\rho_c/\rho_s$  and  $c/L$  as design parameters

## **5.4 Concluding Remarks**

The high-order sandwich beam theory can be used, not only to predict indentation failure loads, but also the failure modes of skin failure, enabling the construction of failure mode maps. This approach offers the advantage of using only one computational tool to calculate the failure loads for every failure mode. The predictions follow satisfactorily the experimental data. However, the disadvantages of using the HOSBT for failure maps are overprediction of the failure loads for skin wrinkling and inability to predict the different behaviour between the two honeycomb ribbon directions when the top skin fails, either by yield or wrinkling.

Finally it is shown that failure maps can help with the preliminary design of sandwich beams under bending, by superimposing contours of mass, stiffness and strength.



# Chapter 6

## Conclusions and Future Work

This thesis addresses theoretical and experimental aspects of the design of honeycomb sandwich panels. The research focuses on sandwich beams made of cross-ply GFRP laminate skins with a Nomex/phenolic resin honeycomb core, a widely used combination for aircraft flooring panels and freight loading pallets. Indentation resistance of such sandwich panels with transversely flexible cores is an important factor in their design. An accurate model of the elastic deformation of such sandwich beams under three point bending has been derived. In particular, this model includes the local behaviour under the central load, allowing indentation failure to be examined.

### 6.1 Conclusions

Firstly the behaviour of sandwich beams of differing lengths and core densities is considered, to examine the importance of the possible failure modes, including failure by skin yielding, skin wrinkling, intra-cell buckling, core shear and indentation. At this initial treatment indentation is treated in an empirical way, using measurements of the bearing area at the load points. Previous research on honeycomb mechanics and simple beam models has been combined to derive failure mode maps for 3-point bending with axes as the core relative density and the ratio of the skin thickness to span length. These maps are based on those of Triantafillou and Gibson [41], who focused on sandwich beams with ductile aluminium skin and isotropic foam cores. This thesis appears to be the first attempt to construct maps for sandwich beams with laminate skins and honeycomb core. Since commercial panels are generally provided with standard skin thicknesses, but with differing core thickness and density, alternative maps with these two core variables are presented, since these will be more useful for a beam designer or manufacturer. Although the maps are generated for three-point bending, the method can straightforwardly be applied to other loading geometries, for example four-point

bending.

Experimental results for failure under three point bending are summarised as follows. A transition from face yielding to intra-cell buckling for long span beams was observed for a honeycomb cell size above a critical value. The measured peak loads were dependent on the direction of the honeycomb ribbon. This difference is due to the shear anisotropy of the honeycomb, illustrating the important role that core shear plays in the bending behaviour of these sandwich beams. Experimental results verified satisfactorily the predicted failure loads. The boundary between skin and core failure on the failure mode maps was also predicted with good accuracy. However, failure near the load points due either to core shear or core indentation was not modelled well.

A high-order sandwich beam theory (HOSBT) was implemented to provide a better deformation model of localised effects under concentrated loads and so to produce an improved indentation failure analysis for honeycomb sandwich beams. The benefits of using the high-order sandwich beam theory to analyse the behaviour of sandwich beams under indentation are presented and verified experimentally by measurements of the core deformation close to an indenter. HOSBT is used to extract a characteristic *spreading length*  $\lambda$ . This is a property of a sandwich beam, depending mainly on the skin's flexural stiffness and characterising the susceptibility of the sandwich beam to indentation loads. Small values of  $\lambda$  correspond to sandwich beam with very flexible skins which are transparent to the external loads. Large values of  $\lambda$  indicate rigid skins that restrict the transmission of localised loads to the core. HOSBT is further used to give an insight into the contact mechanics for a beam loaded by a cylindrical indenter. The way in which the contact pressure is transmitted through the core is examined. A case study shows the fact that sandwich beams used as standard in industry have skins which are rigid enough to spread the external loads. This spreading effect allows to predict the indentation behaviour of a sandwich beam with rigid skins without having to model accurately the contact between the indenter and the top skin. The assumption of a uniform distribution over a roughly estimated width (which depends on the size of the indenter) and the use of the high-order sandwich beam theory can provide reliable predictions of the stress field in the core.

The most important conclusion from this analysis is that the maximum normal stresses in the top skin-core interface, which are mainly responsible for indentation failure, cannot be predicted in a straightforward way for sandwich beams with rigid skins, even if the contact width is known. For sandwich beams with very flexible skins, the approximation of dividing the total line load  $W$  by  $\delta$  can give us reliable estimation of the failure stresses in the skin-core interface. However for commercially applied

sandwich configurations the skin is rather rigid and the flexible skin approximation cannot be used.

A systematic approach has been developed to determine the failure load of sandwich honeycomb structures under indentation loading. Biaxial tests of Nomex honeycombs using an Arcan rig show that a linear dependence on pure compression and shear proves to be a good approximation for the failure envelope of these honeycombs. Using this failure envelope and the core stress field determined by HOSBT, a mixed failure criterion has been introduced to predict the indentation failure, caused by the simultaneous action of out-of-plane compressive and shear stresses exerted in the vicinity of a localised load. This criterion can predict failure that ranges from pure core crushing to pure core shear.

Short beam bending tests validated the theoretical predictions of high order beam model and showed that the mixed failure criterion offers a significant improvement in predicting indentation strength, as compared with models which do not include combined loading. This new approach is particularly needed in high core densities which induce more severe stress fields in the core. It also predicts observed differences in behaviour for longitudinal and transverse ribbon directions. Video captures of the deformed side cross section of the tested sandwich beams illustrate the involvement of core shear in the elastic behaviour of sandwich beams with low density cores. Also they showed the different post-failure damage extent between sandwich beams with different core densities; the higher the core density the less damage propagates into the core and skins can suffer eventually macrobuckling failure.

The high-order sandwich beam theory can also be used to predict the failure modes of skin failure, enabling the construction of failure mode maps. This approach offers the advantage of using only one computational tool to calculate the failure loads for every failure mode. The predictions follow satisfactorily the experimental data. However, the disadvantages of using the HOSBT for failure maps are overprediction of the failure loads for skin wrinkling and inability to predict the different behaviour between the two honeycomb ribbon directions when the top skin fails, either by yield or wrinkling. Finally it is shown that failure maps can help with the preliminary design of sandwich beams under bending, by superimposing contours of mass, stiffness and strength.

## **6.2 Future Work**

With this study a framework of failure analysis of Nomex honeycomb panels has been established and provides the basis for further investigation in the following areas.

Bending tests should be done with sandwich beams with different skin thicknesses and core densities than those tested in this research work, in order to validate further the applicability of the proposed methodologies for failure analysis and for failure map construction. The failure envelope for biaxial loading of Nomex honeycombs determined in section 4.2 should also be investigated for other core materials.

In section 3.4 a parametric study is conducted to define the dependence of the spreading length  $\lambda$  on the material and geometric properties of a sandwich beam. The influence of each parameter has been determined qualitatively. Further work on this area could attempt to derive a single normalised curve  $C_m^{\sigma_{zz}}$  with respect to  $L/m$  (instead of all the curves in Fig. 3.7) that accurately captures the indentation resistance behaviour of a wide range of sandwich beam designs. This approach would lead to simple formulae relating  $\lambda$  to the material and geometric properties of a sandwich beam. Miller [79] adopts such an approach to model the indentation behaviour of foamed metals.

A finite element analysis of a model (see Fig 6.1) of a rigid indenter applying loads to a simply supported beam would be useful to determine the contact pressure between the indenter and the top skin, and the corresponding normal stresses transmitted to the core. These stresses can be compared with those calculated by the high-order beam theory model in section 3.5.

In Chapter 3 we showed the ability of the spreading length parameter  $\lambda$  to characterise the static indentation resistance of sandwich beams. It should be possible to compare  $\lambda$  values with experimental results on dynamic indentation resistance and investigate the applicability of  $\lambda$  as a quality factor in sandwich panel manufacturing. For this purpose, the software code used in section 3.4 to calculate  $\lambda$  could be provided to industry for assessment of its practical usefulness.

Finally the methodology for failure analysis proposed in this study should be used to explore the benefits of unsymmetrical sandwich beams with bottom skins thinner than the top ones. This option would exploit firstly the fact that composite laminates have approximately tensile strength twice as much their compressive and secondly the higher indentation resistance that a thicker top skin can provide.

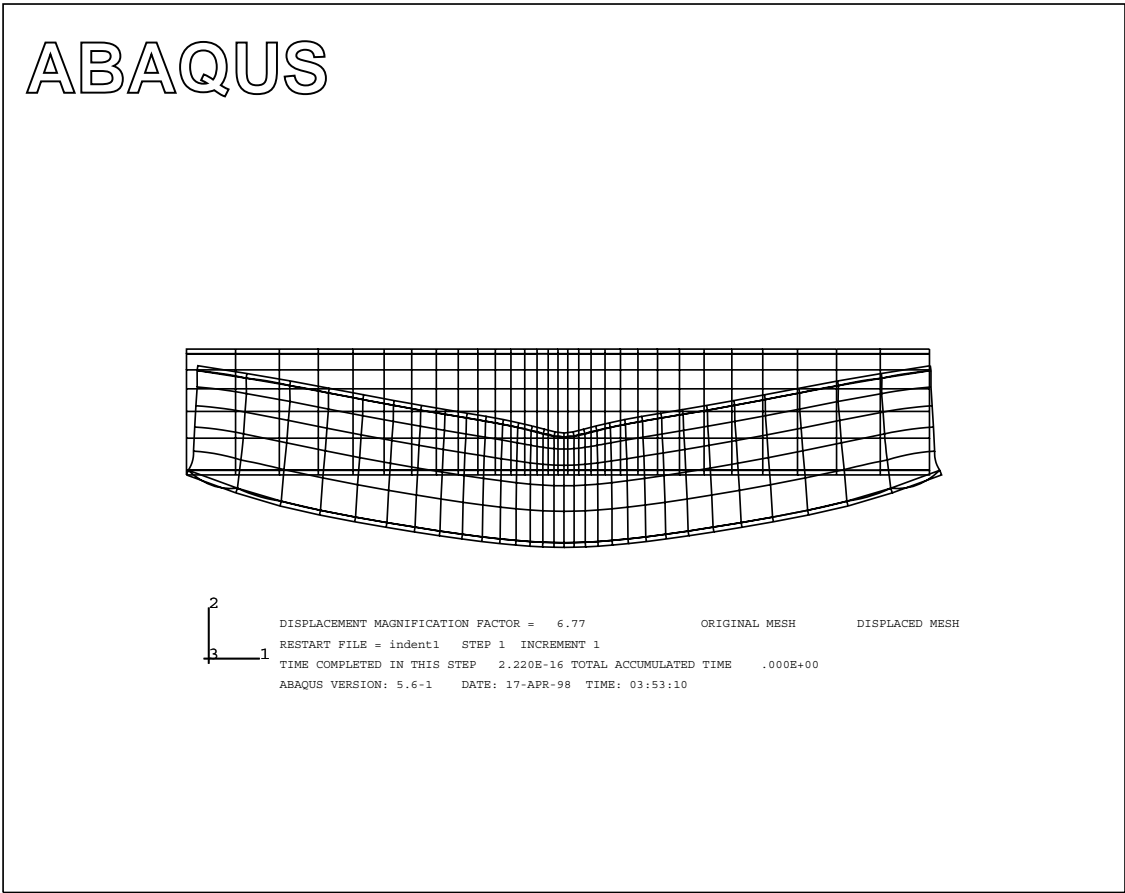


Figure 6.1: Vertical displacements calculated by Abaqus finite element analysis

# Appendix A

## Experimental Results

**Figure A.1:** For 6 mm diameter roller: midspan bottom skin deflection, midspan core compression, and line load variation curves with respect to midspan top skin deflection. Lines legend: (—) longitudinal and (– –) transverse honeycomb ribbon direction

**Figure A.2:** For 10 mm diameter roller: midspan bottom skin deflection, midspan core compression, and line load variation curves with respect to midspan top skin deflection. Lines legend: (—) longitudinal and (– –) transverse honeycomb ribbon direction



**Figure A.3:** For 20 mm diameter roller: midspan bottom skin deflection, midspan core compression, and line load variation curves with respect to midspan top skin deflection. Lines legend: (—) longitudinal and (– –) transverse honeycomb ribbon direction

**Figure A.4:** Video snapshots during loading with a 6 mm diameter roller

**Figure A.5:** Video snapshots during loading with a 10 mm diameter roller

**Figure A.6:** Video snapshots during loading with a 20 mm diameter roller

# Bibliography

- [1] J. E. GORDON, *Structures: or, why things don't fall down*, A Pelican Original, Penguin, Harmondsworth, 1978.
- [2] M. F. ASHBY, *Materials Selection in Mechanical Design*, Pergamon Press, Oxford, 1983.
- [3] R. W. BIRMINGHAM and J. A. D. WILCOX, Charting the Links Between Material Selection and Elemental Form in Structural Design, *Journal of Engineering Design*, **4**(2), 1993, pp. 127–140.
- [4] S. W. TSAI, *Theory of Composite Design*, Think Composites, 1992.
- [5] R. T. HAFTKA, Z. GÜRDAL and M. P. KAMAT, *Elements of Structural Optimization*, Kluwer Academic Publishers, Boston, USA, 1990.
- [6] D. HULL, *An Introduction to Composite Materials*, Cambridge University Press, 1981.
- [7] X. J. XIN, M. P. F. SUTCLIFFE, N. A. FLECK and P. T. CURTIS, *Cambridge Composite Designer - User's Manual*, Cambridge, 1995.
- [8] M. G. BADER, Materials Selection, Preliminary Design and Sizing for Composite Laminates, *Composites Part A*, **27A**(1), 1996, pp. 65–70.
- [9] M. MIKI, A Graphical Method for Designing Fibrous Laminated Composites with Required In-plane Stiffness, *Trans. JSCM*, **9**(2), 1983, pp. 51–55.
- [10] S. W. TSAI and J. M. PATTERSON, *Design Rules and Techniques for Composite Materials*, Longman, 1990.
- [11] J. A. QUINN, *Composites - Design Manual*, James Quinn Associates Ltd, Liverpool, 1995.
- [12] J. A. QUINN, Composites Selection Methods for Engineers, in *FRC 84*, Liverpool.
- [13] J. A. QUINN, Cost and Weight Optimisation Decisions for GRP, in *ICCM III*, Paris, 1980.

- [14] R. MARTIN, Composite Structures - A Dual Approach to Design, *Materials World*, **3**(7), 1995, pp. 320–322.
- [15] D. J. FARRAR, The Design of Compression Structures for Minimum Weight, *Journal of Royal Aeronautical Society*, 1949, pp. 1041–1052.
- [16] A. ZAHORSKI, Effect of Material Distribution on Strength of Panels, *Journal of Aeronautical Sciences*, 1944, pp. 247–253.
- [17] M. S. ANDERSON and W. J. STROUD, A General Panel Sizing Computer Code and its Applications to Composite Structural Panels, *AIAA Journal*, **17**(8), 1979, pp. 892–897.
- [18] D. C. JEGLEY, Study of Structurally Efficient Graphite - Thermoplastic Trapezoidal - Corrugation Sandwich and Semisandwich Panels, *Journal of Aircraft*, **31**(2), 1994, pp. 411–418.
- [19] D. L. GRAESSAR, Z. B. ZABINSKY, M. E. TUTTLE and G. I. KIM, Optimal Design of a Composite Structure, *Composite Structures*, **24**, 1993, pp. 273–281.
- [20] M. B. SNELL and P. BARTHOLOMEW, The Application of Geometric Programming to the Structural Design of Aircraft Wings, *Aeronautical Journal*, **86**(857), 1982, pp. 259–268.
- [21] M. B. SNELL and P. BARTHOLOMEW, Initial Design of Stringer Stiffened Bend Boxes Using Geometric Programming, *Aeronautical Journal*, **87**(861), 1983, pp. 21–25.
- [22] M. B. SNELL and P. BARTHOLOMEW, The Engineering Optimisation of Hybrid Composite/Metallic Wing Boxes for Buckling and Strength Constraints, *Composite Structures*, **7**(1), 1987, pp. 21–58.
- [23] R. J. DUFFIN, E. L. PETERSON and C. M. ZENER, *Geometric Programming*, John Wiley, 1967.
- [24] K. F. KARLSSON and B. T. ASTRÖM, Manufacturing and Applications of Structural Sandwich Components, *Composites Part A*, **28A**, 1997, pp. 97–111.
- [25] L. J. GIBSON and M. F. ASHBY, *Cellular Solids: Structure and Properties*, Pergamon Press, Oxford, 1988.
- [26] J. ZHANG, *The Mechanics of Foams and Honeycombs*, Ph.D. thesis, Cambridge University Engineering Department, Cambridge, U.K., 1989.
- [27] J. ZHANG and M. F. ASHBY, The Out-of-plane Properties of Honeycombs, *International Journal of Mechanical Science*, **34**(5), 1992, pp. 475–489.

- [28] J. ZHANG and M. F. ASHBY, Buckling of Honeycombs under In-plane Biaxial Stresses, *International Journal of Mechanical Science*, **34**(6), 1992, pp. 491–509.
- [29] G. SHI and P. TONG, Equivalent Transverse Shear Stiffness of Honeycomb Cores, *Int. Journal of Solids Structures*, **32**(10), 1995, pp. 1383–1393.
- [30] M. GREDIAC, A Finite Element Study of the Transverse Shear in Honeycomb Cores, *Int. Journal of Solids Structures*, **30**(13), 1993, pp. 1777–1788.
- [31] H. G. ALLEN, *Analysis and Design of Structural Sandwich Panels*, Pergamon Press, London, 1969.
- [32] F. J. PLANTEMA, *Sandwich Construction*, John Wiley & Sons, New York, 1966.
- [33] T. C. TRIANTAFILLOU and L. J. GIBSON, Minimum Weight Design of Foam Core Sandwich Panels for a Given Strength, *Materials Science and Engineering*, **95**, 1987, pp. 55–62.
- [34] Y. W. KWON, M. C. MURPHY and V. CASTELLI, Buckling of Unbalanced Sandwich Panels with Titanium and GRP Skins, *Journal of Pressure Vessel Technology*, **117**, 1995, pp. 40–44.
- [35] T. R. A. PEARCE, *The Stability of Simply-supported Sandwich Panels with Fiber Reinforced Face Plates*, Ph.D. thesis, University of Bristol, Bristol, U.K., 1973.
- [36] D. ZANKERT, *An Introduction to Sandwich Construction*, Engineering Materials Advisory Services, 1997.
- [37] P. J. HOLT and J. P. H. WEBBER, Exact Solutions to Some Honeycomb Beam, Plate, and Shell Problems, *Journal of Strain Analysis*, **17**(1), 1982, pp. 1–8.
- [38] A. K. MUKHOPADHYAY and R. L. SIERAKOWSKI, On Sandwich Beams with Laminated Facings and Honeycomb Cores Subjected to Hygrothermal Loads: Part I – Analysis, *Journal of Composite Materials*, **24**(4), 1990, pp. 382–400.
- [39] E. W. KUENZI, *Sandwich Sandwich Design Criteria*, Tech. 2161, Forest Products Laboratory, Madison, WI, Oct. 1959.
- [40] Y. SHENHAR, Y. FROSTIG and E. ALTUS, Stresses and Failure Patterns in the Bending of Sandwich Beams with Transversely Flexible Cores and Laminated Composite Skins, *Composite Structures*, **35**, 1996, pp. 143–152.
- [41] T. C. TRIANTAFILLOU and L. J. GIBSON, Failure Mode Maps for Foam Core Sandwich Beams, *Materials Science and Engineering*, **95**, 1987, pp. 37–53.
- [42] A. P. S. SELVADURAI, Elastic Analysis of Soil - foundation Interaction, *Developments in Geotechnical Engineering*, **17**, 1979.

- [43] O. T. THOMSEN, Analysis of Local Bending Effects in Sandwich Plates with Orthotropic Face Layers Subjected to Localised Loading, *Composite Structures*, **25**, 1993, pp. 511–520.
- [44] O. T. THOMSEN, Theoretical and Experimental Investigation of Local Bending Effects in Sandwich Plates, *Composite Structures*, **30**, 1995, pp. 85–101.
- [45] Y. FROSTIG and M. BARUCH, Bending of Sandwich Panels with Transversely Flexible Core, *AIAA Journal*, **28**(3), 1990, pp. 523–531.
- [46] Y. FROSTIG and M. BARUCH, Localized Load Effects in High-order Bending of Sandwich Panels with Flexible Core, *Journal of Engineering Mechanics*, **122**(11), 1996, pp. 1069–1076.
- [47] Y. FROSTIG, M. BARUCH, O. VILNAY and I. SHEINMAN, High-Order Theory for Sandwich-Beam Behaviour with Transversely Flexible Core, *Journal of Engineering Mechanics, ASCE*, **118**(5), 1992, pp. 1026–1043.
- [48] Y. FROSTIG, On Stress Concentration in the Bending of Sandwich Beams with Transversely Flexible Core, *Composite Structures*, **24**, 1993, pp. 161–169.
- [49] E. BOZHEVOLNAYA and Y. FROSTIG, Nonlinear Closed-Form High-Order Analysis of Curved Sandwich Panels, *Composite Structures*, **38**(1-4), 1997, pp. 383–394.
- [50] Y. FROSTIG, Hygothermal (environmental) Effects in High-Order Bending of Sandwich Beams with a Flexible Core and a Discontinuous Skin, *Composite Structures*, **37**, 1997, pp. 205–221.
- [51] Y. FROSTIG, Inaccuracies and Validity of Simplified Models in the Theory of Sandwich Structures, in *Proc. of the 4th Int. Conf. on Sandwich Construction*, vol. 1, Stockholm, 1998, (pp. 167–189).
- [52] K. B. ARMSTRONG, *Cost-Effective Design of Indentation Resistant Sandwich Panels for Aircraft Floors and Other Purposes*, Tech. EEA.S.4.8644, BOAC, Dec. 1969.
- [53] Ciba Composites, Duxford, England, *Honeycomb Sandwich Design Technology*, August 1995.
- [54] G. LUBIN, *Handbook of Composites*, Van Nostrand Reinhold Company, New York, 1982.
- [55] H. RAZI, B. SERGEEV, S. SHKARAYEV and E. MADENCI, Analysis of Sandwich Panels with Multiple-Site Damage, in *Proc. of the 4th Int. Conf. on Sandwich Construction*, vol. 1, Stockholm, 1998, (pp. 213–226).



- [56] P. A. LAGACE, J. E. WILLIAMSON, P. H. W. TSANG, E. WOLF and S. THOMAS, A Preliminary Proposition for a Test Method to Measure (Impact) Damage Resistance, *Journal of Reinforced Plastics and Composites*, **12**, 1993, pp. 584–601.
- [57] R. A. W. MINES, C. M. WORRALL and A. G. GIBSON, The Static and Impact Behaviour of Polymer Composite Sandwich Beams, *Composites*, **25**(2), 1994, pp. 95–110.
- [58] R. A. W. MINES and N. JONES, Approximate Elastic-Plastic Analysis of the Static and Impact Behaviour of Polymer Composite Sandwich Beams, *Composites*, **26**(12), 1995, pp. 803–814.
- [59] C. L. WU and C. T. SUN, Low Velocity Impact Damage in Composite Sandwich Beams, *Composite Structures*, **34**, 1996, pp. 21–27.
- [60] E. J. HERUP and A. N. PALAZOTTO, Low-Velocity Impact Damage Initiation in Graphite/Epoxy/Nomex Honeycomb-Sandwich Plates, *Composites Science and Technology*, **57**(12), 1997, pp. 1581–1598.
- [61] P. D. SODEN, Indentation of Composite Sandwich Beams, *Journal of Strain Analysis for Engineering Design*, **31**(5), 1996, pp. 353–360.
- [62] F. M. SHUAIEB and P. D. SODEN, Indentation Failure of Composite Sandwich Beams, *Composites Science and Technology*, **57**(9-10), 1997, pp. 1249–1259.
- [63] R. OLSSON and H. L. MCMANUS, Improved Theory for Contact Indentation of Sandwich Panels, *AIAA Journal*, **34**(6), 1996, pp. 1238–1244.
- [64] E. W. KUENZI, *Edgewise Compression Strength of Panels and Flatwise Flexural Strength of Strips of Sandwich Construction*, Tech. 1827, Forest Products Laboratory, Nov. 1951.
- [65] C. B. NORRIS and W. J. KOMMERS, *Short-column Compressive Strength of Sandwich Constructions as Affected by the Size of the Cells of Honeycomb-core Materials*, Tech. 1817, FPL, Aug. 1950.
- [66] T. WIERZBICKI, Crushing Analysis of Metal Honeycombs, *International Journal of Impact Engineering*, **1**(2), 1983, pp. 157.
- [67] K. LINGAIAH and B. G. SURYANARAYANA, Strength and Stiffness of Sandwich Beams in Bending, *Experimental Mechanics*, **31**(1), 1991, pp. 1–7.
- [68] THE MATHWORKS INC., *MATLAB, The Language of Technical Computing, Using Matlab*, 1996.
- [69] 20 Nov 1996, Personal communication from Hexcel Composites.

- [70] ANONYMOUS, Method of Flexure Tests of Flat Sandwich Structures, *ASTM*, **15.03**(C393-62), 1989.
- [71] O. T. THOMSEN and Y. FROSTIG, Localised Bending Effects in Sandwich Panels: Photoelastic Investigation versus High-Order Sandwich Theory Results, *Composite Structures*, **37**(1), 1997, pp. 97–108.
- [72] K. L. JOHNSON, *Contact Mechanics*, Cambridge University Press, Cambridge, 1985.
- [73] L. M. KEER and R. BALLARINI, Smooth Contact Between a Rigid Indenter and an Initially Stressed Orthotropic Beam, *AIAA Journal*, **21**(7), 1983, pp. 1035–1042.
- [74] L. J. GIBSON, M. F. ASHBY, J. ZHANG and T. C. TRIANTAFILLOU, Failure Surfaces for Cellular Materials under Multiaxial Loads — 2. Comparison of Models with Experiment, *International Journal of Mechanical Science*, **31**(9), 1989, pp. 665–678.
- [75] W. J. STRONGE and J. W. KLINTWORTH, *Biaxial Testing of Honeycomb in the Transverse Direction*, Tech. Report No. CUED/C-Mechanics/TR70, Cambridge University Engineering Department, March 1996.
- [76] M. ARCAN, Z. HASHIN and A. VOLOSHIN, A Method to Produce Uniform Plane-stress States with Applications to Fiber-reinforced Materials, *Experimental Mechanics*, **18**(4), 1978, pp. 141–146.
- [77] A. VOLOSHIN and M. ARCAN, Failure of Unidirectional Fiber-reinforced Materials — New Methodology and Results, *Experimental Mechanics*, **20**(3), 1984, pp. 280–284.
- [78] R. H. MARLOFF, Finite Element Analysis of Biaxial Stress Test Specimen for Adhesive Characterisation, in I. M. Daniel (editor), *ASTM STP*, vol. 787, 1988, (pp. 34–49).
- [79] R. E. MILLER, A Continuum Plasticity Model for the Constitutive and Indentation Behaviour of Foamed Metals, To be submitted to *Intl. J. Mech. Sci.*